MECHANISM INVESTIGATION AND STRUCTURE DESIGN OF ORGANIC PHOTOVOLTAIC CELLS FOR IMPROVED ENERGY CONVERSION EFFICIENCY

ZHANG CHUNFU

(B. Eng, M. Eng, Xidian University, China)

A THESIS SUBMITTED

FOR THE DEGREE OF DOCTOR OF PHILOSOPHY

DEPARTMENT OF

ELECTRICAL AND COMPUTER ENGINEERING

NATIONAL UNIVERSITY OF SINGAPORE

2009

Acknowledgements

First of all, I want to acknowledge the National University of Singapore for providing the research scholarship to me. It gave me the opportunity to work on this exciting and fascinating topic of organic solar cells.

I would like to express my gratitude to my advisor, Associate Professor Zhu Chunxiang, for giving me continuous inspiration, support and criticism throughout the whole of my work. A/Prof. Zhu always provided me with valuable insight and making sure that I was not lost in the research directions. Without his support, it would be impossible for me to finish this work.

I would like to thank Dr. Jiang Changyun and Dr. Tan Swee Tiam, my advisors in the Institute of Microelectronics. They supplied me the sufficient facilities to finish the main experimental parts in this work. It is my pleasure that I could work with them.

I would also like to greatly acknowledge the intellectual support of Prof. E. T. Kang during my graduate research. He has been closely associated with a significant part of my research and his knowledge and mastery in organic field have been truly inspirational. Thank him for valuable guidelines and supplying the experimental conditions. My special thanks also go to Dr. Tong Shi Wun for the many interesting and exciting discussions about organic solar cells. I am very grateful for her advice, help and collaborations.

I have had the pleasure of collaborating with numerous exceptionally talented graduate students and colleagues over the last few years. I would like to thank my colleagues in the organic electronics group, such as Song Yan, Eric Teo Yeow Hwee,

Ling Qidan, Lim Siew Lay, Liu Gang and Liu Yiliang for their discussions and supports. I would also like to thank Yang Jianjun and Yang Weifeng for their support and close friendship which I will always cherish. I would like to extend my appreciation to all other SNDL graduate students and technical staffs for their support and friendship.

Finally, I would like to express my gratitude towards my parents for their unconditional supports and understanding over the years. My deepest love and gratitude go to my wife, Wang Yinhua, and my daughter, Zhang Xinyi, for their love, patience, and enduring support.

Table of Contents

Summary

The performance of organic solar cells (OSCs) is severely limited by poor light absorption, exciton dissociation and charge transport. This challenge can be partially overcome through the use of the bulk heterojunction (HJ) solar cell structure because it has the potential to guarantee the effective exciton dissociation and carrier transport by forming the interpenetrating network. The purpose of this thesis is to investigate the mechanisms of bulk HJ solar cells and then design the novel solar cell structure to improve the power conversion efficiency.

In this thesis, the microscopic mechanisms of the short circuit current density (J_{SC}) and the open circuit voltage (V_{OC}) in bulk HJ solar cells are investigated. J_{SC} suffers from the serious optical interference effect, non-ideal exciton dissociation probability, low mobility and short carrier lifetime. All these factors are investigated and considered to predict J_{SC}. Another parameter, V_{OC} has a direct relationship with the offset energy between the donor (D) and the acceptor (A) materials both in layered and bulk HJ solar cells. However, in the two types of devices, V_{OC} shows different dependences on the electrodes. V_{OC} of layered HJ OSCs shows a very weak dependence on the electrodes, while V_{OC} of bulk HJ solar cells shows a strong dependence on the electrodes. It is suggested that their distinct structures lead to the different dependences of V_{OC} on the electrodes, although V_{OC} of the two types of solar cells follow the same mechanism and are mainly determined by the light injected carriers at the D/A interface and the electrodes.

Based on the above understandings, experimental studies are carried out to increase J_{SC} and enhance V_{OC} of the poly(3-hexylthiophene-2,5-diyl): [6,6]-phenyl-C_{61}-butyric acid methyl ester (P3HT:PCBM) solar cells. It is found that the sequence of the thermal annealing is critical for the performance of the polymer-fullerene bulk HJ solar cells. The post-annealed device shows a higher J_{SC}. This is attributed to the improved contact at polymer/aluminum interface, the improved phase-structured morphology due to the prohibition of the overgrowth of PCBM and the enhanced P3HT crystallinity. It is also found that a significant increase of V_{OC} is obtained in polymer-fullerene bulk HJ solar cells by using e-beam evaporated Al cathodes. This is because that the energetic particles of Al in the e-beam deposition damage the surface of P3HT and induce deep hole traps at the P3HT/Al interface while leave fullerene unaffected. These deep hole traps will induce the negative image charges in the cathode and form “dipoles”. The “dipoles” lower down the Al effective work function and induce a very strong increase of V_{OC}. Based on these findings, the post-annealed devices with the e-beam Al cathodes are optimized around the first and second optical interference peaks.

At last, a simple tandem structure design for efficient light harvesting is proposed. In this device structure, PCBM is employed simultaneously to form a bilayer HJ photovoltaic (PV) subcell with the underlying CuPc and a bulk HJ PV subcell with the blended P3HT. In comparison with the conventional tandem structure, the omission of the semitransparent intercellular connection layer reduces the complexity of the device and the light loss. This structure effectively improves J_{SC} and the overall power conversion efficiency (PCE).

List of Tables

List of Figures

List of Symbols and Abbreviations

α	absorption coefficient
ε_0	the permittivity of free space
ε_r	dielectric constant
λ	wavelength
μ	carrier mobility
σ_{rms}	root-mean-square roughness
τ	lifetime
ϕ	barrier height
a	initial distance of a given electron-hole pair
c	the vacuum speed of light
h	Planck constant
k_B	Boltzmann's constant
k_D	exciton dissociation rate
k_X	exciton decay rate to the ground state
m_e	the electron rest mass
m_{eff}	the effective mass
$\bar{n}$	complex index of refraction
q	electronic charge
r_B	Bohr radius
r_C	radius of coulombic potential well at k_BT
A	acceptor
AFM	tapping mode atomic force microscopy
CO_2	carbon dioxide
CuPc	copper phthalocyanine
D	donor
D_n, D_p	electron and hole diffusion coefficient
DOS	density of states
EA	electron affinity

E_B	exciton binding energy
E_F	Fermi level
E_{ge}	electronic energy gap
E_{go}	optical excitation energy gap
F	electric field
G	the average exciton generation rate
HJ	heterojunction
HOMO	the highest occupied molecular orbital
I_0	incident light intensity
I_s	reverse saturation current of the diode
I_{ph}	photocurrent
ITO	indium-tin-oxide
IP	ionization potential
ISC	inorganic solar cell
ILC	injection limited conduction
J_{SC}	the short circuit current density
L	the active layer thickness
L_D	exciton diffusion length
LUMO	the lowest unoccupied molecular orbital
MIM	metal insulator metal
MePc	metal phthalocyanine
M/O	metal/organic
N_A	LUMO density of states
N_D	HOMO density of states
P_{in}	the incident light power density
P	the dissociation probability
PCE, η	the power conversion efficiency
RCESs	renewable clean energy sources
PEDOT:PSS	poly[3,4-ethylene-dioxy-thiophene]:poly[4-styrenesulphonate]
R_n, R_p	recombination rates
OSC	organic solar cell

P3HT	poly(3-hexylthiophene-2,5-diyl)
PCBM	[6,6]-phenyl-C_{61}-butyric acid methyl ester
PV	photovoltaic
R_s	series resistance
R_{sh}	shunt resistance
SCLC	space charge limited current
T	temperature
TMF	transfer-matrix theory
U	electric potential
V_{bi}	built-in potential
V_{OC}	the open circuit voltage
XPS	X-ray photoelectron spectroscopy
XRD	X-ray diffraction

Chapter 1
Introduction

1.1 Need for renewable clean energy

There is continuous increase of the global energy demand every year [1.1]. However, till now the vast portion of global energy production comes from fossil fuels (coal, oil and natural gas as shown in Fig. 1.1). It is widely known that the combustion of fossil fuels has detrimental long term effects on the natural balance by increasing the concentration of carbon dioxide (CO_2) in the atmosphere, which contributes to the greenhouse effect [1.2]. Today's plants are unable to absorb this huge amount of extra CO_2. As a result, the CO_2 in the atmosphere continues to mount and induce the global warming [1.4]. Another more important problem is that fossil fuels will expire in roughly 50 years [1.5]. Hydroelectricity is a type of renewable energy. However, the construction of hydropower stations may destroy the ecological balance and cause the ecological disaster. Nuclear power is another promise candidate. But, it produces highly dangerous and long lasting radioactive waste that requires expensive containment. Thus, renewable clean energy sources (RCESs) have been considered as the best alternatives as they do not produce waste and are readily available. RCESs include things such as wind power, geothermal sources and solar power. Among them, the most abundant, but not yet well utilized is the solar energy (Fig. 1.1 and Fig. 1.2). The total amount of solar irradiation per year on the earth's surface is about 89 PW [1.6]. Only capturing less than 0.02% would be enough to meet the current energy needs. It has been widely recognized that harvesting energy directly from the sunlight by using photovoltaic (PV) technology is an

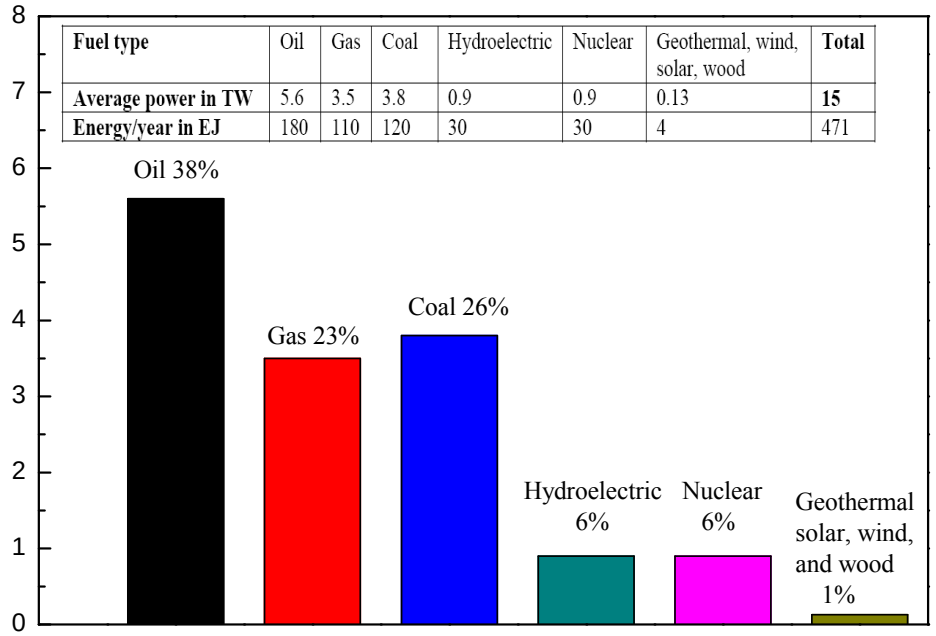

Fig. 1.1 According to the US Energy Information Administration's 2006 estimation, the estimated 471 EJ total consumption in 2004 was divided as in the inset, with fossil fuels supplying 86% of the world's energy [1.3].

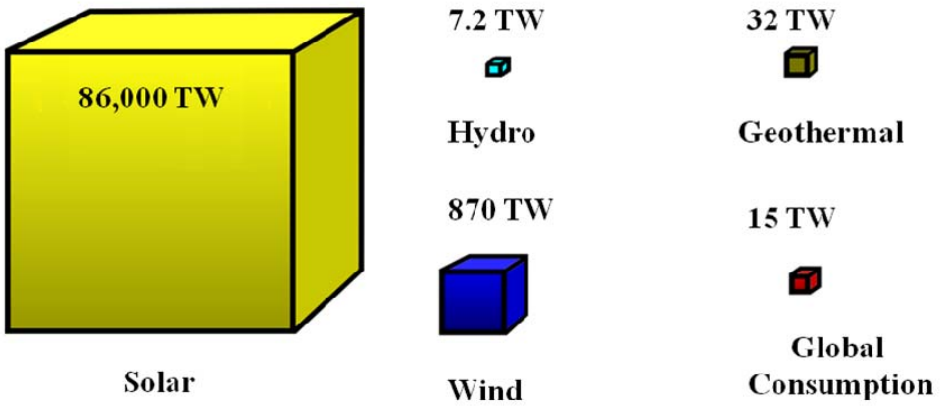

Fig. 1.2 Available renewable energy. The volumes of the cubes represent the amount of available geothermal, hydropower, wind and solar energy in TW, although only a small portion is recoverable. The small red cube shows the proportional global energy consumption [1.3].

essential component to utilize the solar energy. Such a way of using the sunlight as a primary energy source is enormous. It has been calculated that covering only 0.1% of the earth's surface area with solar cells of 10% efficiency will be enough for the global electricity consumption [1.7]. The vast application potential of solar cells attracts a great deal of research interests in the past few decades.

1.2 Solar cells

Solar cells have obvious advantages as they are silent and panels can be placed upon walls or rooftops so they do not interfere with views or surroundings. Additionally, the sun itself is the primary source of energy for the whole planet. Solar cells provide us with a great opportunity to harness this energy source for everyday use.

1.2.1 Inorganic solar cells (ISCs)

The modern age of solar power technology arrived in 1954 when the first crystalline silicon solar cell was developed at Bell Laboratory [1.8]. This resulted in the production of the first practical solar cells with the power conversion efficiency (PCE) of around 6%. Since then, PCE of silicon solar cells has increased steadily and reached 25% in the laboratory [1.9], which is approaching the theoretical PCE limiting of 33% [1.10]. Besides the Si solar cells, other types of solar cells have also been made from many other semiconductor materials with various device configurations, such as monocrystalline, polycrystalline, and amorphous thin-film structures as shown in Fig. 1.3. However, Si-based solar cells are by far the most dominant type of solar cells used and account for 99% of all PV devices [1.11, 1.12]. Conventional ISCs are almost based on the p-n junction, where the photovoltage is generated and the electric field is formed. Under the

light illumination, the holes and electrons produced in or near the p-n junction region are separated by the electric field and move towards the proper electrodes.

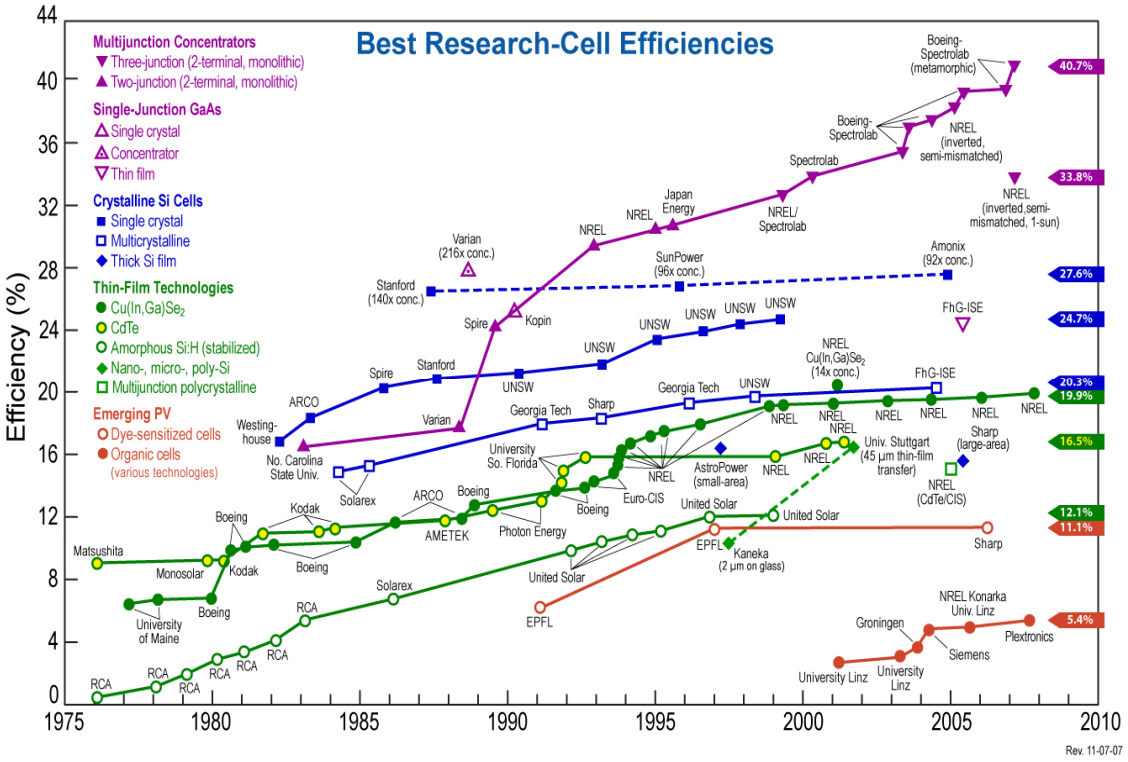

Fig. 1.3 Progress of research-scale PV device efficiencies, under AM 1.5 simulated solar illumination, for a variety of technologies [1.13].

With the increasing PCE and decreasing production cost, the solar cell production has grown by 20-25% each year since 1980. However, these semiconductor PV devices only account for less than 0.1% of the total world energy production [1.11]. One of the major obstacles is still the large production cost for Si based technology. For example, the production of high quality monocrystalline silicon uses extremely high temperature making it very costly [1.14]. A further disadvantage of silicon and other crystalline devices is that they are inflexible and generally very brittle, so they have to be kept flat or

well supported. Otherwise, they will break and be rendered useless. Even though all the obstacles are overcome, large scale production of Si-based solar cells is still limited by the availability of raw Si materials. To ensure a sustainable development of PV devices, it is clear that a cheaper, cleaner and more easily processable material is needed.

1.2.2 Organic solar cells (OSCs)

Organic materials fulfill all of the above requirements. Compared to inorganic semiconductors like Si, they are very cheap. In addition, organic materials usually have extremely high optical absorption coefficients which offer the possibility to fabricate the very thin solar cells. Thus the material consumption in the production is expected to be very low. Organic materials are generally soluble and then it is possible to fabricate the solar cells only by using fewer steps and cheaper technologies, such as various coating methods. Additional attractive feature of organic materials is the property of flexibility. And it is possible for the thin flexible devices to be fabricated using high-throughput, low temperature approaches which employ the well established printing techniques in a roll-to-roll process [1.15, 1.16]. Organic materials have further advantages. They can be designed in molecules at the atomic level by the method of synthetic chemistry according to the requirements [1.17, 1.18]. By this method, it is also possible to change the molecules to absorb more light and much more suited for the solar spectrum [1.19]. The obvious advantages of organic materials attract more and more research interest. PCE of OSCs has been steadily improved in recent years as shown in Fig. 1.4. Now it has been believed that OSCs bear the potential to develop a long term technology that is economically viable for large-scale power generation based on environmentally safe materials with unlimited availability.

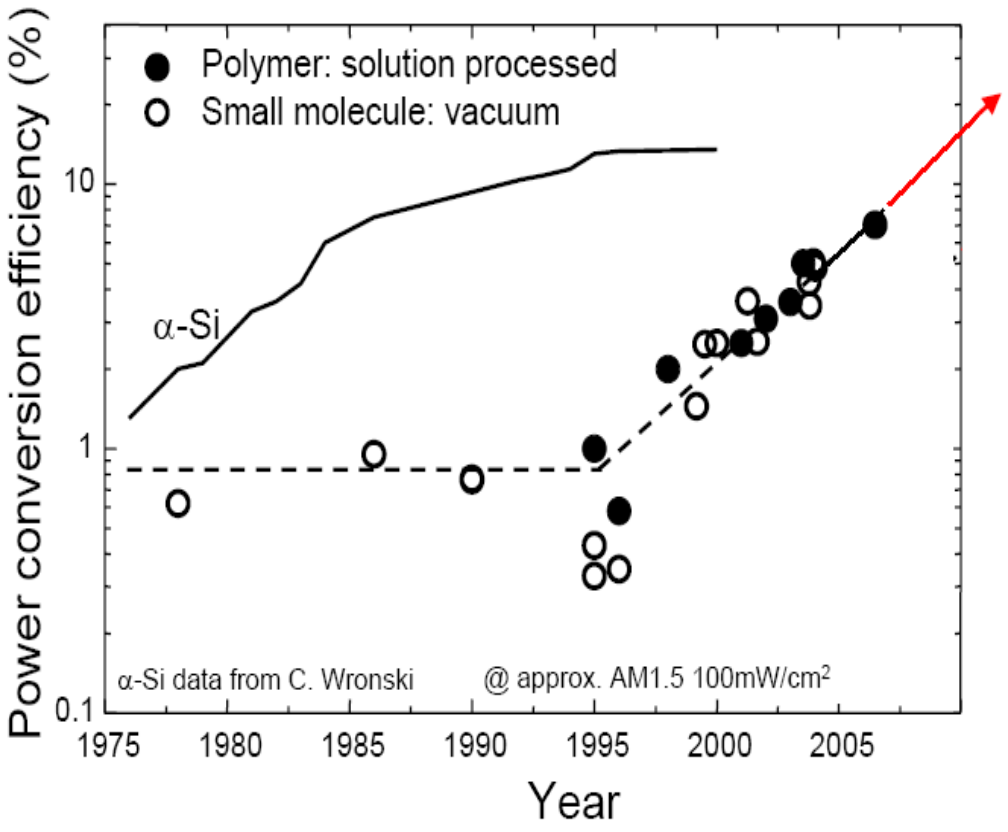

Fig. 1.4 Progress in PCE for both small-molecular weight and polymer PV cells over a span of 30 years. Also shown for comparison is the progress made in a more conventional thin-film technology, amorphous Si. Note that the initial slope of a-Si cell progress is similar to what we are experiencing today in organic thin films [1.20].

1.3 Development of OSCs

The first study of OSCs was reported when studying an anthracene single crystal in 1959 [1.21]. This device was based on a single organic material and exhibited a photovoltage of 200 mV with an extremely low PCE. After that for many years, OSCs were not used for any possible application because their typical PCE was generally very poor (in the range of 10^{-3} to 10^{-2}%) [1.22]. A major breakthrough came in 1985 when a

bilayer-structure OSC was firstly demonstrated by Tang, which exhibited the PCE around 1% based on two organic materials: perylene tetracarboxylic derivative and copper phthalocyanine (CuPc) [1.23]. The record was kept for many years and only broken at the turn of the millennium [1.24]. Now the layered OSCs have been the widely investigated devices. Another important discovery occurred in early 1990s when the ultra-fast photoinduced charge transfer at the interface between a conjugated polymer and the Buckminster fullerene C_{60} was found [1.25]. Following that, another revolutionary development in OSCs came with the introduction of the bulk heterojunction (HJ), where the donor (D) and acceptor (A) materials are blended together. This bulk HJ structure forms the interpenetrating network in the active region of OSCs. In the ideal condition, this structure can ensure the efficient dissociation of the produced excitons and at the same time guarantee the carrier transport. In the past decade, both layered and bulk HJ PV cells have been investigated by using either molecules, conjugated polymers, combinations of small molecules and conjugated polymers or combinations of inorganic and organic materials as the active layer. The performance of OSCs has been steadily improved [1.26]. A recent development of OSCs is summarized in Table 1.1.

Because small molecules show limited solubility in the solvents, traditionally they are mainly deposited by vacuum deposition techniques. In contrast, conjugated polymers are easy to be dissolved in common solvents. The polymer solution can be cast to form a thin organic film by using very simple deposition method, such as spin coating, screen printing or ink jet printing. Thus the conjugated polymers do not require high vacuum sublimation equipment. Now both the sublimed and solution processed OSCs are being developed very fast and the best performance of them shows the comparable efficiency as

shown in Table 1.1. Both of them are now under the intense investigation. The head-to-head race is going between them and which type of PV cell will win the race is still unknown yet.

Table 1.1 Summary of various organic PV cell results

Materials		J_{SC}(mA/cm^2)	V_{OC}(V)	η(%)	P_{in} (mW/cm^2)	Ref.
Donor	Acceptor					
Single layer based solar cells						
Merocyanine		0.18	1.2	0.62	78	1.27
ZnPc		5.6×10^{-4}	0.59	3×10^{-4}	0.1	1.28
Small molecules based solar cells						
CuPc	C_{60}	9.7	1.0	5.7	100	1.29
CuPc	C_{60}	15	0.54	5.0	100	1.30
MeO-TPD, ZnPc	C_{60}	10.8	1.0	3.8	130	1.31
DCV5T	C_{60}	8.25	0.98	3.4	118	1.32
SubPc	C_{60}	3.36	0.97	2.1	100	1.33
CuPc	PTCBI	11	0.49	2.7	100	1.34
Petacene	C_{60}	8.8	0.3	1.6	80	1.35
Polymer-fullerene solar cells						
P3HT	PCBM	9.5	0.63	5.0	80	1.36
P3HT	PCBM	11.1	0.6	4.9	80	1.37
PCPDTBT	$PC_{71}BM$	16.2	0.62	5.5	100	1.38
P3HT	PCBM	11.1	0.61	5.0	90	1.39
P3HT	PCBM	10.8	0.61	4.4	100	1.40

P3HT	PCBM	10.1	0.60	3.5	100	1.41
P3HT	$PC_{71}BM$	10.8	0.59	4.1	85	1.42
P3HT	PCBM	9.1	0.60	3.4	100	1.43
APFO-G5	PCBM	8.2	0.61	2.2	100	1.44
MEH-PPV	PCBM	7.0	0.85	1.5	130	1.45
MDMO-PPV	PCBM	8.2	0.76	3	100	1.46
PCPDTBT	$PC_{71}BM$	11	0.7	3.2	100	1.47
PEBT	PCBM	3.1	1.01	1.1	100	1.48
P3OT	PCBM	3.5	0.35	0.60	100	1.49
Inorganic nanoparticle-polymer solar cell						
OC_1C_{10}-PPV	CdSe	9.1	0.76	2.8	89	1.50
P3HT	CdSe	8.79	0.62	2.6	92	1.51
APFO-3	CdSe	7.23	0.95	2.4	100	1.52
P3HT	CdSe	6.07	0.70	1.7	100	1.53
MDMO-PPV	ZnO	2.4	0.81	1.6	100	1.54
MEH-PPV	ZnO	2.3	1.14	1.1	90	1.55
P3HT	TIO_2	2.76	0.44	0.42	100	1.56
P3HT	ZnO-dye	2.00	0.28	0.20	100	1.57
P3HT	$CuInSe_2$	0.30	1.00	0.15	80	1.58
P3HT	PbSe	1.08	0.35	0.14	100	1.59
P3OT	SWNT	0.5	0.75	0.22	100	1.60

Although great progress has been made in the development of OSCs, there are still many open questions regarding the working mechanisms, the device structure designs

and the fabrication processes. The short circuit current (J_{SC}) is still low in OSCs compared to their inorganic counterparts. This is directly related to the optical-electrical process in organic materials. As is known, excitons rather than free carriers are usually produced in organic materials. The production, motion and dissociation of the excitons have a great influence on J_{SC}. A good understanding of the exciton properties is essential to increase J_{SC}. Another important limiting parameter in OSCs is the open circuit voltage (V_{OC}). It is known that the metal-insulator-metal (MIM) model describes V_{OC} well for the single layer OSCs. However, the situation becomes different for OSCs based on the HJ structure. For this type of solar cells, V_{OC} is rather a complicated function of D and A interface conditions and morphology of the active layer. A good understanding of the determining factors is important to increase V_{OC}. Various fabrication processes, such as post-annealing process (anneal the device after metal deposition) and cathode deposition method, also affect the OSCs performance. Huge amount of experimental work is needed to optimize the fabrication process. For the further improvement of OSCs, other efforts, such as novel structure design, are also urgently needed. All these issues will be addressed in this work.

1.4 Outline of the study

In Chapter 2, the general theory related to organic semiconductors in PV devices is introduced. Compared to the inorganic materials, excitons rather than free carriers are produced in the organic materials. This property determines the working processes of OSCs: light absorption (exciton generation), exciton diffusion, exciton dissociation (charge generation) and charge transport. Every process has its own limiting factors. In

order to overcome these limiting factors, various structures are proposed. In this chapter, the fundamental background about organic PV cells will be briefed.

In Chapter 3, we will focus on the microscopic generation mechanism of J_{SC} in bulk HJ solar cells. Compared to the inorganic materials, the absorption coefficients of organic materials are usually very high, which makes the active layer very thin. Thus, the optical interference effect becomes very important in OSCs. At the same time, not all the excitons can be dissociated into free carriers and contribute to J_{SC}. The exciton dissociation probability has an important influence on J_{SC}. These factors are considered in this chapter, and the calculation of J_{SC} is introduced. Finally, the influence of carrier lifetime on J_{SC} will be discussed.

Another important parameter, V_{OC}, is discussed in Chapter 4. It has been shown that V_{OC} has a direct relationship with the energy difference between the highest occupied molecular orbital (HOMO) of D and the lowest unoccupied molecular orbital (LUMO) of A in both the layered and bulk HJ PV cells. However, how the electrodes affect V_{OC} is still not well understood. Experimental results show that V_{OC} of layered HJ organic PV cells shows a very weak dependence on the electrodes, while V_{OC} of bulk HJ PV cells shows a strong dependence on the electrodes. In this chapter, the mechanism behind this phenomenon is investigated.

Based on the above theoretical studies, the poly(3-hexylthiophene-2,5-diyl): [6,6]-phenyl-C_{61}-butyric acid methyl ester (P3HT:PCBM) solar cells are investigated in Chapter 5. It is found that the sequence of the thermal annealing is critical for the performance of the polymer-fullerene bulk HJ solar cells. The post-annealed device shows a higher J_{SC}. This is attributed to the improved contact at polymer/aluminum

interface, the improved phase-structured morphology due to the prohibition of the overgrowth of PCBM and the enhanced P3HT crystallinity. It is also found that a significant increase of V_{OC} is obtained in polymer-fullerene bulk HJ solar cells by using e-beam evaporated Al cathodes. This is because the energetic particles of Al in the e-beam deposition damage the surface of P3HT and induce deep hole traps at the P3HT/Al interface while leaving PCBM unaffected. These deep hole traps induce the negative image charges in the cathode and form "dipoles". The "dipoles" lower down the Al effective work function and induce a very strong increase of V_{OC}. Based on these findings, the post-annealed device with the e-beam Al cathode is optimized around the first and second optical interference peaks.

In Chapter 6, a simple tandem structure design of OSCs for efficient light harvesting is proposed and demonstrated. It is well known that PCE of OSCs is still low compared to their inorganic counterparts despite their recent fast development. One important factor is the limited overlap of the absorption spectra of organic materials with the solar spectrum. The design of tandem structures, in which two or more cells are stacked, is an effective way to overcome this problem. In this chapter, a simple tandem structure of OSCs is proposed and demonstrated for efficient light harvesting. In this device structure, PCBM is employed simultaneously to form a bilayer HJ PV subcell with the underlying CuPc and a bulk HJ PV subcell with the blended P3HT. In comparison with the conventional tandem structure, the omission of the semitransparent intercellular connection layer reduces the light loss and the complexity of the device fabrication.

At last, the important results of this work are summarized and some suggestions for future work are discussed in Chapter 7.

References

[1.1] A. H. Cordesman and K. R. Al-Rodhan, the International Energy Outlook 2005, http://www.csis.org/media/csis/pubs/050805_energyoutlook[1].pdf.

[1.2] United Nations Environment Programme (UNEP), Global environment outlook (GEO yearbook 2004/5), www.unep.org/geo/yearbook.

[1.3] World energy resources and consumption: http://en.wikipedia.org/wiki/World_ energy_ resources_and_consumption#cite_note-gcep-9.

[1.4] N. Oreskes, Science, 306, 1686 (2004).

[1.5] Commission of the European Communities, Green Paper, 769 (2000).

[1.6] J. W. Tester, E. M. Drake, M. J. Driscoll, M. W. Golay and W. A. Peters, Sustainable Energy: Choosing Among Options, The MIT Press (2005).

[1.7] Grätzel, M. Nature, 414, 338 (2001).

[1.8] D. M. Chapin, C. S. Fuller and G. L. Pearson, J. Appl. Phys., 25,676 (1954).

[1.9] UNSW: The University of New South Wales - Sydney Australia - News - Magic solar milestone reached.

[1.10] M. Green, Physica E, 14, 65 (2002).

[1.11] For a comprehensive review on Si and other types of solar cells see: A. Goetzberger, C. Hebling, H.W. Chock, Mater. Sci. Eng. R, 40, 1(2003).

[1.12] J. Carabe and J.J. Gandia, Opto-Electron. Rev., 12, 1 (2004).

[1.13] Solar cell: http://en.wikipedia.org/wiki/Solar_cell.

[1.14] J. J. Dittmer, R. Lazzaroni, Ph. Leclere, P. Moretti, M. Granstrom, K. Petritsch, E. A. Marseglia, R. H. Friend, J. L. Bredas, H. Rost, and A. B. Holmes, Sol. Energy Mater. Sol. Cells, 61, 53 (2000).

[1.15] S. E. Shaheen, R. Radspinner, N. Peyghambarian and G. E. Jabbour, Appl. Phys. Lett., 79, 2996 (2001).

[1.16] P. W. M. Blom, V. D. Mihailetchi, L. J. A. Koster, and D. E. Markov, Adv. Mater., 19, 1551 (2007).

[1.17] C. Winder, Sensitization of Low Bandgap Polymer Bulk Heterojunction Solar Cells, PhD thesis, Universitat Linz (2001).

[1.18] S. H. Chanteau and J. M. Tour, J. Org. Chem., 68, 8750 (2003).

[1.19] D. Muhlbacher, H. Neugebauer, A. Cravino, N. S. Sariciftci, J. K. J. van Duren, A. Dhanabalan, P. A. van Hal, R. A. J. Janssen, and J. C. Hummelen, Molecular Crystals and Liquid Crystals, 385, 205 (2002).

[1.20] S. R. Forrest, Mrs. Bulletin, 30, 28 (2005).

[1.21] H. Kallmann and M. Pope, J. Chem. Phys., 30, 585 (1959).

[1.22] H. Hoppea and N. S. Sariciftci, J. Mater. Res., 19, 1924 (2004).

[1.23] C. W. Tang, Appl. Phys. Lett., 48, 183 (1986).

[1.24] P. Peumanns, V. Bulovic, and S. R. Forrest, Appl. Phys. Lett., 76, 2650 (2000).

[1.25] N. S. Sariciftci, L. Smilowitz, A. J. Heeger, and F. Wudl, Science, 258, 1474 (1992).

[1.26] J. Y. Kim, K. Lee, N. E. Coates, D. Moses, T. Q. Nguyen, M. Dante, and A. J. Heeger, Science, 317, 222 (2007).

[1.27] D. L. Morel, A. K. Ghosh, T. Feng, E. L. Stogryn, P. E. Purwin, R. F. Shaw, and C. Fishman, Appl. Phys. Lett., 32, 495 (1978).

[1.28] S. Siebentritt, S. Gunster, and D. Meissner, Synth. Met., 41, 1173 (1991).

[1.29] J. Xue, B.P. Rand, S. Uchida, and S. R. Forrest, Appl. Phys. Lett., 85, 5757 (2004).

[1.30] J. Xue, B. P. Rand, S. Uchida, and S. R. Forrest, Adv. Mater. (Weinheim,Ger.), 17, 66 (2005).

[1.31] J. Drechsel, B. Mannig, F. Kozlowski, M. Pfeiffer, K. Leo and H. Hoppe, Appl. Phys. Lett., 86, 244102 (2005).

[1.32] K. Schulze, C. Uhrich, R. Schuppel, K. Leo, M.Pfeiffer, E. Brier, E. Reinold and P. Bauerle, Adv. Mater., 18, 2872 (2006).

[1.33] K. L. Mutulo, E. I. Mayo, B. P. Rand, S. R. Forrest and M. E. Thompson, J. Am. Chem. Soc., 128, 8108 (2006).

[1.34] F. Yang, M. Shtein, and S.R. Forrest, J. Appl. Phys., 98, 014906 (2005).

[1.35] A. K. Pandey, and J. M. Nunzi, Appl. Phys. Lett. 89, 213506 (2006).

[1.36] W. Ma, C. Yang, X. Gong, K. Lee and A. J. Heeger, Adv. Funct. Mater. 15, 1617 (2005).

[1.37] M. Reyes-Reyes, , K. Kim, and D. L. Carroll, Appl. Phys. Lett., 87, 083506 (2005).

[1.38] J. Peet, J. Y. Kim, N. E. Coates, W. Ma, D. Moses, A. J. Heeger and G. C. Bazan, Nat. Mater., 6, 497 (2005).

[1.39] K. Lee, J.Y. Kim and A. J. Heeger, Proc of SPIE, 6117, 61170T (2006).

[1.40] G. Li, V. Shrotriya, J. Huang and Y. Yao, T. Moriarty, K. Emery, Nat. Mater. 4, 864 (2005).

[1.41] A. J. Moule, J. B. Bonekamp and K. Meerholz, J. Appl. Phys., 100, 094503 (2006).

[1.42] S. Yoo, W. J. Potscavage, B. Domercq, J. Kim, J. Holt and B. Kippelen, Appl. Phys. Lett., 89, 233516 (2006).

[1.43] R. C. Hiorns, R. de Bettignies, J. Leroy, S. Bailly, M. Firon and C. Sentein, Adv. Funct. Mater., 16, 2263 (2006).

[1.44] F. Zhang, W. Mammo, L. M. Andersson, S. Admassie, M. R. Andersson and O. Inganas, Adv. Mater., 18, 2169 (2006).

[1.45] D. W. Sievers, V. Shrotriya and Y.Yang, J. Appl. Phys., 100, 114509 (2006).

[1.46] M. Al-Ibrahim, H. K. Roth, and S. Sensfuss, Appl. Phys. Lett., 85, 1481 (2004).

[1.47] D. Muhlbacher, M. C. Scharber, M. Morana, Z. Zhu, D. Waller and R. Gaudiana, J. Adv. Mater., 18, 2884 (2006).

[1.48] J. Cremer, P. Bauerle, M. M. Wienk and R. A. Janssen, Chem. Mater., 18, 5832 (2006).

[1.49] L. H. Nguyen, S. Gunes, H. Neugebauer, N. S. Sariciftci, F. Banishoeib and A. Henckens, Sol. Energy Mater. Sol. Cells, 90, 2815 (2006).

[1.50] B. Sun, H. J. Snaith, A. Dhoot, S. Westenhoff, N. C.Greenham, J. Appl. Phys., 97, 014914 (2005).

[1.51] B. Sun and N. C. Greenham, Phys. Chem. Chem. Phys., 8, 3557 (2006).

[1.52] P. Wang, A. Abrusci, H. M. P. Wong, M. Svensson, M. R. Andersson and N. C. Greenham, Nano. Lett., 6, 1789 (2006).

[1.53] W. U. Huynh, J. J. Dittmer and A. P. Alivisatos, Science, 295, 2425 (2002).

[1.54] W. J. E. Beek, M. M. Wienk and R. A. Janssen, Adv. Mater., 16, 1009 (2004).

[1.55] W. J. E. Beek, L. H. Slooff, M. M. Wienk, J. M. Kroon and R. A. Janssen, Adv. Funct. Mater., 15, 1703 (2005).

[1.56] C. Y. Kwong, A. B. Djurisic, P. C. Chui, K. W. Cheng and W. K.Chan, Chem. Phys. Lett., 384, 372 (2004).

[1.57] P. Ravirajan, A. M. Peiro, M. K. Nazeeruddin, M. Graetzel, D. C. Bradley and J. R. Durrant, J. Phys. Chem. B, 110, 7635 (2006).

[1.58] E. Arici, H. Hoppe, F. Schaffler, D. Meissner, M. A. Malik and N. S.Sariciftci, Thin Solid Films, 451, 612 9 (2004).

[1.59] D. Cui, J. Xu, T. Zhu, G. Paradee, S. Ashok and M.Gerhold, Appl. Phys. Lett., 88, 183111 (2006).

[1.60] E. Kymakis, E. Koudoumas, I. Franghiadakis and G. A. J. Amaratunga, J. Phys. D: Appl. Phys., 39, 1058 (2006).

Chapter 2
Organic solar cell fundamentals

OSCs are based on organic materials that have semiconductor properties. In 1977，the conductivity and semi-conductivity of polymers were discovered [2.1]. This opened the research on organic molecules and polymers for classical semiconductor applications, such as transistors, light emitting diodes and solar cells. Now there have been various organic semiconductor materials. In spite of their broad variation of chemical structures and practical applications, they have common properties which are different from the traditional inorganic materials. In this chapter, we will compare the organic semiconductor materials with the traditional inorganic semiconductor materials and then introduce the fundamental properties of organic semiconductors. These properties determine the basic operation principles and the device structures of OSCs. These various structures of OSCs and their corresponding limiting factors will be discussed. The experimental and characterization methods will also be introduced in this chapter.

2.1 Excitons in organic semiconductor materials

Light absorption in semiconductor materials is able to excite an electron from an occupied state below the bandgap to an available state above the bandgap. However, there are some differences in this process between the inorganic and organic materials. As is well known, the free electrons and holes are usually generated immediately in inorganic semiconductor materials (such as Si) upon light absorption under the normal condition. The generated free carriers distribute throughout the bulk according to the

exponential decrease of the incident light density. However, instead of the immediately generation of free charges, excitons are usually produced in organic materials upon light absorption [2.2]. Exciton is an excited state in which the electron and hole are still tightly bound due to Coulombic attraction. Excitons are electrical neutral and the external electric field cannot drift them to move. And they usually move by diffusion. A good understanding of the exciton behaviors is the key to understand the operation principles of OSCs. Why excitons rather than free carriers are produced in organic materials can be interpreted by two main reasons [2.2]:

(1) Compared to most inorganic semiconductors (dielectric constant, ε_r>10), the dielectric constant of the organic materials is usually low (ε_r≈2-4). Thus the attractive Coulombic potential in organic materials is very large and extends over a greater volume than it does in inorganic semiconductors. The typical exciton binding energies (E_B) of photogenerated electron-hole pairs in inorganic semiconductors are typically far below k_BT (k_B is Boltzmann's constant, T is temperature, and k_BT is 26 meV at room temperatures) such that free charge carriers are generated upon photo-excitation due to thermal dissociation. While for organic materials, E_B is far larger than k_BT and is localized on a few polymer repetition units or a molecule [2.3]. This fundamental difference of E_B between organic and inorganic materials is schematically illustrated in Fig. 2.1.

(2) The noncovalent electronic interactions between organic molecules are weak, resulting in a narrow bandwidth compared to the strong interatomic electronic interactions of covalently bonded inorganic semiconductor materials like silicon. The

electron's wave function is spatially restricted, allowing it to be localized in the potential well of its conjugate hole (and vice versa).

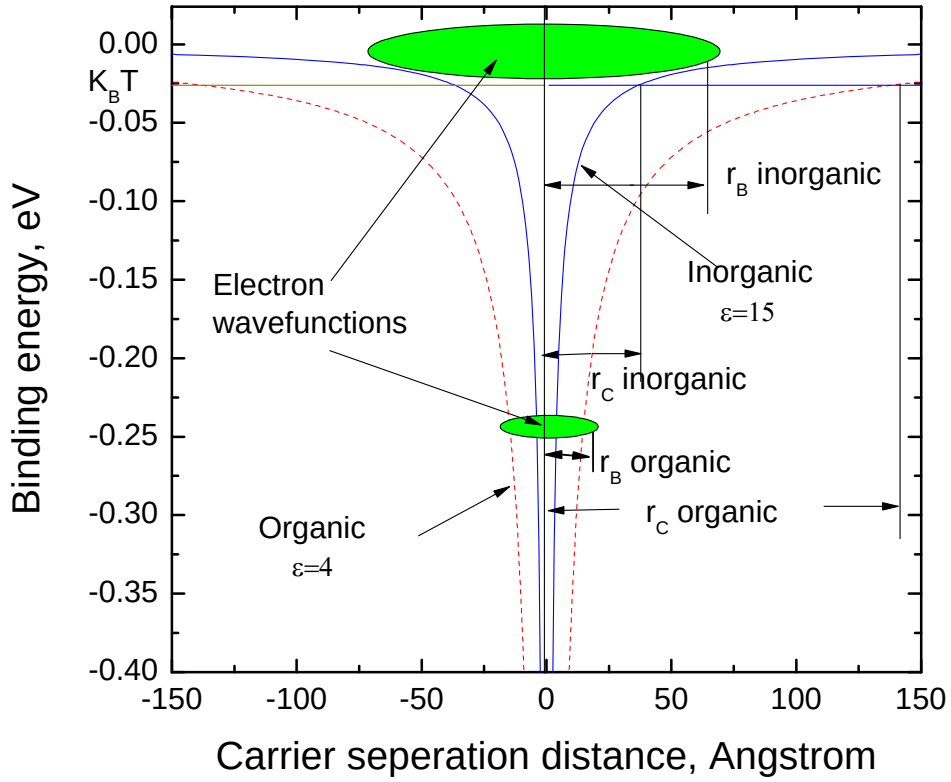

Fig. 2.1 A schematic plot of the fundamental difference between organic and inorganic semiconductors (replotted from [2.2] and [2.4]). A positive charge (hole) is at the origin and a negative charge (electron) at the indicated distance from the hole. Potential wells were calculated for a typical inorganic semiconductor with an isotropic dielectric constant ε_r =15 and a typical organic semiconductor (ε_r =4) assuming point charges. It shows that in most conventional inorganic semiconductors, free charge carriers are generated upon photoexcitation, because the electron wavefunction extends further than r_C, i.e. the radius of the Coulomb potential at k_{BT}. However, in organic semiconductors the photogenerated electron-hole pair is electrostatically bound. When $\gamma = r_C/r_B > 1$, the wave function of the electron is spatially restricted and "fit" deep into the potential well, i.e. is less delocalized. This leads to photoproduction of bound electron-hole pairs, or excitons.

Because excitons are usually produced in organic materials, they can be categorized to excitonic semiconductors. Whether a material belongs to the conventional semiconductor or excitonic semiconductor can be judged by the following criterion. This is done by the ratio of r_C (the width of the coulombic potential well at k_BT) and r_B (the Bohr radius of the relevant charge carrier) [2.4]:

$$\gamma = \left(\frac{r_C}{r_B}\right) \approx \left(\frac{q^2}{4\pi\varepsilon_0 k_B r_0 m_e}\right)\left(\frac{m_{eff}}{\varepsilon_r^2 T}\right) \tag{2.1}$$

where q is the electronic charge, ε_0 the permittivity of free space, r_0 the first Bohr radius of an electron of the hydrogen atom, m_e the electron rest mass and m_{eff} the effective electron mass in the semiconductor. If $\gamma > 1$, an excitonic behavior can be observed, which is the usual case in organic materials as shown in Fig. 2.1.

2.2 Other differences between organic and inorganic materials

Besides the generation of excitons in organic materials, there are some other properties of organic materials which are different from the conventional inorganic materials. A summary of the differences between organic and inorganic semiconductors is shown in Table 2.1. The inorganic material is represented by crystalline silicon since it is the dominant material in the conventional inorganic semiconductors.

Table 2.1 Main differences between crystalline silicon and organic semiconductors.

Materials	Crystalline silicon	Organic semiconductors
Basic entities	atoms	molecules
Bulk structure	crystalline	amorphous
Produced particles upon light	free carriers	excitons
Carrier mobility μ ($cm^2V^{-1}s^{-1}$)	electron: 1500 hole:450	<<0.1
Transport mechanism	band transport	hopping
Transport property	bipolar conduction	unipolar conduction
T dependence of mobility	T↑→ μ ↓	T↑→ μ ↑
Optical excitation energy gap (E_{go} eV)	1.1	≈2
Absorption coefficient near E_{go} (cm^{-1})	$\approx 10^3$	$\approx 10^5$
Dielectric constant	11.9	≈2-4
$\gamma = r_C/r_B$	<1	>1
Exciton binding energies 300K (meV)	<26	>100

2.3 Basic working principles of OSCs

Exciton consists of one electron and one hole. Due to the electrical neutrality, excitons cannot contribute to the photocurrent. In order to convert light into electrical energy, the excitons must firstly be dissociated into free carriers. This determines the basic working principles in OSCs. Generally there are four separate steps for OSCs to finish the energy conversion as shown in Fig. 2.2.

(1) Light absorption and exciton generation

(2) Exciton diffusion

(3) Exciton dissociation and free carrier generation

(4) Free carrier transport and collected by the electrodes

In the following sections, the four separate steps will be discussed.

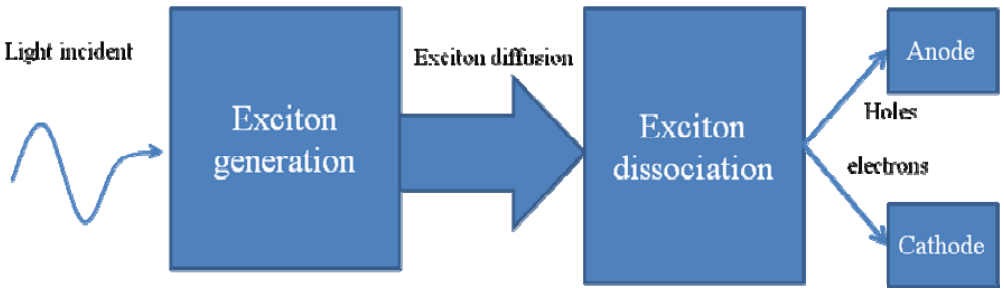

Fig. 2.2 Illustration of the basic operation principles in OSCs. Generally, there are four separate steps.

2.3.1 Light absorption

The light absorption is directly related to J_{SC} and determines the performance of OSCs. Primarily, high broadband light absorption is desired for the organic materials to be able to absorb most of the solar light. The absorption ability of the organic material is determined by the optical excitation energy gap (E_{go}). Here "E_{go}" is used instead of the conventional "electronic energy gap" (E_{ge}), since a tightly bound exciton, instead of a free electron and hole, is produced in the organic material. E_{ge} typically refers to the energy gap between the free holes at valence band and the free electrons at conduction band in inorganic semiconductors. The E_{go} and E_{ge} have the relationship

$$E_{ge} = E_{go} + E_B \tag{2.2}$$

E_B is the exciton binding energy with its value between 0.05–2 eV [2.7-2.12]. The widely used conjugated polymers in OSCs have E_{go} higher than 2.0 eV (for example, the widely used PPV and polythiophene materials). However, the solar spectrum extends well into the infrared region. As shown in Fig. 2.3, more than 60% of the total solar energy is in the wavelength region above 600 nm, which corresponds to E_{go} below 2.0 eV. For terrestrial applications, it is desirable that E_{go} of a solar cell material spans a range from 1.3 eV to 2.0 eV. Thus the "photon loss" problem due to the limited absorption of organic materials is very common in almost all the currently reported organic PV materials and devices. The light absorption (or exciton generation) of the state-of-art OSCs is still far from being optimized. To reduce the "photon loss", a number of recent studies have worked on the development of low band gap conjugated polymers [2.13-2.15]. Another effective way to improve the light absorption ability is the novel structure design, such as various tandem structures [2.14-2.16].

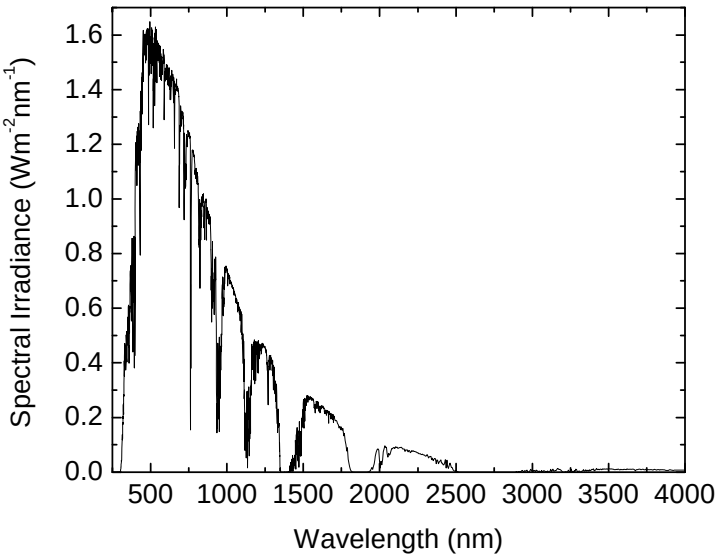

Fig. 2.3 The solar spectrum (AM 1.5) [2.17].

2.3.2 Exciton migration

After an exciton is photo-generated, it can migrate by diffusion. At the same time, the exciton can also decay radiatively or non-radiatively to the ground sate. The lifetime of excitons is at typically pico- to nano-seconds [2.18, 2.19]. This makes the exciton diffusion length (L_D) very small. For polymer materials, L_D is measured to be about 10 nm [2.20-2.22], which is smaller in comparison to the layer thickness of polymer films usually used in OSCs (>80 nm). Some small molecules have larger exciton L_D. Table 2.2 shows L_D of some small molecules. Polyacenes (eg. pentacene and tetracene) and metal phthalocyanines (MePc) (eg. CuPc) show L_D to be approximately 50 nm and 10 nm, respectively. C_{60} shows L_D of 40 nm. The long L_D materials can be used for the layered structure, where the film thickness is alleviated by the long L_D; while for the small L_D materials, the bulk HJ structure is desired, which effectively shortens the diffusion distance before the exciton dissociation. MePC materials have relatively small L_D (around 10 nm), but the large light absorption ability makes the active layer thickness very small and then they can be used in layered structures (see Table 1.1). The discussion for the different structures will be given in section 2.4.

Table 2.2 Summary of optical and electrical properties of some small organic materials in OSCs.

Material	Ionization potential (IP, eV)	Electron affinity (EA, eV)	E_{go} (eV)	Mobility ($cm^2V^{-1}s^{-1}$)	L_D (nm)	Ref.
C_{60}	6.2	3.6	1.8	5.1×10^{-2}	40 ± 5	2.23,2.24,2.25
CuPc	5.2	3.2	1.7	7.4×10^{-4}	10 ± 3	2.24,2.25,2.26
Pentacene	5.1	3.0	1.9	1.5×10^{-1}	65 ± 16	2.26,2.27
PTCBI	6.2	3.6	1.7	2.4×10^{-6}	3 ± 0.3	2.24,2.25,2.26

2.3.3 Exciton dissociation

For the solar cell application, excitons must be dissociated into free electrons and holes. Such a process can be induced by the built-in electric field, but the efficiency at electric fields typically found in organic electronic devices (F~10^6 V/cm) is low (η_D ~10%) [2.25]. Electronic trap sites in the bulk can also dissociate the exciton into one trapped carrier and one free carrier, but this is not a viable mechanism for efficient photoconversion [2.2]. It has been recognized that the most efficient exciton dissociation in organic materials occurs at a D/A interface [2.28, 2.29]. In order to dissociate the excitons, some energy is needed. This is efficiently supplied by the offset energy at the D/A interface. Fig. 2.4 shows the energy level alignment requirements for efficient charge transfer from the photoinduced state to take place [2.25]. The D material has a lower ionization potential (IP) given by HOMO level, while the acceptor material has a high electron affinity (EA) given by LUMO level. Then the offset energy is given by IP_D-EA_A (the subscripts denote the D and A materials). For Fig. 2.4 (a), the D/A HJ has

$$E_{go} > IP_D\text{-}EA_A \tag{2.3}$$

The charge-transfer reactions will take place:

$$D^* + A \rightarrow D^+ + A^- \tag{2.4}$$

$$D + A^* \rightarrow D^+ + A^- \tag{2.5}$$

Where D* and A* are donor and acceptor excited states, and D^+ and A^- are hole and electron polarons in the donor and acceptor materials. However, for Fig. 2.4 (b), the D/A HJ has

$$E_{go} < IP_D\text{-}EA_A \tag{2.6}$$

such that the charge-transfer reaction is energetically unfavorable.

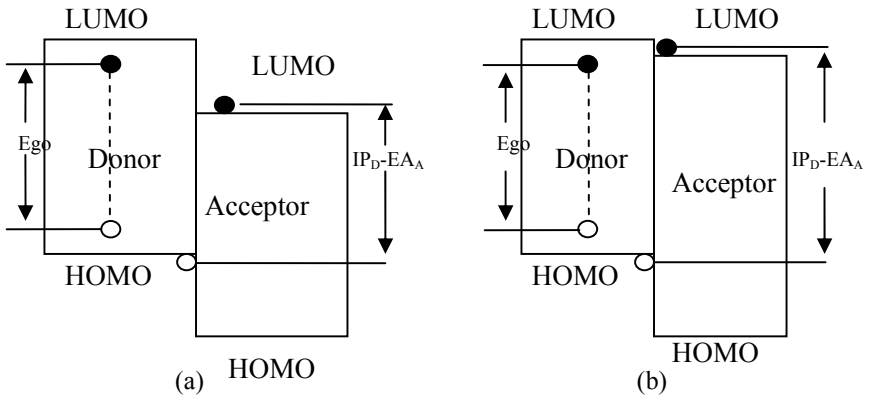

Fig. 2.4 Schematic illustration of the energy level alignment requirements of D/A HJ for charge transfer from the photoinduced state to take place. (a) efficient D/A energy offset and (b) inefficient D/A energy offset.

The dissociation typically occurs in the time scales of a few hundred femto-seconds or less [2.30, 2.31]. This is much shorter than any other competing process and assures the efficient dissociation at D/A HJ interfaces. After exciton dissociation, the device must assure that the electron and hole remain separated. This may be achieved by creating paths that selectively transport one type of carriers but block the other type of carriers.

2.3.4 Carrier transport

Once the excitons are separated, the holes need to transport toward the anode and electrons transport toward the cathode. The driving forces may come from the field created by the work function difference between the two electrodes as well as the "chemical potential" driving force [2.32]. With the chemical potential force, even if the two electrode are the same (the driving force due to work function difference is zero), the PV effect still can be observed [2.2, 2.32].

The mobilities of organic semiconductors are typically several orders of magnitude less than those found in crystalline inorganic semiconductors (Table 2.1). This is because of the weak order in organic materials. In the weakly ordered organics, intermolecular forces are too weak to form well-defined conduction and valence bands. Thus the charges must hop between local states in contrast to the band transport in most crystalline inorganic semiconductors. Mobility is also limited by the confinement of the charge to the lattice. Once the exciton is dissociated, it relaxes to form a lattice distortion (polaron). In order for the polaron to migrate along the polymer backbone, it must possess enough energy to overcome the energy barrier associated with rearranging that distortion. The polaron has a large effective mass and thus is poorly mobile.

The low mobilities in organic semiconductors limit the feasible thicknesses of the organic layer in solar cells to a few hundred nanometers. Fortunately, organic semiconductors are very strong absorbers in the UV-VIS regime (Table 2.1). Thus only very thin organic layers (~100 nm) are needed for effective absorption.

2.4 OSCs structures

The above section has introduced the working principles of OSCs. Based on these working principles, several device structures have been proposed in the past few decades. The main difference among these structures is how they deal with the process of exciton dissociation and charge transport. In the following, these structures will be introduced.

2.4.1 Single layer structure

In this structure, a single organic layer is sandwiched between two different electrode materials. The PV behavior of these devices can be explained by the MIM

model (for insulators) or by the formation of a Schottky barrier (for doped materials) [2.33]. As shown in Fig. 2.5, the excitons are dissociated at metal/organic (M/O) interface for the MIM case or dissociated by the high electric field near the contact for the Schottky barrier case. Single layer structure is the simplest structure and can achieve a very high open circuit voltage in excess of 1V [2.34]. Earlier work mainly focused on this type of structure [2.35, 2.36]. However this structure suffers from very low PCE.

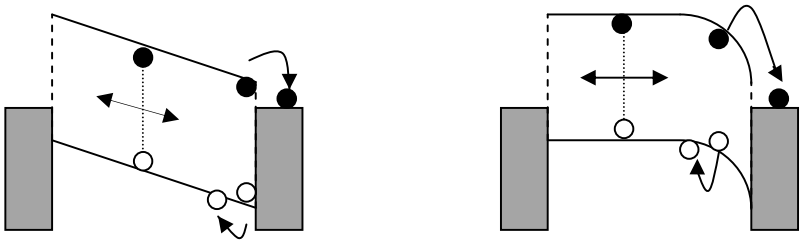

Fig. 2.5 Energy band diagram of a single layer organic PV device; (a) MIM picture and (b) Schottky picture.

The low PCE is due to the very short exciton diffusion length for most OSC materials and the low exciton dissociation probability. Dissociation of the excitons only occurs in a restricted zone near the metal contacts. Most of the excitons, which are not generated in this zone, recombine without contribution to any external photocurrent. Thus, J_{SC} of this structure device is usually very low. In addition, the series resistances in this structure are large. Thus this structure shows a low fill factor (FF) and a field-dependent charge carrier collection. These thin film devices with the single layer structure can work well as photodetectors, as under a high reverse bias the electric field drives the charges to the electrodes. However, they most probably will not result in any practical PV application.

2.4.2 Heterojunction structure

As discussed in the single layer structure, the main limits for PCE are the very short exciton diffusion length and the limited exciton dissociation sites (only near the contact). In order to overcome these shortcomings, D/A interface is introduced to OSCs. As has been discussed in section 2.3.3, the exciton dissociation at D/A HJ interface is ultrafast and efficient. The introduction of D/A HJ interfaces effectively increases the device performance and becomes the "driving force" of the development of OSCs in the past two decades. There are mainly two types of HJ solar cells: layered HJ solar cells and bulk HJ solar cells.

Layered HJ solar cells

With the introduction of an electron acceptor layer in the device, a planar HJ interface is formed as shown in Fig. 2.6. At the D/A interface, there is a large potential drop, and there the excitons can be effectively dissociated. In this structure, the four separate working steps are very clear as shown in Fig. 2.6. Excitons are generated and diffuse within both D and A materials. If they encounter the organic D/A interface, a fast dissociation takes place. After the exciton dissociation, the recombination rate between holes in D and electrons in A is several orders of magnitude smaller than the forward charge transfer rate [2.37, 2.38]. Then the holes and electrons can be effectively separated from each other. A good matching of the work function of the cathode to LUMO of A and anode to HOMO of D yields optimal electron collection of the free carriers.

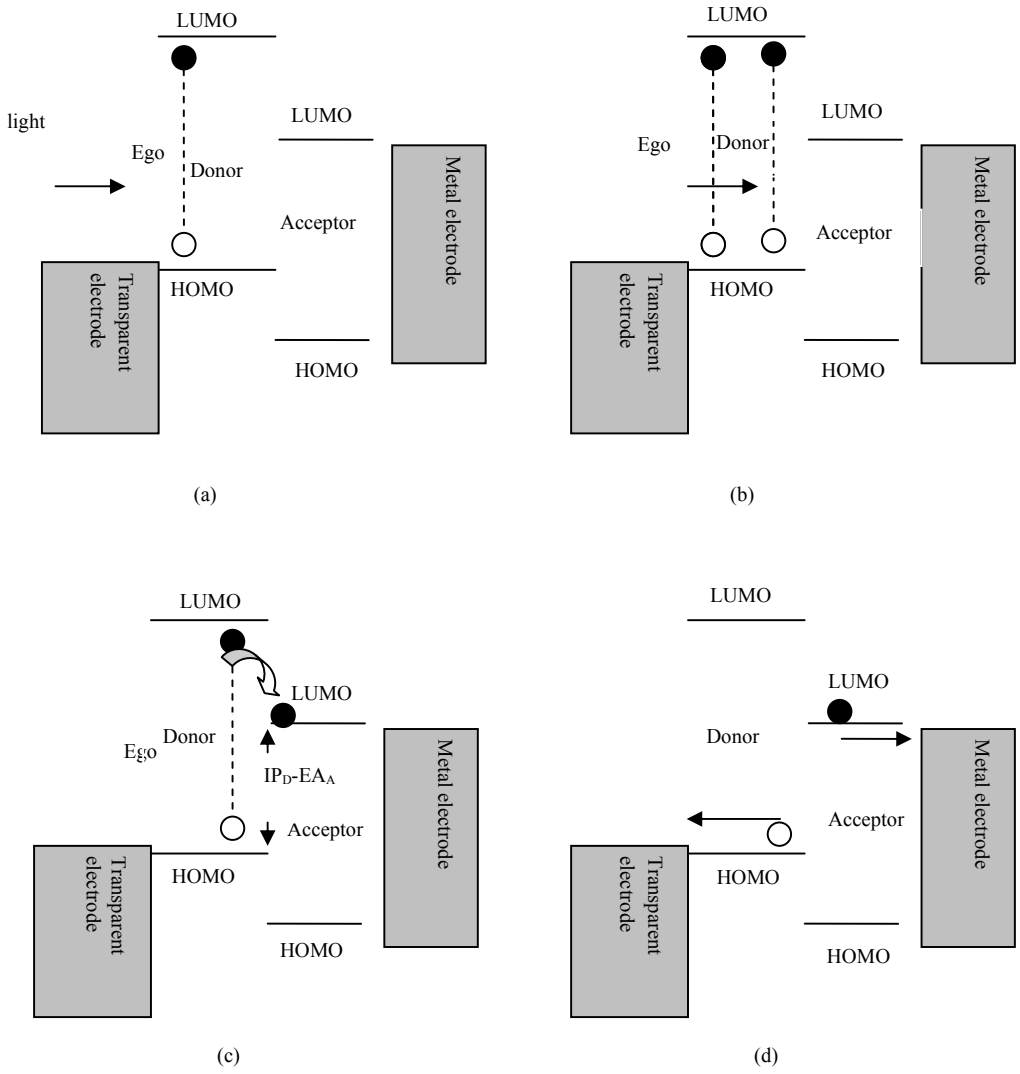

Fig. 2.6 Very clear consecutive steps in the generation of photocurrent of layered HJ OSCs: (a) Exciton generation, (b) Exciton migration, (c) Exciton dissociation and (d) Free carrier transport.

Compared to the single layer device, the exciton dissociation at the D/A interface is more effective than that at M/O interface. After the excitons are dissociated at the D/A

interface, the electrons transport within the A material, and the holes transport within the D material. Then holes and electrons are effectively separated from each other, thus the recombination rate can be greatly reduced. At the same time, the charge transport is usually not a problem in this structure and the charge collection can be reached to 100% [2.25]. The photocurrent dependency on illumination intensity can be linear [2.39-2.41], and a large FF can be achieved [2.42].

However, in order to contribute to the photocurrent, excitons must pass a long distance and reach the D/A interface before recombination. Only the excitons in the L_D region near the D/A interface can be dissociated. Thus most of the excitons outside this region are lost and have no contribution to the photocurrent. To solve this problem, the bulk HJ structure has been proposed.

Bulk HJ solar cells

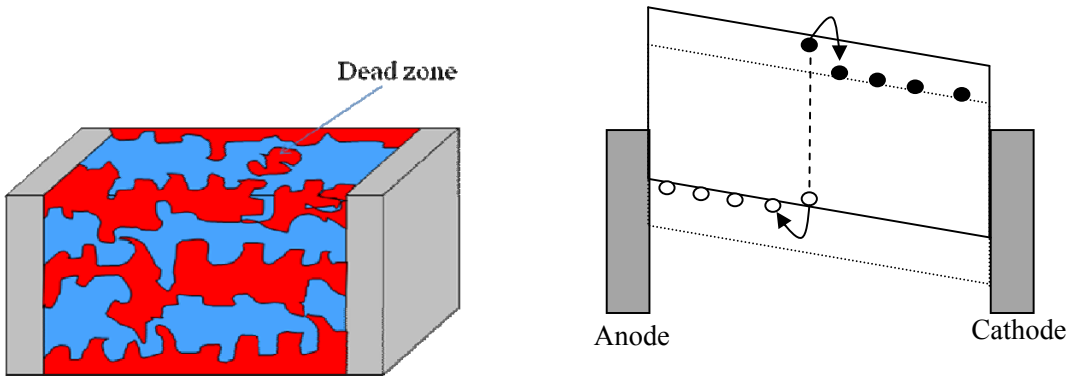

Fig. 2.7 Bulk HJ PV cells. In this structure, D and A are mixed together and form the interpenetrating network. The produced excitons can be dissociated efficiently.

The bulk HJ is formed by intimately mixing the D and A components in a bulk volume. As shown in Fig. 2.7, in this structure, the D/A interfaces are distributed overall

the active layer, so that almost all the excitons can reach the D/A interface within the distance of L_D. Compared to layered structure, bulk HJ structure effectively increases the D/A interface area, and thus the exciton loss is avoided. After the exciton dissociation, the charges are separated within the different D and A phases. And if continuous pathways exist throughout the mixed layer, light-generated charges can travel along these respective phases towards the external contacts. Like the layered structures, the photocurrent also has a linear or sublinear relation with the light intensity [2.43].

From the above discussion, it is very clear that the morphology, the actual mixing of the two materials in the active layer, has a very important influence on performance of bulk HJ solar cells. As shown in Fig. 2.7 (a), some zones may not be included in the interpenetrating network. As a result, the carriers in this region cannot be collected by the electrodes, thus the "dead zone" is formed in the active layer. In the optimal case, it should guarantee an efficient mixture of D and A (for exciton dissociation) and an easy transport of charges via the percolation at the same time. If the domains are too large, separation will not be efficient. If the domains are too small, recombination of free charges may be favored and charge transport may be hindered. Many methods have been studied to improve the performance of bulk HJ solar cells. For example, P3HT can crystallize and achieve a higher hole mobility by thermal annealing [2.47-2.51]. It has also been demonstrated that the characteristics of solvent used, such as its evaporability, play an important role in the morphology formation of the photoactive layer [2.52-2.54].

2.4.3 Tandem structure

Although OSCs have been developed fast in the past decade, PCE is still low compared to their inorganic counterparts. One main reason is the limited overlap between

the organic absorber and the solar spectrum [2.55, 2.56]. The tandem structure is designed to overcome this problem. In this structure, the devices are stacked on the top of each other and connected in series (Fig. 2.8 (a)-increase V_{OC}) or in parallel (Fig. 2.8 (b)-increase J_{SC}). By combining different organic materials with complementary absorption spectra in tandem cell [2.57, 2.58], it can improve the spectral coverage and increase the photon harvesting. The tandem solar cells can be categorized into three groups:

(1) the low molecular weight molecules are used for both the bottom and the top cells

(2) the polymers are used for both the bottom and the top cells

(3) hybrid tandem OSCs which include the low molecular weight molecules subcell and the polymer subcell.

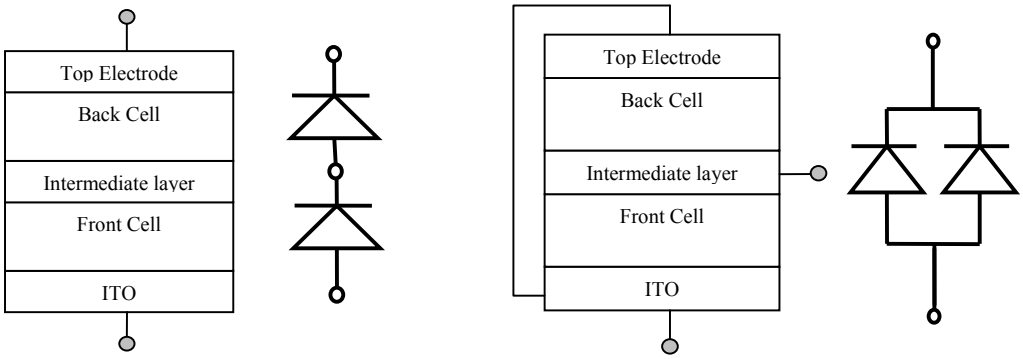

(a) Series connection (b) Parallel connection

Fig. 2.8 Tandem architectures and their equivalent circuits: (a) series connection-an increased open circuit voltage V_{OC} and (b) parallel connection-an increased short circuit current J_{SC}.

Tandem structure can effectively increase the overall absorption of OSCs. By using this structure, the performance is further improved. Recently, tandem solar cells have reached PCE as high as 6.5% [2.14]. The disadvantage for this structure is mainly their

complex fabrication process. Tandem solar cell connects two or more cells in one device. And the standalone cell is still the core of this type of solar cells.

2.5 Materials, experimental and device characterization methods

The bulk HJ solar cell is the most promising cell because it has the potential to guarantee the effective exciton dissociation and at the same time guarantee the efficient carrier transport by well optimizing the active layer morphology. Our work is mainly based on this structure. In this section, we will give a brief introduction to the materials and the experimental and characterization methods, which will be used in this study.

2.5.1 Materials

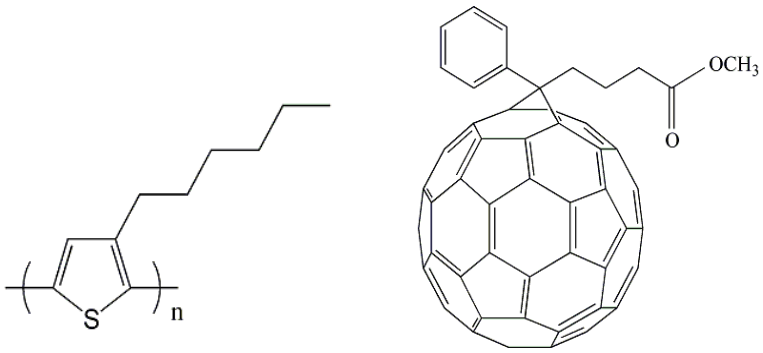

(a) (b)

Fig. 2.9 The chemical structure of a) P3HT and b) PCBM.

There are many organic materials which have been used in OSCs. Among them, P3HT (Fig. 2.9 (a)) shows obvious advantages over other materials. P3HT has reasonably high hole mobility. For pure films of P3HT, a value of the hole mobility in the range of μ_p = 0.2 to $10^{-3}cm^2V^{-1}S^{-1}$ [2.59, 2.60] was measured. Compared to the traditional poly(p-phenylene vinylene) materials, P3HT has an improved absorption. P3HT has other

advantages, such as the environmental stability. Till now, the highest PCE achieved in OSCs is based on P3HT (see Table 1.1).

For the acceptor material, the soluble fullerene PCBM is used. PCBM is a special spherical electron carbon cluster, whose chemical structure is shown in Fig. 2.9 (b). For pure films of PCBM, a value of the electron mobility in the range of 10^{-3} $cm^2V^{-1}s^{-1}$ [2.61] was measured.

2.5.2 Experimental method

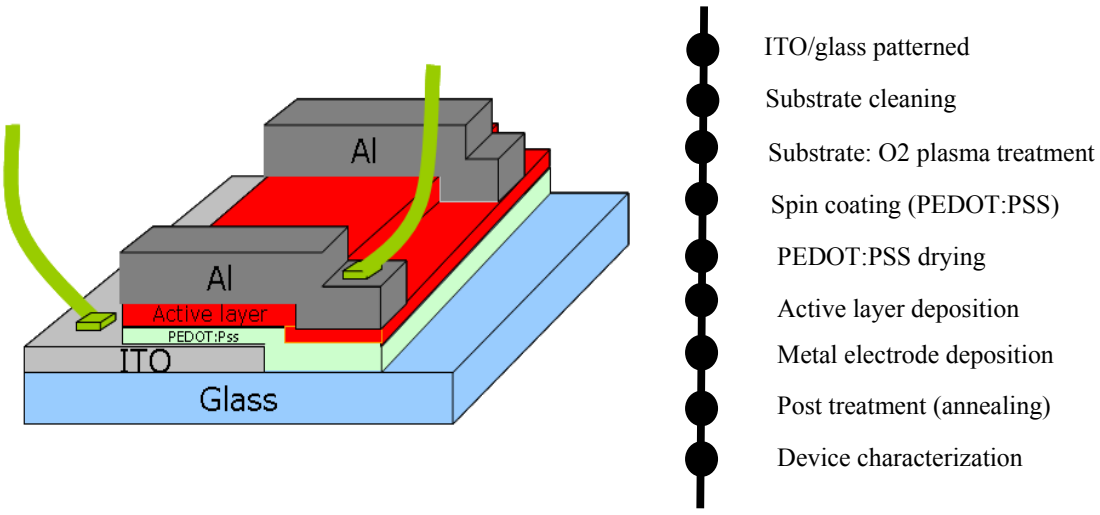

(a) (b)

Fig. 2.10 (a) Layer structure of our OSCs and (b) The production process flow.

Fig. 2.10 shows the layer structure and the process flow for the fabrication of OSCs. All of our devices are fabricated on the ITO/glass substrates. Before the fabrication, the substrates are patterned by etching the ITO film using concentrated hydrochloric acid

(HCl, 37%). After the patterns are formed, there are some particulates and adsorbed organic compounds on the substrates. The substrates must be cleaned carefully. The cleaning procedure is summarized in Table 2.3. After cleaning the substrate surface with the liquid solvents, it is usually to treat the substrate again by exposure to UV-ozone or O_2 plasma. This step can further remove absorbed organic particles, alter the work function and decrease the surface roughness. In our case, the substrates are treated by O_2 plasma for three minutes. Then the poly[3,4-ethylene-dioxy-thiophene]:poly[4-styrenesulphonate] (PEDOT:PSS, Baytron-P) are spin coated. PEDOT:PSS layer can facilitate the contact to the absorber layer, increase the work function of anode, and decrease the substrate roughness. After drying the substrates, the active layer was deposited. To prepare the active layer, the P3HT:PCBM solutions were prepared by dissolving the polymer, fullerene, or the polymer-fullerene blend in dichlorobenzen, and stirring for at last several hours in nitrogen glovebox. Then the metal electrode was deposited. At last, the devices were annealed and measured.

Table 2.3 Substrate treatment procedures

Solvent	Ttemperature	Time	Sonicate
Deionized Water +detergent	Room Temperature	15 mins	Yes
Deionized Water	Room Temperature	15 mins	Yes
Acetone	Room Temperature	15 mins	Yes
Iso-propanol	Room Temperature	15 mins	Yes

2.5.3 Device characterization

2.5.3.1 Absorption measurement

The absorption measurement gives the important information about the absorption ability of organic materials and determines which part of the wavelength can be absorbed by the materials. The information is essential for the design of the solar cells. Then it is one of the most useful measurements taken during characterization. Absorption spectra of organic films on glass were measured by a Shimadzu UV-3101 PC UV-VIS-NIR spectrophotometer. This is a straightforward measurement using two identical substrates, one with the organic film on, the other kept clean and used as a reference. By using this method, samples could be on varying substrates but only the absorbance of the film would be measured.

2.5.3.2 Current-voltage measurement

This measurement is done by applying a voltage sweep in the dark and under light illumination. For every voltage (V) applied to the sample, the current density (I) flowing through the sample is measured. The I-V curve is measured using a Keithley 2400 Source-Measure-Unit.

I-V characterization in the dark

From the measured I-V curve in the dark, some information can be derived. An example of the I-V curve for organic electronic devices in the dark is shown in Fig. 2.11. As is shown, the obvious rectifying characteristic is observed. This is attributed to the different M/O interface injection barriers at the forward and inverse biases (Fig. 2.11 inset).

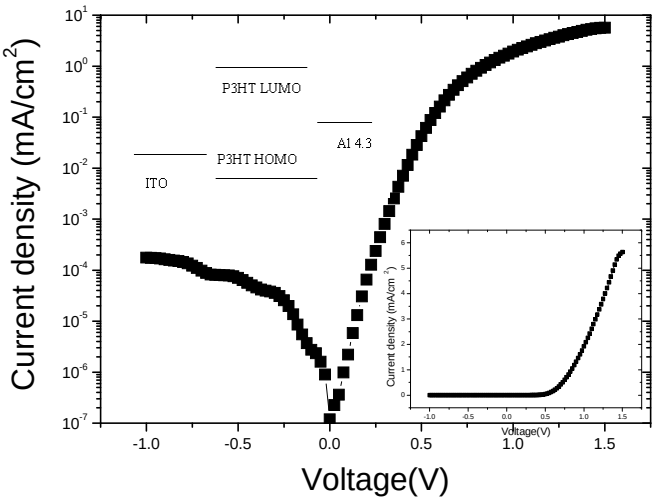

Fig. 2.11 Typical I-V curve for the organic electronic device. Inset: the linear scale graph and the band structure for this device of ITO/P3HT/Al.

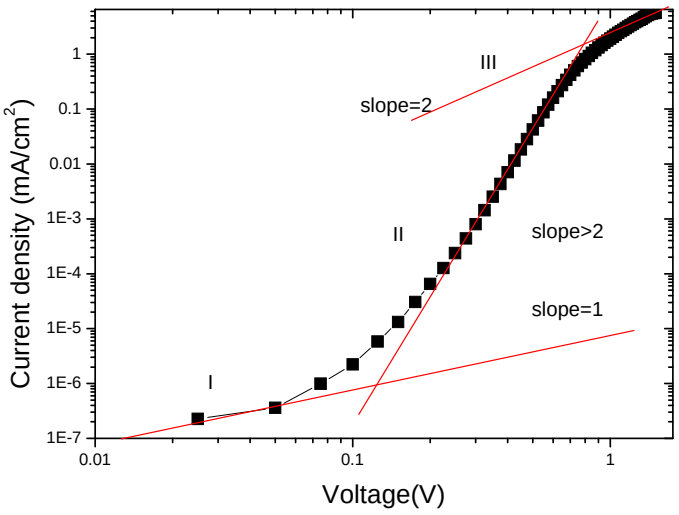

Fig. 2.12 Forward dark I-V characteristics in double logarithmic scale. The same device in Fig. 2.11. Region I, Ohmic conduction; Region II, ILC; Region III, SCLC.

From the dark I-V curve, the charge conduction in the organic materials can be investigated. Typically, three different conduction regions can be observed as shown in Fig. 2.12 by using the double logarithmic representation.

In region I (V < 0.1 V), the external electric field across the device is small and the carrier injection from the electrodes is blocked by the interface barrier. Hence the number of charge carriers participating in the current almost does not increase. Current depends on applied field and the conductivity of the material. Thus it obeys Ohm's law and has the slope of logI vs logV equal to 1. In region II (0.1 V <V< 0.7 V), the voltage applied has surpassed the threshold of blocking for carrier injection from the electrodes. The number of charges participating in the total current increases rapidly with the increase of voltage. At this region, the bulk material is still able to accommodate these rapid increased carriers. This leads to injection limited conduction (ILC) and has the slope of logI vs logV larger than 2. If the applied voltage is increased further, more carriers are injected from the electrodes so that the bulk material cannot accommodate so many carriers and then the space charge starts to form near the injecting electrode interface (SCLC). This is the region III which is indicated by the slope of logI vs logV equal to 2.

The minimum current ("current zero") is usually achieved when the voltage is zero as shown in Fig. 2.11. However, sometimes the shift of current zero can be observed. This is due to the traps in the organic materials [2.62].

I-V characterization under light illumination

I-V curve under light illumination is the most important characteristic for solar cells and it determines the device performance. A typical solar cell I-V curve measured

under light illumination is shown in Fig. 2.13. Several parameters are indicated on this curve.

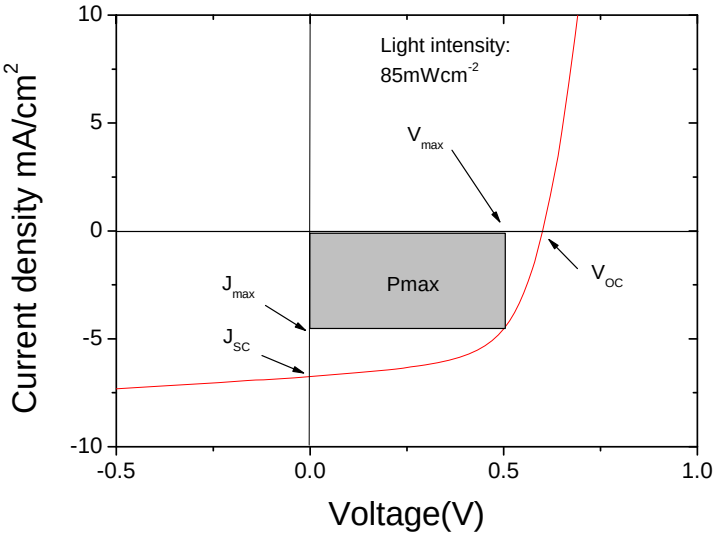

Fig. 2.13 A typical polymer/fullerene bulk HJ solar cell I-V curve measured in the dark and under light illumination (85mW/cm^2)

(I) The open-circuit voltage, V_{OC}, is the maximum photovoltage that can be generated in the cell and corresponds to the voltage where current is zero under light illumination.

(II) The short circuit current density, J_{SC}, is the current density when the applied voltage is zero.

(III) The fill factor (FF) is defined as

$$FF = \frac{(JV)_{\max}}{J_{SC}V_{OC}} \tag{2.7}$$

FF is a measure of the I-V curve. A rectangular shape gives a large FF.

(IV) The power conversion efficiency (PCE, η) is the ultimate measure of the device efficiency in converting photons to electrons. It can be defined as

$$\eta = \frac{J_{SC} V_{OC} FF}{P_{in}} = \frac{J_{\max} V_{\max}}{P_{in}} \tag{2.8}$$

P_{in} is the incident light power density. Efficiency is equal to the area of shadow rectangle divided by P_{in}.

I-V curve describes the macroscopic properties of OSCs. This characteristic can be described by

$$I = I_s \left(e^{\frac{q(V+R_S I)}{nk_B T}} - 1 \right) + \frac{V - R_S I}{R_{Sh}} - I_{ph}, \tag{2.9}$$

where I_{ph} is photocurrent, I_s the reverse saturation current of the diode, R_s the series resistance, R_{sh} the shunt resistance, n the ideal factor. By fitting the curve, all the parameters can be extracted.

Besides the electrical characterization, other methods such as tapping mode atomic force microscopy (AFM), x-ray photoelectron spectroscopy (XPS) and X-ray diffraction (XRD) are also used.

2.6 Summary

Due to the low dielectric constant and weak noncovalent electronic interactions between the molecules, excitons rather than free carriers are produced in the organic materials upon light absorption. These excitons play a very important role in the working principles of OSCs. Generally, to convert the light into electric current there are four

separate steps: light absorption (exciton generation), exciton diffusion, exciton dissociation (charge generation) and charge transport. Depends on the ways of dealing with the exciton dissociation and charge transport processes, there are different structure designs: single layer device, layered HJ device and bulk HJ device. Among them, the bulk HJ solar cell is the most promising cell because it has the potential to guarantee the effective exciton dissociation and at the same time the efficient carrier transport by optimizing the active layer morphology. Therefore, this is the structure of our focus. At last of this chapter, the materials, the experimental and device characterization methods are addressed.

References

[2.1] H. Shirakawa, E. J. Louis, A. G. Macdiarmid, and A. J. Heeger. J. Chem. Soc. Chem. Com., 16, 578 (1977).

[2.2] B. A. Gregg and M. C. Hanna, J. Appl. Phys., 93, 3605 (2003).

[2.3] C. J. Brabec, V. Dyakonov, J. Parisi, and N. S. Sariciftci, Organic Photovoltaics: Concepts and Realization. Springer, Berlin, 1 edition, 2003.

[2.4] S. E. Gledhill, B. Scott, and B. A. Gregg, J. Mater. Res., 20, 3167 (2005).

[2.5] M. Knupfer, Appl. Phys. A, 77, 623 (2003).

[2.6] I. G. Hill, A. Kahn, G. Soos, and R. A. Pascal, Chem. Phys. Lett., 217, 181 (2000).

[2.7] M. Knupfer, H. Peisert, and T. Schwieger, Phys. Rev. B, 65, 033204 (2002).

[2.8] S. F. Alvarado, P. F. Seidler, D. G. Lidzey, and D. D. C. Bradley, Phys. Rev. Lett., 81, 1082 (1998).

[2.9] M. Knupfer, J. Fink, E. Zojer, G. Leising, U. Scherf, and K. Mullen, Phys. Rev. B, 57, R4202 (1998).

[2.10] S. Barth and H. Bassler, Phys. Rev. Lett., 79, 4445 (1997).

[2.11] C. J. Brabec, C. Winder, N. S. Sariciftci, J . C. Hummelen, A. Dhanabalan, P . Hal and R. A. J. Janssen, Adv. Func. Mater., 12, 709 (2002).

[2.12] I. Polec, A. Henckens, L. Goris, M. Nicolas, M. A. Loi, P. J.Adriaensens, L. Lutsen, J. V. Manca, D. Vanderzande and N. S. Sariciftci, J. Polym. Sci., Part A: Polym. Chem., 41, 1034 (2003).

[2.13] S. Sun and N. S. Sariciftci (eds.), Organic Photovoltaics: Mechanisms, Materials and Devices, CRC Press, Boca Raton (2005).

[2.14] J. Y. Kim, K. Lee, N. E. Coates, D. Moses, T. Q. Nguyen, M. Dante, and A. J. Heeger, Science, 317, 222 (2007).

[2.15] A. G. F. Janssen, T. Riedl, S. Hamwi, H.-H. Johannes, and W. Kowalsky, Appl. Phys. Lett., 91, 073519 (2007).

[2.16] G. Dennler, H. J. Prall, R. Koeppe, M. Egginger, R. Autengruber, and N. S. Sariciftci, Appl. Phys. Lett., 89, 073502 (2006).

[2.17] The solar spectrum (AM 1.5): http://rredc.nrel.gov/solar/spectra/ .

[2.18] T. Stubinger and W. Brutting, J. Appl. Phys., 90, 3632 (2001).

[2.19] H. Amerongen, L. Valkunas and R. Grondelle (eds.), Photosynthetic Excitons, World Scientific, Singapore (2000).

[2.20] T. Stubinger and W Brütting. J. Appl. Phys., 90, 3632 (2001).

[2.21] H. R. Kerp, H. Donker, R. B. M. Koehorst, T. J. Schaafsma, and E. E. Van Faassen. Chem.Phys. Lett., 298, 302 1998.

[2.22] A. Haugeneder, M. Neges, C. Kallinger, W. Spirkel, U. Lemmer, J. Feldmann, U. Scherf, E. Harth, A. Gugel, and K. Mullen. Phys. Rev. B, 59, 15346 1999.

[2.23] P. J. Benning, D. M. Poirier, T. R. Ohno, Y. Chen, M. B. Jost, F. Stepniak, G. H. Kroll, J. H. Weaver, J. Fure, R. E. Smalley Phys. Rev. B, 45, 6899 (1992).

[2.24] B. P. Rand, J. Xue, S. Uchida and S. R.Forrest, J. Appl. Phys., 98, 124902 (2005).

[2.25] P. Peumans, A. Yakimov and S. R.Forrest, J. Appl. Phys., 93, 3693 (2003).

[2.26] A. Kahn, N. Koch and W. Y. Gao. J. Polymer Sci. Part A, 41, 2529 (2003).

[2.27] S. Yoo, B. Domercq and B. Kippelen. Appl. Phys. Lett., 85, 5427 (2004).

[2.28] G. Yu, J. Gao, J. Hummelen, F. Wudl, and A. J. Heeger, Science, 270, 1789 (1995).

[2.29] J. J. M. Halls, C. A. Walsh, N. C. Greenham, E. A. Marseglia, R. H. Friend, S. C. Moratti, and A. B. Holmes, Nature (London), 376, 498 (1995).

[2.30] P. A. van Hal, R. A. J. Janssen, G. Lanzani, G. Cerullo, M. Zavelani-Rossi, and S. D. Silvestri, Chem. Phys. Lett., 345, 33 (2001).

[2.31] B. C. Zerza, G. Cerullo, S. D. Silvestri, and N. S. Sariciftci, Synth. Met., 119, 637 (2001).

[2.32] B. Gregg, J. Phys. Chem. B., 107, 4688 (2003).

[2.33] H. Hoppea and N. S. Sariciftci, J. Mater. Res., 19, 1924 (2004).

[2.34] X. Wei, M. Raikh, Z. V. Vardeny, Y. Yang and D. Moses, Phys. Rev. B, 49, 17480 (1994).

[2.35] B. R. Weinberger, M. Akhtar and S. Gau, Synth. Met., 4, 187 (1982).

[2.36] S. Gemos. G. Tourillon and F. Garnier, Thin solid films, 139, 221 (1986).

[2.37] G. Zerza, C. J. Brabec, G. Cerullo, S. D. Silvestri, and N. S. Sariciftci, Synth. Met., 119, 637 (2001).

[2.38] A. F. Nogueira, I. Montari, J. Nelson, J.R. Durrant, C. Winder, N.S. Sariciftci, and C. Brabec, J. Phys. Chem. B, 107, 1567 (2003).

[2.39] L. A. A. Pettersson, L.S. Roman, and O. Inganas, J. Appl. Phys., 86, 487 (1999).

[2.40] N. S. Sariciftci, D. Braun, C. Zhang, V. I. Srdanov, A. J. Heeger, G. Stucky, and F. Wudl, Appl. Phys. Lett., 62, 585 (1993).

[2.41] J. Rostalski and D. Meissner, Sol. Energy Mater. Sol. Cells, 63, 37 (2000).

[2.42] C.W. Tang, Appl. Phys. Lett., 48, 183 (1986).

[2.43] P. Schilinsky, C. Waldauf, and C.J. Brabec, Appl. Phys. Lett., 81, 3885 (2002).

[2.44] D. Gebeyehu, M. Pfeiffer, B. Maennig, J. Drechsel, A. Werner, and K. Leo, Thin Solid Films, 451, 29 (2004).

[2.45] E. A. Katz, D. Faiman, S.M. Tuladhar, J.M. Kroon, M.M. Wienk, T. Fromherz, F. Padinger, C. J. Brabec, and N. S. Sariciftci, J. Appl. Phys., 90, 5343 (2001).

[2.46] V. Dyakonov, Physica E, 14, 53 (2002).

[2.47] F. Padinger, R. S. Rittberger and N. S. Sariciftci, Adv. Funct. Mater., 13, 85, (2003).

[2.48] F. Yang, M. Shteina and S. R. Forrest, J. App.l Phys., 98, 014906 (2005).

[2.49] X. N. Yang, J. K. J. van Duren and J. Loos, Macromolecules, 37, 2151 (2004).

[2.50] J. S. Huang, G. Li and Y. Yang, Appl. Phys. Lett., 87,112105 (2005).

[2.51] W. Ma, C. Yang, X. Gong, K. Lee and A. J. Heeger, Adv. Funct. Mater., 15, 1617 (2005).

[2.52] S. E. Shaheen, C. J. Brabec and N.S. Sariciftci, Appl. Phys. Lett., 78, 841 (2001).

[2.53] X. N. Yang, J. K. J. van Duren , M. T. Rispens, J. C. Hummelen, R. A. J. Janssen, M. A. J. Michels, and J. Loos, Adv. Mater., 16, 802, (2004).

[2.54] T. Martens, J. D Haen, T. Munters, Z. Beelen, L. Goris, J. Manca, M. D. Olieslaeger, D. Vanderzande, L. De Schepper, and R. Andriessen. Synth. Met., 138, 243 (2003).

[2.55] B. P. Rand, J.G. Xue, F. Yang and S.R. Forrest, Appl. Phys. Lett., 87, 233508 (2005).

[2.56] A.G. F. Janssen, T. Riedl, S. Hamwi, H.-H. Johannes, and W. Kowalsky, Appl. Phys. Lett., 91, 073519 (2007).

[2.57] G. Dennler, H. J. Prall, R. Koeppe, M. Egginger, R. Autengruber, and N. S. Sariciftci, Appl. Phys. Lett., 89, 073502 (2006).

[2.58] A. Hadipour, B. de Boer, and Paul W. M. Blom, J. Appl. Phys., 102, 074506 (2007).

[2.59] H. Sirringhaus, P. J. Brown, R. H. Friend, M. M. Nielsen, K. Bechaard, B. M. W. Langeveld-Voss, A. J. H. Spiering, R. A. J. Janssen, E. W. Meijer, P. Herwig, and D. M. de Leeuw, Nature, 401, 685, 1999.

[2.60] A. Ullmann, J. Ficker, W. Fix, H. Rost, McCulloch, I., M. Giles, G.E. ed. Jabbour, and N.S. Sariciftci. Mater. Res. Soc. Symposium Proc., 665 (2002).

[2.61] V. D. Mihailetchi, J. K. J. van Duren, P. W. M. Blom, J. C. Hummelen, R. A. J. Janssen, J. M. Kroon, M. T. Rispens, W. J. H. Verhees, and M. M. Wienk. Adv. Funct. Mater., 13, 43 (2003).

[2.62] P. H. Nguyen, S. Scheinert, S. Berleb, W. Bruttin and G. Paasch, Organic Electronics, 2, 105 (2001).

Chapter 3
Short circuit current density in bulk HJ OSCs

In the previous chapter, the working principles and the different structure designs of OSCs have been introduced. It has been indicated that the bulk HJ solar cell is the most promising cell because it has the potential to guarantee the effective exciton dissociation and at the same time guarantee the efficient carrier transport by optimizing the active layer morphology. Many studies have been done on this structure [3.1-3.5]. In order to achieve the good device performance, a high J_{SC} is essential. Thus to well understand and predict J_{SC} becomes important because it can help us to figure out the limiting factors for J_{SC} and propose the ways to increase the device performance. In this chapter, a model describing J_{SC} in bulk HJ solar cells is proposed. Based on the model, the limiting factors of J_{SC} are investigated.

3.1 Factors describing J_{SC}

J_{SC} is directly related to the absorption ability of organic materials. It is believed that increasing the light harvesting ability of the active layer is an effective method to increase J_{SC}. In order to increase J_{SC}, some optical models [3.6-3.8] have been built to optimize the active layer thickness. However, only optimizing the thickness for better light absorption is difficult to improve J_{SC}. This is because that PCE depends on not only the light absorption, but also on exciton dissociation and charge collection. In bulk HJ OSCs, a blend layer consisting of conjugated polymer as the electron donor and fullerene

as the electron acceptor is always used as the active layer. For a well blended layer, the length scale of D and A phases is smaller than the exciton diffusion length (typically less than 10 nm), so that most of the generated excitons can diffuse to the D/A interface before they decay. Even if all the excitons can reach the D/A interface, not all of them can be dissociated into free carriers. This is because the dissociation probability is less than 1 at D/A interface. The dissociation probability is not a constant and depends on some factors such as electric field and temperature [3.2]. When the active layer thickness is increased to optimize the light absorption, the electric field in the blend layer decreases, which lowers down the exciton dissociation probability [3.2] and makes charge collection less effective [3.8] simultaneously. As a result, J_{SC} may become low, although the thickness has been optimized for better light absorption. Thus to obtain a higher J_{SC}, both the optical and the electric properties should be considered at the same time.

In previous works, *Lacic* et al. [3.9] and *Monestier* et al. [3.10] studied the characteristic of J_{SC}. However, they neglected the influence of exciton dissociation probability, which is very important for OSCs [3.11]. In another study, *Koster* et al. [3.12] considered this factor, but they neglected the optical interference effect in OSCs, which is a basic property for the very thin organic film. All the above studies are based on the numerical method, and then it is not easy to solve the equations and understand the direct influence of various parameters on the J_{SC}. A more direct model is needed.

In this chapter, a model predicting J_{SC} is proposed based on very simple analytical equations. From this model, it is found that optical interference effect has a very important influence on J_{SC}. Besides, the carrier lifetime is also found to be an important factor. Generally, when the lifetimes of both electrons and holes are long enough, the

dissociation probability plays a very important role for a thick active layer. J_{SC} behaves wavelike with the variation of the active layer thickness. When the lifetime of one type of carrier is too short, the accumulation of charges appears near the electrode and J_{SC} increases at the initial stage and then decreases rapidly with the increase of the active layer thickness. The validity is confirmed by the experiment results.

3.2 Theory

3.2.1 Exciton generation

The active layer in OSCs absorbs the light energy when it is propagating through this layer. How much energy can be absorbed depends on the complex index of refraction $\bar{n} = n + i\kappa$ of the materials. At the position z in the organic film (Fig. 3.1 (a)), the time average of the energy dissipated per second for a given wavelength λ of incident light can be calculated by [3.7]

$$Q(z,\lambda) = \frac{1}{2} c\varepsilon_0 \alpha_j n \left|\bar{E}(z)\right|^2 \tag{3.1}$$

where c is the vacuum speed of light, ε_0 the permittivity of vacuum, n the real index of refraction, α the absorption coefficient, $\alpha = \frac{4\pi\kappa}{\lambda}$, and E(z) the electrical optical field at point z. $Q(z,\lambda)$ have the unit of W/m^3 . Assuming that every photon generates one exciton, the exciton generation rate at position z in the material is given by

$$G(z,\lambda) = \frac{Q(z,\lambda)}{h\gamma} = \frac{\lambda}{hc} Q(z,\lambda) \tag{3.2}$$

where h is Planck constant, and γ is the frequency of incident light. The total excitons generated by the material at position z in solar spectrum are calculated by

$$G(z) = \int_{300}^{800} G(z,\lambda) d\lambda \tag{3.3}$$

Here the integration is performed from 300 nm to 800 nm, which is because that beyond this range, only very weak light can be absorbed by P3HT: PCBM active layer. In ISCs [3.13], $Q(z,\lambda)$ is usually modeled by

$$Q(z,\lambda) = \alpha I_0 e^{-\alpha z} \tag{3.4}$$

I_0 is the incident light intensity. Here, the optical interference effect of the materials is neglected. But in OSCs, the active layers are so thin compared to the wavelength that the optical interference effect cannot be neglected which will be discussed in the next section.

3.2.2 Optical model

In order to obtain the distribution of electromagnetic field in a multilayer structure, the optical transfer-matrix theory (TMF) is one of the most elegant methods, which was introduced by *Heavens* [3.14] and was firstly applied in OSCs by *Pettersson* [3.6]. In this method, the light is treated as a propagating plane wave, which is transmitted and reflected on the interface. As shown in Fig. 3.1 (a), OSCs usually consist of a stack of several layers. Each layer is treated to be smooth, homogenous and described by the same complex index of refraction $\bar{n} = n + i\kappa$. The optical electric field at any position in the stack can be decomposed into two parts: an upstream component E^+ and a downstream component E^-, as shown in Fig. 3.1 (a). According to Fresnel theory, the complex

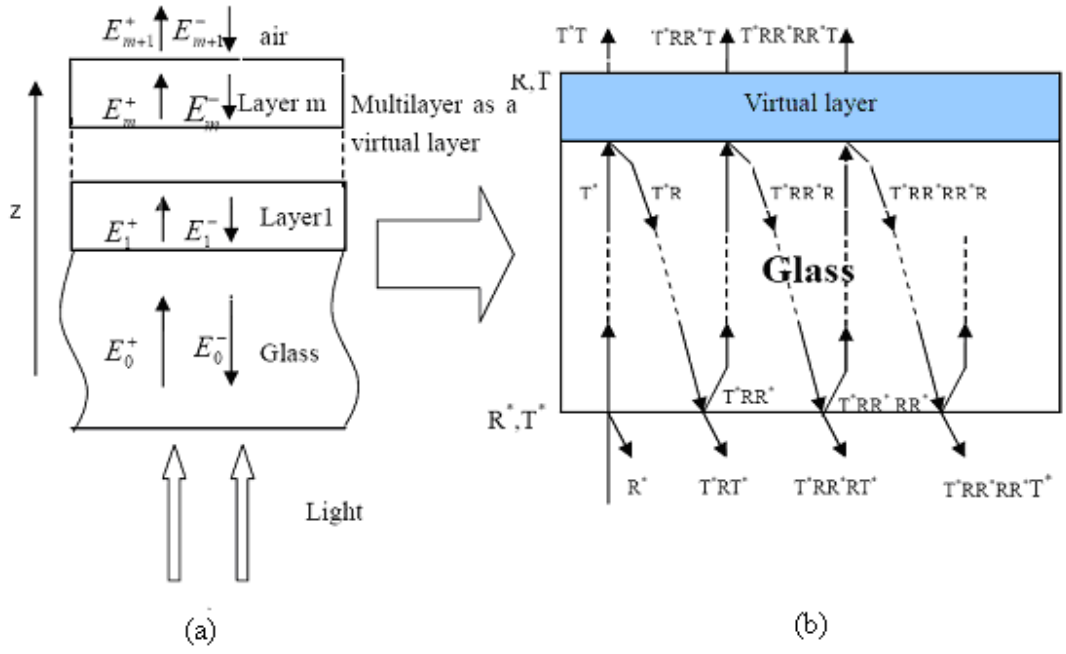

Fig. 3.1 Bulk HJ OSCs consist of multilayer structure between air and a semi-infinite substrate. The light is incident on the cells from the downside. (a) the optical electric field in each layer can be denoted as an upstream optical electric field E^+ and a downstream optical electric field E^-, and (b) treating the multilayer as a virtual layer to calculate the light loss due to the very thick glass substrate.

reflection and transmission coefficients for a propagating plane wave along the surface normal between two adjacent layers i and j are

$$r_{jk} = \frac{\overline{n_j} - \overline{n_k}}{\overline{n_j} + \overline{n_k}} \tag{3.5a}$$

$$t_{jk} = \frac{2\overline{n_j}}{\overline{n_j} + \overline{n_k}} \tag{3.5b}$$

where r_{jk} and t_{jk} are the reflection coefficient and the transmission coefficient, $\overline{n_j}$ and $\overline{n_k}$ the complex index of refraction for layer j and layer k. So the interface matrix between the two adjacent layers is simply described as

$$I_{jk} = \frac{1}{t_{jk}}\begin{bmatrix} 1 & r_{jk} \\ r_{jk} & 1 \end{bmatrix} = \begin{bmatrix} \dfrac{\overline{n_j} + \overline{n_k}}{2\overline{n_j}} & \dfrac{\overline{n_j} - \overline{n_k}}{2\overline{n_j}} \\ \dfrac{\overline{n_j} - \overline{n_k}}{2\overline{n_j}} & \dfrac{\overline{n_j} + \overline{n_k}}{2\overline{n_j}} \end{bmatrix} \tag{3.6}$$

When light travels in layer j with the thickness d, the phase change can be described by the layer matrix (phase matrix)

$$L_j = \begin{bmatrix} e^{-i\beta_j} & 0 \\ 0 & e^{i\beta_j} \end{bmatrix} \tag{3.7}$$

where $\beta_j = \dfrac{2\pi\overline{n_j}d_j}{\lambda}$ is phase change the wave experiences as it traverses in layer j. The optical electric fields in the substrate (subscript 0) and the final layer (subscript m+1) have the relationship as

$$\begin{bmatrix} \overline{E_0^+} \\ \overline{E_0^-} \end{bmatrix} = S\begin{bmatrix} \overline{E_{m+1}^+} \\ \overline{E_{m+1}^-} \end{bmatrix} = \begin{bmatrix} S_{11} & S_{12} \\ S_{12} & S_{22} \end{bmatrix}\begin{bmatrix} \overline{E_{m+1}^+} \\ \overline{E_{m+1}^-} \end{bmatrix} = \left(\prod_{v=1}^{m} I_{(v-1)v}L_v\right) \bullet I_{m(m+1)} \tag{3.8}$$

Because in the final layer, $\overline{E_{m+1}^-}$ is 0, it can be derived that the complex reflection and transmission coefficients for the whole multilayer are:

$$r = \frac{\overline{E_0^-}}{\overline{E_0^+}} = \frac{S_{21}}{S_{11}} \tag{3.9a}$$

$$t = \frac{\overline{E_{m+1}^{+}}}{\overline{E_0^{+}}} = \frac{1}{S_{11}} \tag{3.9b}$$

In order to get the optical electric field $E_j(z)$ in layer j, S is divided into two parts,

$$S = S_j^{'} L_j S_j^{''} \tag{3.10}$$

where

$$S_j^{'} = \left(\prod_{v=1}^{j-1} I_{(v-1)v} L_v \right) \bullet I_{j(j-1)} \tag{3.11a}$$

and

$$S_j^{''} = \left(\prod_{v=j+1}^{m} I_{(v-1)v} L_v \right) \bullet I_{m(m+1)} \tag{3.11b}$$

At the down interface in layer j, the upstream optical electric field is denoted as

$$\overline{E_j^{+}} = t_j^{+} \bullet \overline{E_0^{+}} = \frac{S_{j11}^{''}}{S_{j11}^{'} S_{j11}^{''} + S_{j12}^{'} S_{j21}^{''} e^{i2\beta_j}} \overline{E_0^{+}} \tag{3.12}$$

Similarly, at the up interface in layer j, the downstream optical electric field is

$$\overline{E_j^{-}} = t_j^{-} \bullet \overline{E_0^{+}} = \frac{S_{j21}^{''}}{S_{j11}^{''}} e^{i2\beta_j} \overline{E_j^{+}} \tag{3.13}$$

The optical electric field $\overline{E_j}(z)$ at any position z in layer j is the sum of upstream part $\overline{E_j^{+}}(z)$ and downstream part $\overline{E_j^{-}}(z)$

$$\overline{E_j}(z) = \overline{E_j^+}(z) + \overline{E_j^-}(z) = (t_j^+ e^{i\beta_j} + t_j^- e^{-i\beta_j})\overline{E_0^+} \tag{3.14}$$

3.2.3 Light loss due to the substrate

Because the glass substrate is very thick compared to wavelength (usually 1mm>>wavelength), the optical interference effect in the substrate can be neglected. Here only the correction of the light intensity at the air/substrate and substrate /multilayer interfaces is made. As shown in Fig. 3.1 (b), the multilayer can be treated as a virtual layer whose complex reflection and transmission coefficients can be calculated using above equations. Then the irradiance to the multilayer is

$$I_g = T\left(\sum_{i=0}^{\infty}(R^*R)^i\right)I_0 = \frac{1-R^*}{1-RR^*}I_0 \tag{3.15}$$

I_g is described as

$$I_g = \frac{1}{2}c\varepsilon_0 n_g \left|E_0^+\right|^2 \tag{3.16}$$

It can be derived that

$$\left|E_0^+\right| = \sqrt{\frac{2(1-R^*)*I_0}{\varepsilon_0 c n_g (1-RR^*)}} \tag{3.17}$$

3.2.4 Free carrier generation

When the excitons are generated, not all of them can be dissociated into free carriers. The dissociation probability depends on the electric field and temperature.

Recently, the dissociation probability has been taken into consideration in OSCs [3.2, 3.12]. The geminate recombination theory, first introduced by *Onsager* and refined by *Brau* later, gives the probability of electron-hole pair dissociation,

$$P(F,T) = \frac{k_D(F)}{k_D(F) + k_X} \tag{3.18}$$

where T is the temperature, F the electric field, k_X the decay rate to the ground state and k_D the dissociation rate of a bound pair. Braun gives the simplified form for dissociation rate

$$k_D(F) = k_R e^{-U_B/k_B T}\left[1 + b + \frac{b^2}{3} + \cdots\right] \tag{3.19}$$

where a is the initial separation distance of a given electron-hole pair, U_B is electron-hole pair binding energy described as

$$U_B = \frac{q^2}{4\pi\varepsilon_0\varepsilon_r a} \tag{3.19a}$$

and

$$b = \frac{q^3 F}{8\pi\varepsilon_0\varepsilon_r k_B T^2} \tag{3.19b}$$

ε_r is the dielectric constant of the material. In equation (3.19), k_R is a function of the carrier recombination. For simplification, we treat k_R as a constant. Thus, the dissociation probability P only depends on the electric field F when the temperature keeps constant.

3.2.5 J_{SC} expression equations

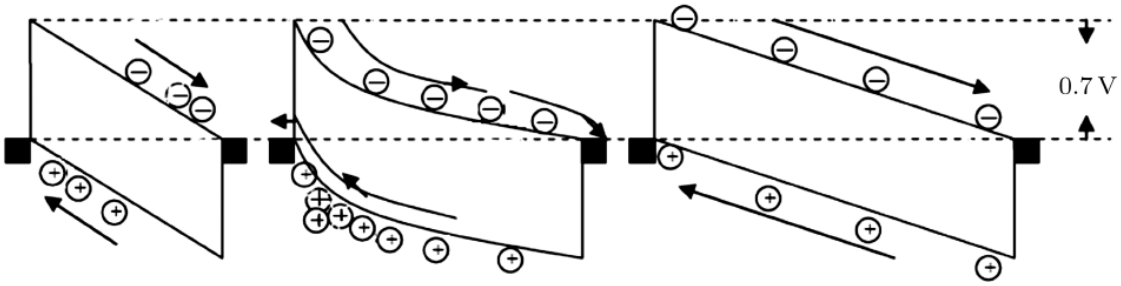

(a) (b) (c)

Fig. 3.2 Energy band diagrams of an OSC under short circuit condition. The built-in voltage is 0.7 V determined by the electrodes. (a) Case I: the active layer thickness is shorter than both hole and electron drift lengths, (b) Case II: the active layer thickness is longer than hole drift length but shorter than electron drift length, and (c) Case III: the active layer thickness is longer than both hole and electron drift lengths.

J_{SC} is determined by the number of carriers collected by the electrodes in the period of their lifetime τ under short circuit condition. If the active layer thickness L is shorter than the electron and hole drift lengths (which is the product of carrier mobility μ, the electric field F and the carrier lifetime τ) or in other word, the lifetimes of both types of carriers exceed their transit time (case I as in Fig 3.2 (a)), all generated free carriers can be collected by the electrodes. Considering the dissociation probability P, J_{SC} is

$$J_{SC} = qP(F,T)GL \tag{3.20}$$

where G is the average exciton generation rate in the active layer.

If L is longer than drift lengths of electrons and holes, that is to say that the lifetimes of both types of carriers are smaller than their transit time, the carriers are accumulated in the active layer. At steady state, J_{SC} follows Ohm's law [3.15]. Considering the dissociation probability P, J_{SC} is

$$J_{SC} = qP(F,T)G(\mu_e\tau_e + \mu_h\tau_h)F = qP(F,T)G(\mu_e\tau_e + \mu_h\tau_h)V_{bi}/L \qquad (3.21)$$

where V_{bi} is the built-in potential which is usually determined by the difference between cathode and anode work functions. This is case III as described in Fig. 3.2 (c).

Between case I and case III, it is case II as described in Fig. 3.2 (b). In this case, L is only longer than the drift length of one type of carrier. For P3HT:PCBM based OSCs, the mobilities of holes and electrons in P3HT:PCBM (1:1 by weight) layer are $2\times10^{-8}m^2V^{-1}s^{-1}$ and $3\times10^{-7}m^2V^{-1}s^{-1}$, respectively [3.16]. Because the hole mobility is one order lower than the electron mobility, holes are easy to accumulate in the active layer, which makes the electric field non-uniform. In order to enhance the extraction of holes, the electric field increases near the anode. On the other hand, in order to diminish the extraction of electrons, the electric field decreases near the cathode. The electric field is modified until the extraction of holes equal to the extraction of electrons. *Goodman* and *Rose* studied this case and gave an equation for the photocurrent [3.17]. Considering the dissociation probability P, J_{SC} is

$$J_{sc} = qP(F,T)GL(1+c)\frac{-c+(c^2+4(1-c)V\mu_h\tau_h/L^2)^{\frac{1}{2}}}{2(1-c)} \qquad (3.22)$$

where $c = \frac{\mu_h \tau_h}{\mu_e \tau_e}$ is the drift length ratio of holes and electrons. When c<<1, the equation is simplified to

$$J_{sc} = qP(F,T)G(\mu_h \tau_h)^{1/2} V^{1/2} \tag{3.23}$$

3.3 Results and discussion

3.3.1 Exciton generation profile in the active layer

For the studied bulk HJ cell, the D and A materials are well blended and form the active layer. Because the D and A domains are very small, we can neglect the complex reflection and transmission at D/A interfaces, and treat the whole active layer as one homogenous material. This method has been widely used to measure the optical constant of the blended active layer, which well describes the optical properties of this blend layer [3.10, 3.18]. All the optical constants (n, k) of the ITO, PEDOT:PSS, P3HT:PCBM active layers and the Al electrode [3.10, 3.18] are input into our program, and the exciton generation rate in OSCs is calculated.

If the interference effect is neglected, the exciton generation rate decreases with the increasing thickness of the active layer as described in equation (3.4) which makes the corresponding average exciton generation rate (total exciton generation rate divided by the thickness) become smaller. However, when the optical interference effect is considered, the modulation effect of average exciton generation rate with the thickness variation is very clear as shown in Fig. 3.3. At the initial stage, the average exciton generation rate increases with the increasing thickness of the active layer. This is because the first light peak does not appear in the active layer when the active layer is thin due to

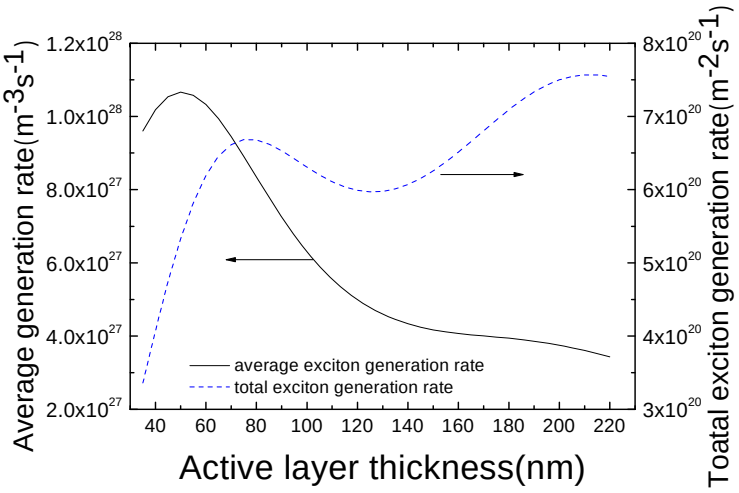

Fig. 3.3 The calculated exciton generation rate in the active layer when the optical interference effect is considered.

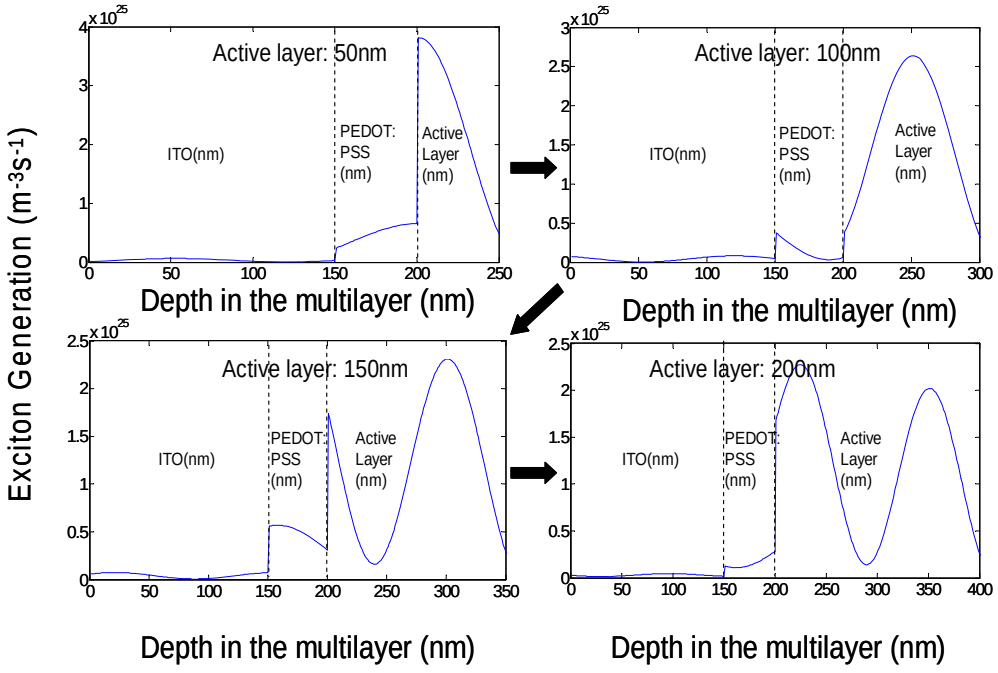

Fig. 3.4 Evolution of exciton generation in the active layer. The light wavelength is 500 nm. It can be seen that with the increase of the active layer thickness, the first peak enters the active layer, which makes the average exciton generation rate become large. For very thick film, although other peaks can enter the active layer, the absolute values for the peaks become small, which leads to the corresponding decrease of average exciton generation rate.

the interference effect. With the increase of the active layer, the first light peak approaches and enters the active layer such that the average generation rate becomes larger. With the further increase of the active layer, the average generation rate decreases although other light peaks enter the active layer. This is because for a thicker film, the thickness of the active layer dominates the generation rate. This evolution of exciton generation is plotted in Fig. 3.4 for the 500 nm light wavelength.

3.3.2 J_{SC} and the active layer thickness

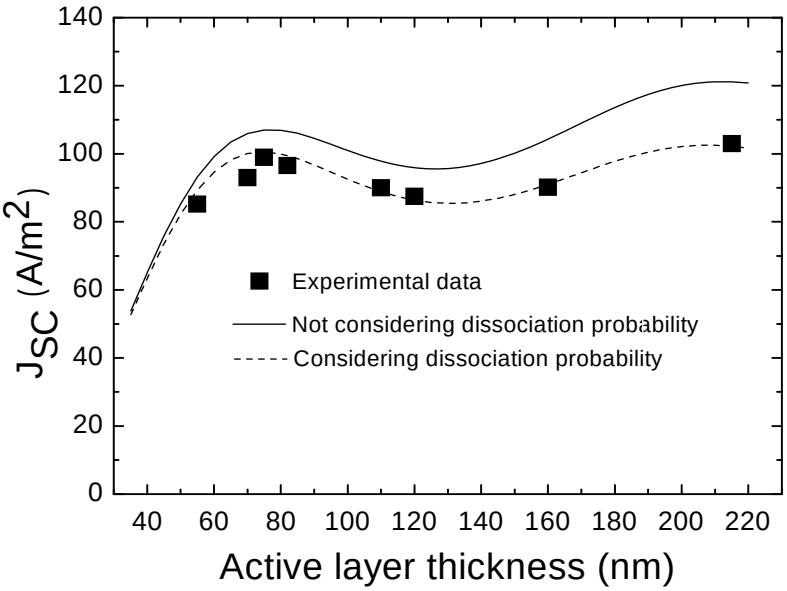

Fig. 3.5 Long carrier lifetime condition: the lifetimes of both carriers are always longer than their transient time. J_{SC} is predicted with and without considering the dissociation probability, and experimental data are extracted from [3.10].

Based on the calculated exciton generation rate, it is easy to predict J_{SC} when the drift lengths of both carriers are larger than the blend layer thickness. If all the generated

excitons can be dissociated into free carriers, and then collected by the electrodes, J_{SC} should be proportional to the total exciton generation rate and behave wavelike as shown in Fig. 3.5 (solid line). *Monestier* et al. [3.10] have found this trend based on P3HT:PCBM systems. In their experiments, the active layer thickness is varied from a few tens nanometer to 215 nm. When the thickness is 70 nm, J_{SC} reaches the maximum value, and followed by a little decrease until 140 nm. When the thickness increases further, J_{SC} increases again. Unfortunately, there is obvious deviation between the prediction and the experiment results, especially in the thick film as shown in Fig. 3.5 (a) (solid line). Obviously, the assumption that the dissociation probability is unity is not correct. The influence of dissociation probability on J_{SC} must be considered.

In the previous work, *Mihailetchi* [3.16] exactly predicted photocurrent of P3HT:PCBM solar cells by assuming the same e-h separation distance (a) and decay rate (k_X). By fitting the experimental data, they obtained e-h separation distance of a=1.8nm, room temperature bound pair decay rate of $k_X \approx 2\times10^4 s^{-1}$ for a 120 nm active layer, and the dissociation probability is close to 90%. We use the same data and derive the parameter $k_R = 3.9662\times10^8 S^{-1}$ (equation (3.19)). The dissociation probability is calculated according to section 3.2.4. The results are shown in Fig. 3.6. Obviously, the exciton dissociation probability becomes lower with the increase of the active layer thickness. Using the results to correct J_{SC}, another J_{SC} curve is obtained and also shown in Fig. 3.5 (dash line). It can be seen that the predicted J_{SC} is exactly in accordance with the experimental results. This confirms the validity of our model. In the previous work, *Monestier* [3.10] modeled J_{SC}, and found that the predicted J_{SC} is larger than the experimental data, especially for the thickness larger than 180 nm. They attributed this to

the thickness dependence of optical constants. Here, according to our model, it is found that the deviation should come from the low exciton dissociation probability for thick active layers.

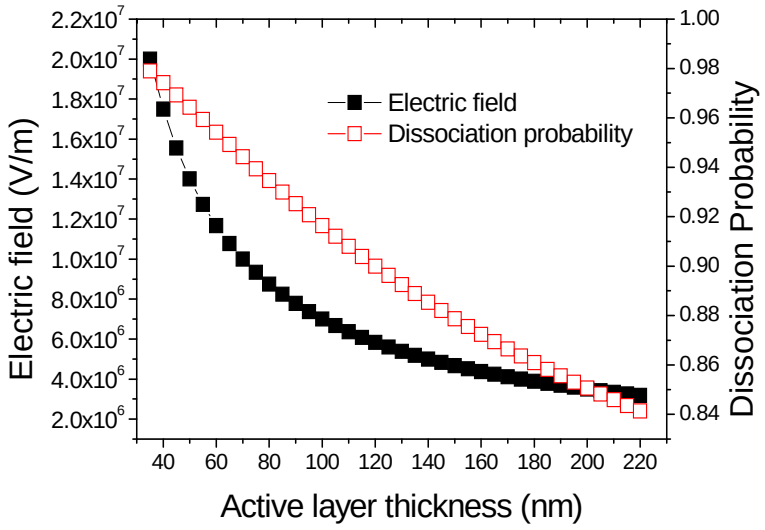

Fig. 3.6 Relations of electric field and exciton dissociation probability with the active layer thickness.

We have predicted J_{SC} precisely for the long enough carrier lifetime case. However, for OSCs, the performance is sensitive to the process and experimental conditions. This may make the carrier lifetime relatively short. For P3HT:PCBM system, because the hole mobility is one order of magnitude lower than the electron mobility, holes are easy to accumulate in the active layer and limit the photocurrent. This is the case II as described in section 3.2.5. By tuning the parameters to fit the experimental data [3.19], the best fitting curve is obtained (Fig. 3.7) when the average hole lifetime τ is $6.2\times10^{-7}\,s$ and dissociation probability is unity. A short lifetime τ may imply that there are many

defects. These defects increase the exciton dissociation probability [3.20]. At the same time, the transport process becomes the dominant limiting factor for J_{SC}, and the exciton dissociation process becomes relatively unimportant. Then it seems that the assumption of exciton dissociation probability as unity can satisfy the need of the prediction. In Fig. 3.7, we can see that there are two regions in the fitting curve. The left region is determined by equation (3.20). In this region, the lifetimes of both carriers are longer than their transient time. The solid line in the right region is determined by equation (3.22). In this region, hole lifetime is shorter than its transit time and electron lifetime is longer than its transit time.

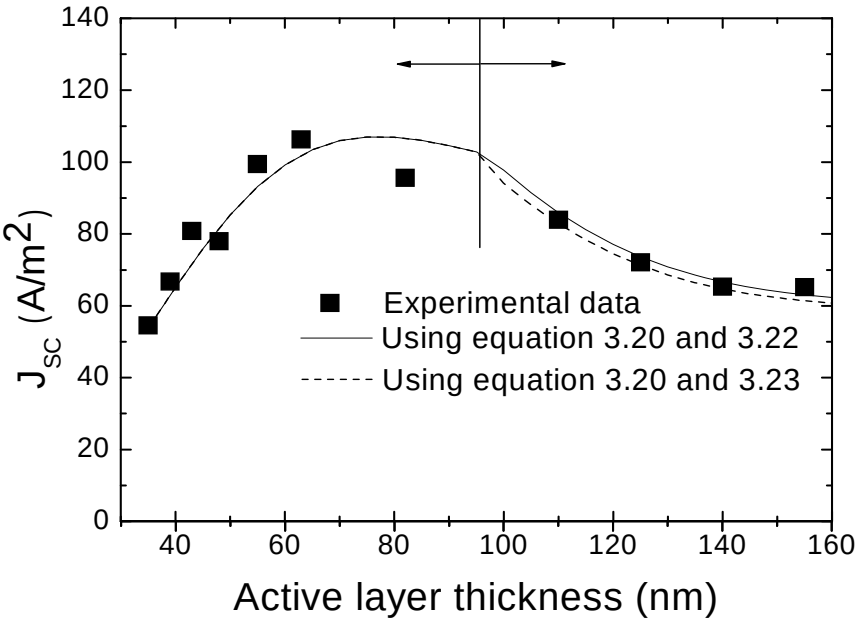

Fig. 3.7 Short hole carrier lifetime condition. Left arrow: hole lifetime is longer than its transient time; right arrow: hole lifetime is shorter than its transient time, and hole lifetime is $6.2\times10^{-7}s$, and electron lifetime is $1\times10^{-6}s$. Experimental data are extracted from [3.19].

If it is assumed that the drift length ratio of hole and electron ($c = \frac{\mu_h \tau_h}{\mu_e \tau_e}$) is very small, then the equation (3.23) can be used to predict J_{SC}. As shown in Fig. 3.7 (dash line), it can predict J_{SC} very well, which means c<<1.

3.4 Summary

In this chapter, the exciton generation rate was calculated by taking the optical interference effect into account. Based on the calculated exciton generation rate, the dependence of J_{SC} on the active layer thickness was analyzed and compared with experimental data. Because of the optical interference effect, the total exciton generation rate does not monotonously increase with the increase of the active layer thickness, but behaves wavelike which induces the corresponding variation of J_{SC}. The carrier lifetimes also influence J_{SC} greatly. When the lifetimes of both electrons and holes are long enough, dissociation probability plays an important role for the thick active layer. J_{SC} behaves wavelike with the variation of the active layer thickness. When the hole lifetime is too short (drift length is smaller than device thickness), accumulation of charges appears near the electrode and J_{SC} increases at the initial stage and then decreases rapidly with the increase of the active layer thickness. The accordance between the predictions and the experimental results confirms the validity of the proposed model. These results give a guideline to optimize J_{SC}.

References

[3.1] C. J. Brabec, N. S. Sariciftci and J. C. Hummemen, Adv. Funct. Mater., 11, 15 (2001).

[3.2] V. D. Mihailetchi, L. J. A. Koster, J. C. Hummenmen, and P. W. M. Blom, Phys. Rev. Lett., 93, 216601 (2004).

[3.3] C. F. Zhang, S. W. Tong, C. Y. Jiang, E. T. Kang, D. S. H. Chan and C. X. Zhu, Appl. Phys. Lett., 92, 083310 (2008).

[3.4] J. Y. Kim, K. Lee, N. E. Coates, D. Moses, T. Q. Nguyen, M. Dante and A. J. Heeger, Science, 317, 222 (2007).

[3.5] H. Hoppe and N. S. Sariciftci, J. Mater. Chem., 16, 45 (2006).

[3.6] L. A. A. Pettersson, L. S. Roman, and O. Inganas, J. Appl. Phys., 86, 487 (1999).

[3.7] P. Peumans, A. Yakimov and S. R. Forrest, J. Appl. Phys., 93, 3693 (2003).

[3.8] N. K. Persson, H. Arwin and O. Inganas, J. Appl. Phys., 97, 34503 (2005).

[3.9] S. Lacic, O. Inganas, J. Appl. Phys., 97, 124901 (2005).

[3.10] F. Monestier, J. J. Simon, P. Torchio, L. Escoubas, F. Flory, S. Bailly, R. Bettignies, S. Guillerez and C. Defranoux, Sol. Energy Mater. Sol. Cells, 91, 405 (2007).

[3.11] V. D. Mihailetchi, L. J. A. Koster, J. C. Hummelen, and P. W. M. Blom, Phys. Rev. Lett., 93, 216601 (2004).

[3.12] L. J. A. Koster, E. C. P. Smits, V. D. Mihailetchi, and P. W. M. Blom, Phys. Rev. B, 72, 085205 (2005).

[3.13] A. K. Ghosh and T. Feng, J. Appl. Phys., 49, 5982 (1978).

[3.14] O. S. Heavens, Optical Properties of Thin solid Films (Dover, New York, 1965)

[3.15] K. C. Kao and N. W. Hwang, Electrical transport in solids: with particular reference to organic semiconductors, Oxford; New York: Pergamon Press vol. 14 (1981).

[3.16] V. D. Mihailetchi, H. Xie, B. Boer，L. J. A. Koster and P. W. M. Blom, Adv. Funct. Mater., 16, 699 (2006).

[3.17] A. M. Goodman and A. Rose, J. Appl. Phys., 42, 2823 (1971).

[3.18] H. Hoppe, N. S. Sariciftci and D. Meissner, Mol. Cryst. Liq. Cryst., 385, 233 (2002).

[3.19] G. Li, V. Shrotriya and Y. Yao, J. Appl. Phys., 98, 43704 (2005).

[3.20] B. A. Gregg, MRS bulletin, 30, 20 (2005).

Chapter 4
Open circuit voltage
in layered and bulk HJ OSCs

Due to great efforts devoted to OSCs, their performance has been steadily improved in the past years [4.1-4.7]. A better understanding of the device physics behind OSCs thus becomes important to further improve the device performance [4.1-4.13]. In Chapter 3, the parameter J_{SC} is investigated theoretically. As has been discussed, J_{SC} is directly related to the light harvesting capability of organic materials. Due to the large E_{go} of organic materials (usually around 2 eV), there is a large spectral mismatch between the sunlight and absorption spectrum of organic materials [4.6, 4.7, 4.14, 4.15], which makes J_{SC} much lower than those reported for inorganic devices. Many studies have been carried out to improve the device light harvesting capability, such as using small bandgap materials and combining different organic materials with complementary absorption spectra in one device [4.14-4.16]. J_{SC} also depends on the active layer thickness. But simply increasing the active layer thickness may not be enough to increase the light absorption ability because of the optical interference effect in the very thin active layer [4.17-4.18]. Devices should be fabricated around the optical interference peaks. Besides, a proper D and A blended morphology must be guaranteed to ensure the efficient exciton dissociation and charge transport. The film morphology is related to the solvent type, or deposition method [4.19-4.20]. In addition to J_{SC}, the performance of OSCs is also related to V_{OC}, given that $\eta=J_{SC}V_{OC}FF/P_{in}$. In order to improve the device performance further,

another issue of considerable focus in OSCs is V_{OC}, which will be discussed in this chapter.

4.1 V_{OC} in OSCs

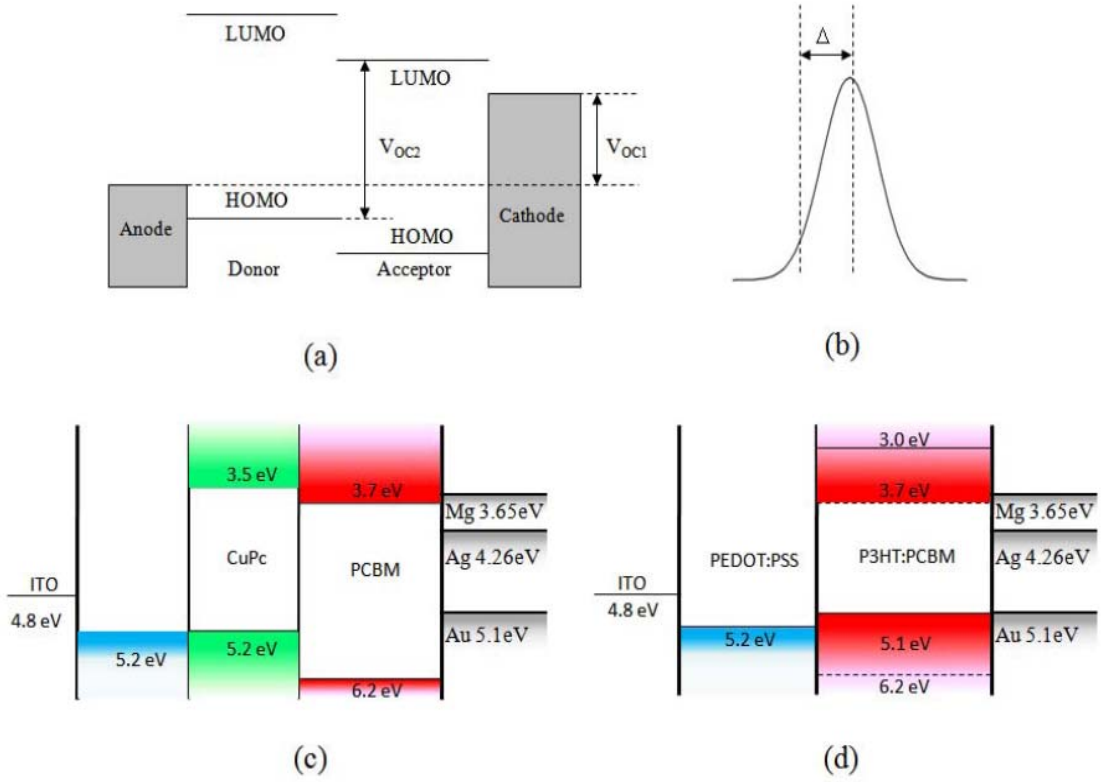

Fig. 4.1 (a) Schematic representation of the origin of V_{OC} of organic PV cells. V_{OC1} represents the difference of anode and cathode work function. V_{OC2} represents the difference of HOMO of donor and LUMO of acceptor. (b) Gaussian Density of States (DOS) for organic materials. Δ represents that the transport level in a Gaussian DOS lays below its center by $\frac{5}{9}\frac{\sigma^2}{k_B T}$. (c) and (d) show the energy diagrams of materials and device structures used in layered and HJ PV cells.

V_{OC} has attracted much research interest in recent years [4.21-4.27]. It has been shown that V_{OC} does not follow the traditional MIM model [V_{OC1} in Fig. 4.1 (a)], but has a direct relationship with the offset energy between the HOMO of D and the LUMO of A [V_{OC2} in Fig. 4.1 (a)] in both the layered and bulk HJ PV cells. A recent study including a total of 26 different polymer/fullerene blend devices showed that V_{OC} varies linearly with HOMO of the polymer [4.24]. Then the enhancement of V_{OC} can be obtained by using new materials with larger offset energies at organic heterointerfaces. However, to enhance V_{OC} by increasing the offset energy usually decreases J_{SC}, because a high bandgap absorber is required and thus leads to a large mismatch with the solar spectrum. Therefore, it is more attractive to increase V_{OC} of the PV cells made on the given organic materials. This makes it necessary to better understand the factors affecting V_{OC} beyond the D and A offset energies, for example, the influence of the electrodes. It has been observed that in layered devices, V_{OC} shows a very weak dependence on the electrode work function difference. Only a small variation in V_{OC} was observed when varying the work function of cathode [4.13, 4.26]. However, an obvious dependence of V_{OC} on the electrodes was reported in bulk HJ PV cells [4.22, 4.23]. For example, a total of more than 500 mV variation of V_{OC} was observed by varying the cathode work function [4.23].

Since both the layered and bulk HJ PV cells are based on organic materials and have the same operation mechanisms (light absorption, exciton production, exciton dissociation and charge transport), their V_{OC} should also follow the same mechanism. However, V_{OC} of the two types of PV cells show different dependences on the metal electrodes. It is of great importance to understand the mechanism behind the different

dependences for the PV cells, because it gives us a guideline to enhance V_{OC} by the electrode modification and thus improve the device performance further.

The aim of this chapter is to investigate the factors which determine V_{OC} of organic HJ PV cells. Based on the experimental results and theoretical analysis, an explanation for the different dependences of V_{OC} on the metal electrodes in layered and bulk HJ PV cells is proposed. It is found that although V_{OC} of both the two types of PV cells are determined by the electrodes and the light injected carriers at the D/A interface, the distinct device structures make the boundary conditions in layered and bulk HJ PV cells very different, which leads to the different dependences of V_{OC} on the electrodes.

4.2 Experimental

The typical organic PV cells studied in this work consist of the active layer sandwiched between a transparent anode and a metal cathode. Briefly, the devices were fabricated on indium-tin-oxide (ITO)-coated glass substrates. After routine solvent cleaning (treated sequentially with detergent, de-ionized water, acetone, and isopropanol in an ultrasonic bath for about 15 mins), the dried ITO glass substrates were treated with oxygen plasma for about 3 mins. Then the filtered PEDOT:PSS suspension (through 0.45 μm filter) was spin coated on the top of the ITO surface to form a ~50 nm layer under ambient condition, before drying the substrates at 120^{o}C in an oven for more than 1 hour. For layered HJ PV cells, a ~20 nm CuPc layer was deposited by thermal evaporation under a pressure of about 5.4×10^{-5} Pa, and then followed by spin coating ~40 nm PCBM to finish the active layer. For bulk HJ PV cells, P3HT:PCBM with different weight ratios were dissolved in dichlorobenzene and stirred in the glove box before spin casting to form a ~100 nm blend layer. Finally the metal electrode was deposited through

a shadow mask. The device current-voltage (I-V) characteristics were measured as fabricated by using a Keithley 2400 parameter analyzer under a simulated light intensity (AM 1.5G) with various light intensities. The light intensity was calibrated by a Thorlabs optical power meter. All the parameters of the used materials and the device structures are shown in Figs. 4.1 (c) and (d). To understand the influence of metal electrodes on V_{OC}, different metal electrodes (Mg, Ag and Au) were employed to fabricate both the organic layered and bulk HJ PV devices.

4.3 Experimental results

Fig. 4.2 shows the typical I-V characteristics of the layered devices with the structure configuration of ITO/PEDOT:PSS/CuPc/PCBM/cathode (cathode=Ag, Au, and Mg). The devices with Ag, Mg and Au cathodes exhibit V_{OC} values of 605 mV, 608 mV and 589 mV, respectively. The fact that V_{OC} of the device with Au cathode is only slightly lower than those with Mg and Ag cathodes suggests a severely deviation from the prediction of the classic MIM model where V_{OC} is limited by the difference of the anode and cathode work functions [V_{OC1} in Fig. 4.1 (a)]. According to the MIM model, a large variation of V_{OC} should be observed for different cathodes with metal work function difference larger than 1 eV. However, here only a small variation of less than 20 mV was observed. *Rand* et al. [4.13] and *Cheyns* et al. [4.26] also reported that only a small variation in V_{OC} was observed when varying the cathode metals, which confirms our experimental results that the electrodes have a weak influence on V_{OC} in the layered PV cells.

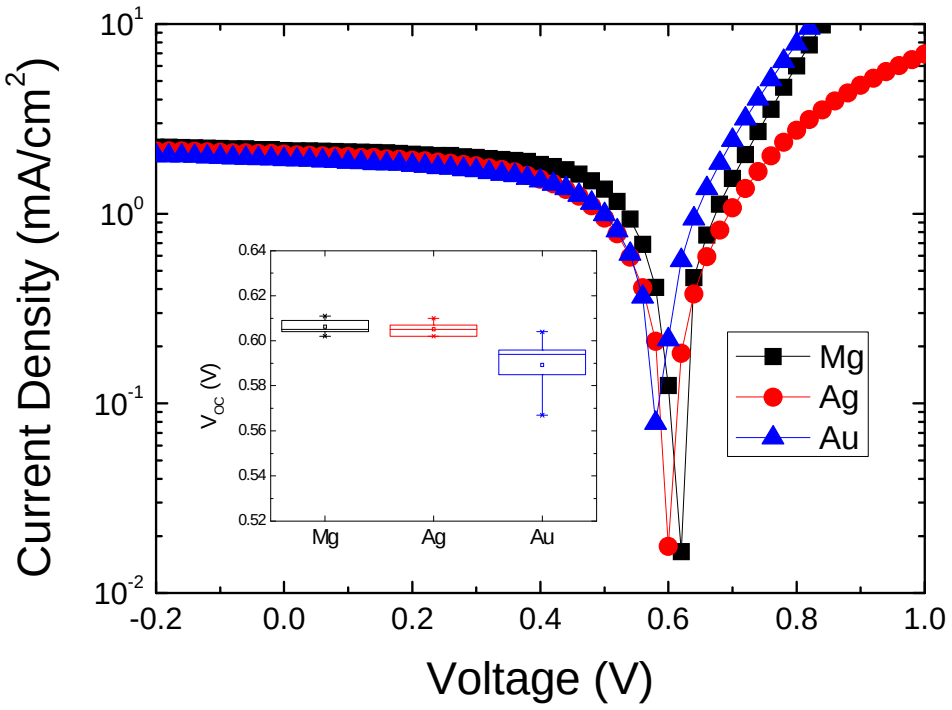

Fig. 4.2 Characteristics of the layered HJ PV cells with different metal electrodes. Inset: statistical properties of V_{OC}. The trend is clear that V_{OC} of the layered HJ PV cells with high work function metal is smaller than V_{OC} of the devices with low work function metal. The light intensity is 100 mW/cm^2.

Fig. 4.3 shows the typical I-V characteristics of the bulk HJ PV cells based on P3HT:PCBM (1:0.8) with different metal cathodes using the structure of ITO/PEDOT:PSS/ P3HT:PCBM/cathode. It is observed that the devices with Au, Ag and Mg electrodes show V_{OC} of 141 mV, 592 mV and 696 mV, respectively. Here V_{OC} shows a strong dependence on the metal electrodes and a variation of V_{OC} as high as 555 mV is observed, which is contrary to that observed in organic PV cells using the layered structure. In fact, *Mihailtechi* et al. [4.23] have reported the similar results and explained

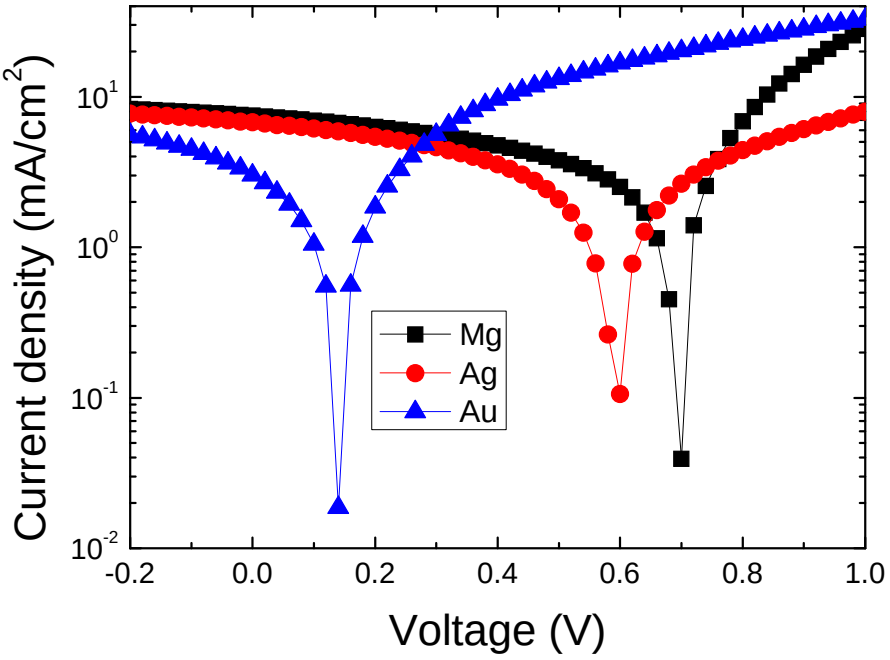

Fig. 4.3 Characteristics of the bulk HJ PV cells with different metals. The structure is ITO/PEDOT: PSS /1:0.8 P3HT:PCBM/cathode. A variation of V_{OC} as high as 555 mV is observed. The light intensity is 100 mW/cm^2.

the obvious dependence of V_{OC} on different cathodes in bulk HJ PV cells by modifying the classical MIM model.

However, since the layered and bulk HJ PV cells are both based on organic materials and the mechanisms of light absorption, exciton production, exciton dissociation and charge transport are also the same, it is not possible that V_{OC} of the two types of PV cells follows different mechanisms. Considering the differences of the two types of devices, the essential difference is that they have distinct structures. Compared with the layered HJ PV cell, there are no geometrically "flat" D/A and M/O interfaces in

the bulk HJ PV cell due to the formation of the interpenetrating network. It is supposed that the different dependences of V_{OC} on the metal electrodes should have relations with their distinct structures. In the following, how the different structures affect the behaviors of V_{OC} will be discussed.

4.4 Discussion

4.4.1 Theory

In principle, V_{OC} of a PV cell is a function of both electric and chemical potential energy gradients [4.8]. In the conventional inorganic (for example, silicon based) PV cells, electron-hole pairs are photogenerated in the same semiconducting phase, there are no photoinduced chemical potential gradients established, and only a classical built-in potential (V_{bi}) is required to separate the carriers. However, the situation is different for organic based PV cells. Because of the low dielectric constant and weak noncovalent electric interactions in organic materials, excitons are always produced rather than free carriers. It is well recognized that the most efficient exciton dissociation occurs at the D/A interface in organic materials. For simplification, we assume that all the excitons are dissociated at the D/A interfaces in organic PV cells and neglect the dissociation at M/O interfaces as that has been done by *Cheyns* et al. [4.26]. After exciton dissociation, the dissociated electrons and holes are separated into different phases of A and D. This photoinduced charge injection at the D/A interface will establish chemical potential gradients in the organic materials and then influence V_{OC}. At M/O interfaces, the electrodes can also inject carriers into the organic materials and influence V_{OC}. With knowing D/A and M/O interface conditions, the carrier concentration distribution and all

the electric variables in organic PV cells can be obtained at open circuit condition by using the "shooting algorithm".

4.4.1.1 Shooting algorithm

Let consider one dimension case. The general kinetic equations for electron and hole current densities in one dimension are usually expressed as

$$J_n(x) = -q\mu_n n(x)\frac{\partial U(x)}{\partial x} + qD_n\frac{\partial n(x)}{\partial x} \tag{4.1a}$$

$$J_p(x) = -q\mu_p p(x)\frac{\partial U(x)}{\partial x} - qD_p\frac{\partial p(x)}{\partial x} \tag{4.1b}$$

Where q is the elementary charge, n and p the electron and hole densities, μ_n and μ_p the electron and hole mobilities, D_n and D_p electron and hole diffusion coefficients, and U the electric potential which is given by the Poisson equation

$$\frac{\partial^2}{\partial x^2}U(x) = \frac{q}{\varepsilon}[n(x) - p(x)] \tag{4.2}$$

The diffusion coefficients ($D_{n,p}$) obey the Einstein relation

$$D_{n,p} = \mu_{n,p}\frac{k_B T}{q} \tag{4.3}$$

The continuity equations for the electron and hole carrier densities are

$$\frac{\partial n(t)}{\partial t} = \frac{1}{q}\frac{\partial J_n(x)}{\partial x} - R_n + G_n \tag{4.4a}$$

$$\frac{\partial p(t)}{\partial t} = -\frac{1}{q}\frac{\partial J_p(x)}{\partial x} - R_p + G_p \tag{4.4b}$$

Here, G_n and G_p are the electron and hole generation rates, R_n and R_p recombination rates, respectively. These are the basic equations in semiconductor; and are valid under light illumination and in the dark environment.

For D/A based organic PV cells, light created excitons do not affect the potential in organic materials due to its electric neutral property (equation (4.2)). Considering phase A where electrons are transported and holes can be neglected, the equations (4.1) and (4.2) at the open circuit condition (J=0) can be reduced to

$$J_n(x) = -q\mu_n n(x)\frac{\partial U(x)}{\partial x} + qD_n\frac{\partial n(x)}{\partial x} = 0 \tag{4.5}$$

$$\frac{\partial^2}{\partial x^2}U(x) = \frac{q}{\varepsilon}n(x) \tag{4.6}$$

The electric potential and the electric field (F(x)) have the relation

$$\frac{\partial U(x)}{x} = F(x) \tag{4.7}$$

Thus, if the boundary conditions (carrier concentrations) are known, the carrier concentration distribution and electric variables in phase A can be numerically calculated by using above equations based on the so-called “shooting algorithm”: at the first grid point, D/A interface, the potential of LUMO is set to zero, then the Fermi level (E_F) can be obtained by

$$U = -\frac{kT}{q}\ln\left(\frac{N_A}{n}\right) \tag{4.8}$$

Where N_A is the LUMO density of states in phase A, which is assumed to be 2.8×10^{25} m^{-3} in this work. All the parameters at D/A interface are known, except the electric field F(0). Guess a value for F(0). The electron concentration in the next grid point *i* is calculated by discretization of equation (4.5). Once the electron concentration in point *i* is known, one can calculate electrostatic potential and the electric field in point *i*, by equations (4.6) and (4.7). This is repeated until one arrives at the M/O interface, and the second boundary condition (electron concentration) at M/O interface is checked. This is repeated with improved guesses of *F*(0) until the second boundary condition is fulfilled. Same method can be used for D phase.

In order to use the shooting algorithm, the boundary conditions at D/A and M/O interfaces are needed. Now, we firstly consider one material phase (here is phase A) in the simple layered HJ PV cell which has geometrically "flat" D/A and M/O interfaces as shown in Fig. 4.4 (a).

4.4.1.2 Boundary conditions

D/A interface

Under light illumination, the created excitons diffuse to D/A interface and are dissociated into electron-hole pairs (polarons). These polarons can be dissociated into free carriers and the free carriers can also return to polarons. Under the steady-state condition, the number of polarons is determined by

$$\frac{dX}{dt} = G_X - k_X X - k_D X + \gamma np \tag{4.9}$$

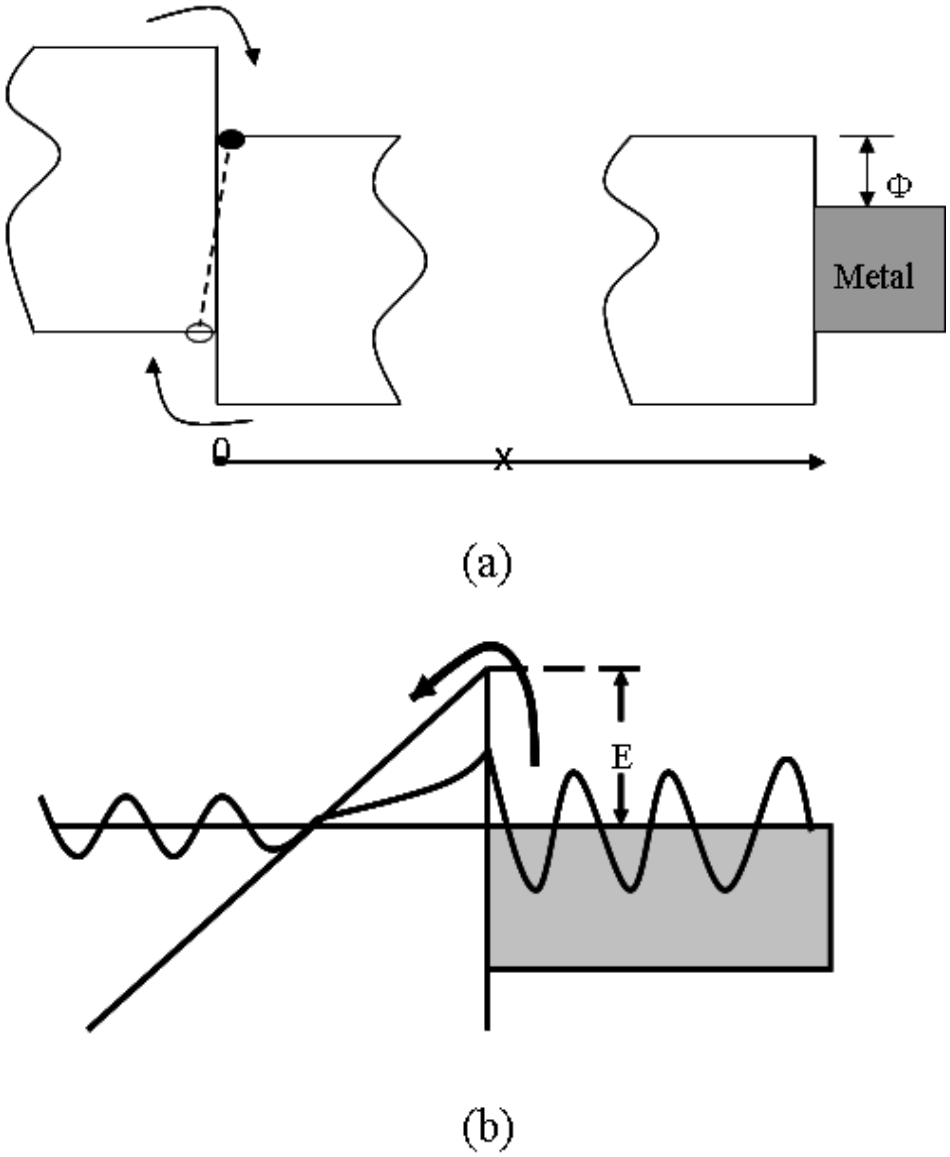

Fig. 4.4 (a) Bilayer HJ PV cell which has geometrically "flat" D/A and M/O interfaces. At the D/A interface, the excitons are dissociated into electrons and holes. After dissociation, hole and electron are still bound by the Coulombic attractive force. (b) Carrier injection from the metal to the organic material at the M/O interface. Thermionic emission and tunneling effect may exist at the M/O interface.

Where n and p are the electron and hole densities, G_X the amount of the dissociated excitons into polarons, k_X the decay rate to the ground state, k_D the dissociation rate of a bound pair, and γnp the excitons created due to the bimolecular capture of free charges at the interface. Usually G_X has a linear dependence on the incident light intensity

$$G_X = \alpha P_{\text{in}} \tag{4.10}$$

Where α is a constant. Considering the photoinduced carriers and the carrier generation/recombination process, the free carrier continuity equation at the open circuit condition is

$$\frac{\partial n}{\partial t} = k_D X - \gamma np - k_{SRH}\frac{np}{n+p} \tag{4.11}$$

The last term describes the Schokley-Read-Hall (SRH) recombination [4.26]. Assuming n in phase A and p in phase D are the same at the interface, the electron concentration (n) in phase A can be derived by combining equations (4.9)-(4.11). If the bimolecular recombination dominates at the interface,

$$n = \sqrt{\frac{k_D}{\gamma k_X}\alpha p_{\text{in}}} \tag{4.12}$$

and if the SRH recombination dominates at the interface,

$$n = \frac{2k_D}{k_{SRH}(k_D + k_X)}\alpha p_{\text{in}} \tag{4.13}$$

M/O interface

The carrier density at the M/O interface usually depends on the potential barrier between the metal and organic material. When the electric field is relatively low, the carrier density can de described by Richardson-Schockley theory [4.30] [Fig. 4.4 (b)] for thermionic emission

$$n = N_A \exp(-\frac{q(\phi_A - \Delta\phi)}{k_B T}) \tag{4.14}$$

with

$$\Delta\phi = \sqrt{\frac{q^3 F}{4\pi\varepsilon_0\varepsilon_r}} \tag{4.15}$$

Here, N_A is the LUMO density of states (DOS) of A, ϕ_A the barrier height between A and cathode, $\Delta\phi$ accounts for the barrier lowering effect. If the barrier is very thin and the electric field is very large, the carrier tunneling effect [Fig. 4.4 (b)] becomes important, and the carrier concentration at the M/O interface depends on the tunneling probability. According to the Wentzel–Kramers– Brillouin (WKB) approximation

$$n \propto \exp\left[-2\int \sqrt{\frac{2m}{\hbar}}\sqrt{V(x)-E}\,dx\right] \tag{4.16}$$

here, m is electron effective mass, V(x) the potential of the barrier, and E the energy of electron. When the tunneling happens, the carrier density at M/O interface increases rapidly. In real devices, the thermionic emission and tunneling injection exist together. In the low electric field, the thermionic emission dominates and at high electric field the

tunneling plays a major role. At the medium electric field, there is a transition region where both mechanisms need to be considered to determine the boundary conditions.

After knowing the D/A and M/O interface conditions, all the parameters in phase A can be obtained at the open circuit condition by using the "shooting algorithm" described in the above. For symmetry reasons, the same method can be applied to phase D. Thus, the behaviors of V_{OC} for layered and bulk HJ PV cells can be investigated.

4.4.2 Layered HJ PV Cells

In order to interpret the behavior of layered HJ PV cells, we firstly consider the light saturation condition for simplification. Under this condition, there are enough carriers generated at D/A interface under very intense light so that almost all the LUMO states of A at D/A interface are filled. On the other hand, at M/O interface the boundary condition is set by the injected carriers from the metal, which depends on the M/O barrier height [equation (4.14)]. Both the calculated electron carrier concentration and potential energy distribution in phase A are calculated and shown in Figs. 4.5 (a) and (b) with different M/O barrier heights from 0.0 eV to 1.0 eV. The x-scale is from the D/A interface to M/O interface [see Fig. 4.4 (a)], and the LUMO potential energy at D/A interface is taken as the ground potential energy. From Fig. 4.5 (a), at D/A interface, the electron carrier density is constant since all the LUMO states of A at D/A interface are filled under light saturation condition; on the other hand, at M/O interface, the electron carrier density decreases greatly with the increase of the barrier height, causing electron carrier concentration profile becoming steeper from D/A interface to M/O interface in the interior of phase A. Fig. 4.5 (b) shows the corresponding LUMO profile. It can be seen

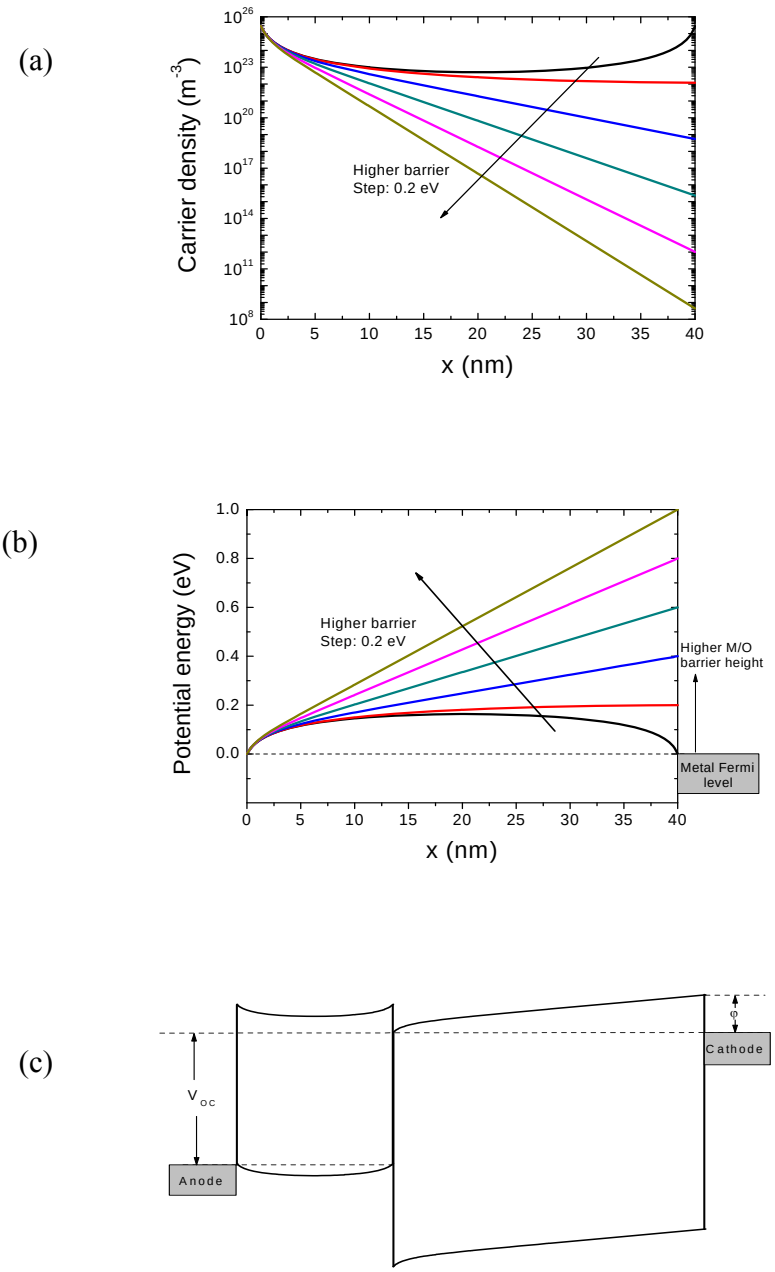

Fig. 4. 5 (a) Calculated carrier density profile for different barriers. Step: 0.2 eV. The positions of x=0 and 40 nm refer to the D/A and M/O interfaces, respectively. (b) The corresponding variation of LUMO profile. Light injected carriers at D/A interface will "pin" the metal Fermi level. Here, the LUMO potential at D/A interface is set as the ground potential. (c) Band diagram for a layered HJ PV cell with Ohmic anode and a 0.4 eV barrier cathode. HOMO of D and LUMO of A set the upper limit of V_{OC}. Not consider the barrier lowering effect.

that when M/O interface is with a large barrier, the LUMO profile is almost a straight line and there is no band bending because of the relatively low carrier injection. When M/O interface is Ohmic contact or there is very small barrier, an obvious band bending at M/O interface is observed due to the large amounts of electrons injected from the cathode causing the electron accumulation occurred at the phase A near M/O interface. *Mihailtechi* et al [4.23] have noted this band bending and claimed that it could decrease V_{OC}. However, according to our results, no matter whether it is Ohmic contact or non-Ohmic contact, V_{OC} should be the same. This is because that the Fermi level of the metal electrode is apt to be "pinned" to LUMO level of A at D/A interface irrespective with the barrier height as shown in Fig. 4.5 (b). Similarly, the same things happen in phase D. As a result, V_{OC} is determined by the difference of LUMO at A and HOMO of D at D/A interface and is independent with the barrier height at M/O interfaces or to say the work function of the metal electrodes. This explains why V_{OC} shows a direct relation with D/A offset energies in the experiments [4.13, 4.24]. According to the above results, an example of a bilayer HJ PV cell with an Ohmic contact at anode and a 0.4 eV barrier height at cathode is plotted in Fig. 4.5 (c).

In fact, it is difficult for the layered HJ PV cell to reach saturation under 1 sun illumination at room temperature [4.13]. Non-saturation condition, under which not all the LUMO states of A at D/A interface are filled, makes the value of V_{OC} become smaller. Fig. 4.6 (a) and (b) show the calculated electron density and potential energy under light non-saturation conditions assuming the M/O barrier height is kept at 0.5 eV. Since the barrier height is fixed, the electron carrier concentration at M/O interface does not change with different light intensities if neglecting the barrier lowering effect [equation (5.15)].

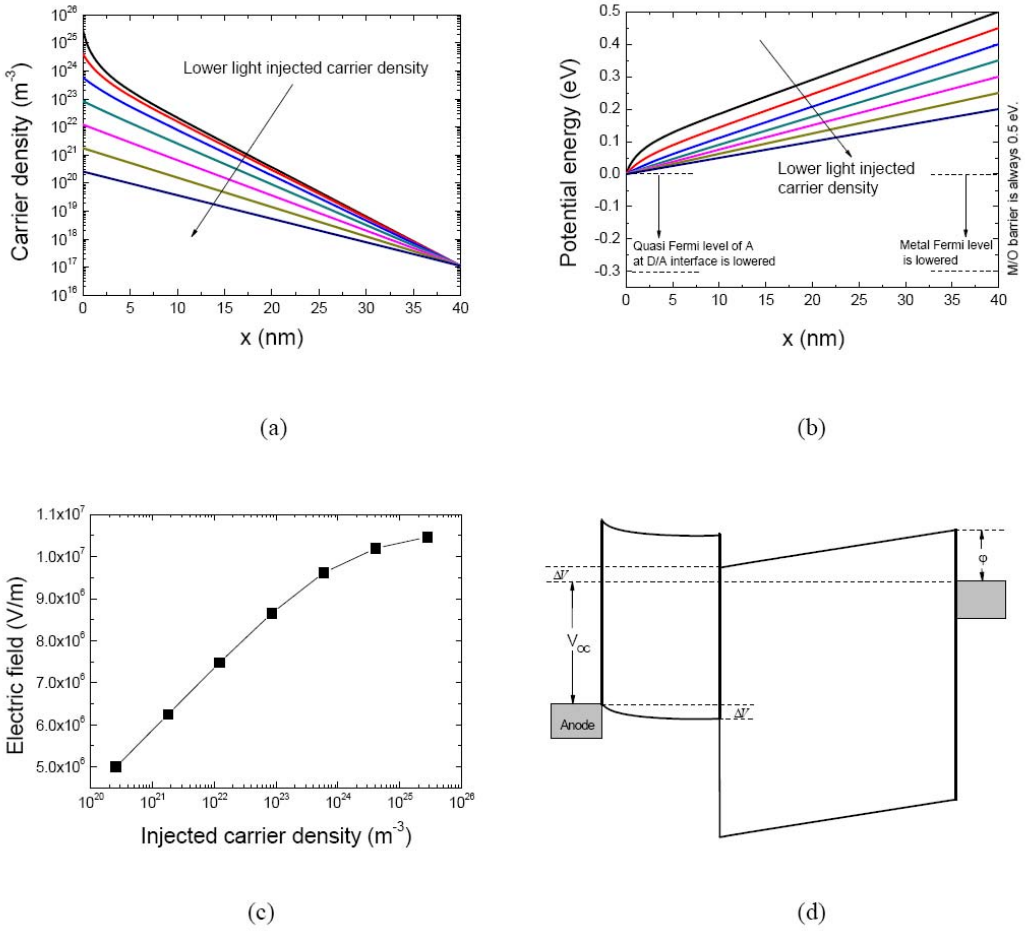

Fig. 4.6 (a) Carrier density profile for different light injection. The positions of x=0 and 40 nm refer to the D/A and M/O interfaces, respectively. (b) Corresponding LUMO diagram. The LUMO potential at D/A interface is set as the ground potential. (c) Corresponding variation of electric field at M/O interface. (d) Band diagram of a bilayer HJ PV cell with light injection carrier density of 8.46×10^{22}. ΔV means the decrease of V_{OC} under non-saturation condition. The value of V_{OC} is indicated. All above have a M/O barrier of 0.5 eV and do not consider the barrier lowering effect.

On the other hand, at D/A interface, the electron carrier density decreases with the drop of light intensity which causes carrier concentration profile less steep in the interior of A as shown in Fig. 4.6 (a). Fig. 4.6 (b) plots the corresponding LUMO profile. The quasi Fermi level of phase A at D/A interface is lowered below its LUMO level because of the

decrease of the injected carrier density at D/A interface. The metal Fermi level is also lowered since it has to be aligned to the quasi Fermi level of phase A at D/A interface. Due to the same reason, the Fermi level of the anode shifts up with the dropped light intensity. As a result, V_{OC} decreases with the dropping of the light intensity as observed in the studies [4.9, 4.13]. An example of a bilayer HJ PV cell with Ohmic anode and a 0.5 eV barrier cathode is shown in Fig. 4.6 (d) when the light injected carrier density at D/A interface is 8.46×10^{22} m^{-3}. Here, ΔV indicates the decreased value of V_{OC} in phase A due to the non-saturation condition. Assuming DOS of HOMO in phase D equals to that of LOMO in phase A (N_A=N_D), the value of V_{OC} is lowered by $2\Delta V$ compared with the D/A offset energies.

According to above discussions, no matter under light saturation or non-saturation conditions, the Fermi level of the metal electrode has to be aligned to the quasi Fermi level at D/A interface. Then in the layered HJ PV cells, V_{OC} seems to mainly depend on the D/A interface condition. This explains why V_{OC} only shows a very weak dependence on the electrodes. However, although the variation of V_{OC} with different electrodes is very small, the trend is clear that V_{OC} decreases slightly with the increase of metal cathode work function (see the statistic results of V_{OC} in the inset of Fig. 4.2). The barrier lowering effect at the M/O interface may account for this phenomenon. It is expected that the lowered barrier increases the carrier concentration at M/O interface [equation (4.14)], which shifts the metal Fermi level and then affects V_{OC}. Fig. 4.7 shows how the barrier lowering influences on V_{OC} under the light saturation condition. Due to the barrier lowering (Fig. 4.7 (b)), more carriers are injected into the organic material, which changes the boundary condition at the M/O interface compared with that not considering

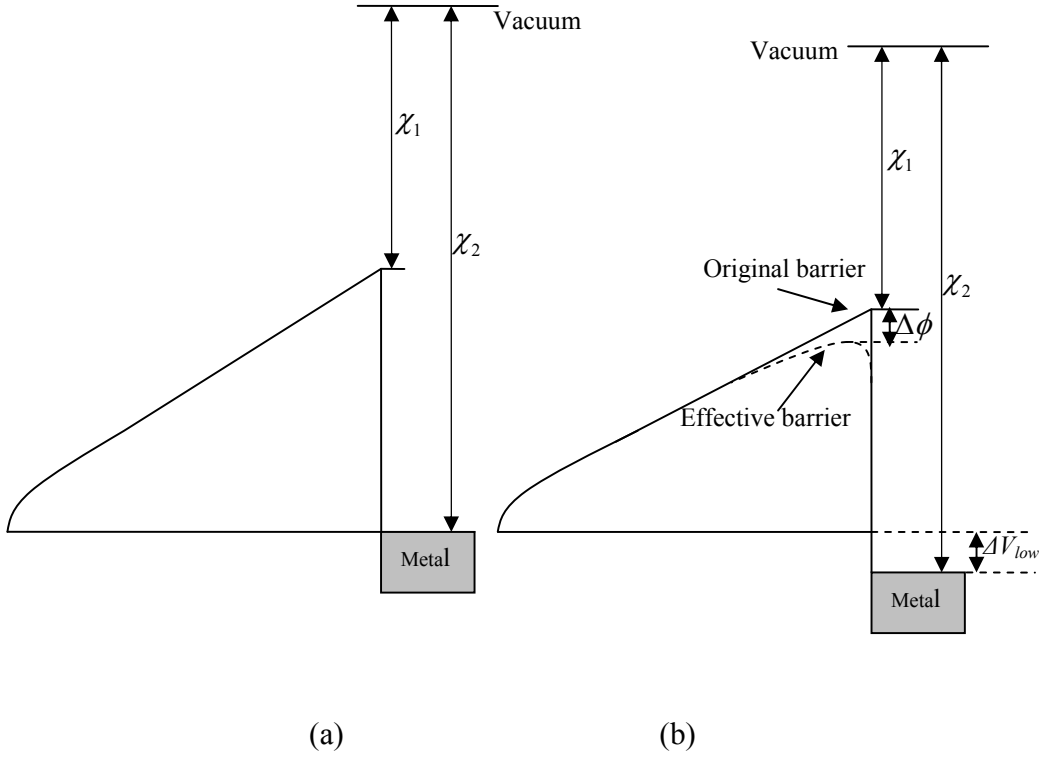

Fig. 4.7 Influence of barrier lowering on V_{OC}. (a) Not considering the barrier lowering effect (b) Considering the barrier lowering effect. The barrier lowering induces the decrease of V_{OC}. $\Delta\phi$ represents the value of barrier lowering, and ΔV_{low} represents the decrease of V_{OC}. The LUMO potential at D/A interface is set as the ground potential.

the barrier lowering effect. This lowers the metal electrode Fermi level and thus decreases V_{OC}. ΔV_{low} in Fig. 4.7 (b) indicates this effect. The value of ΔV_{low} depends on the electric field since the value of the barrier lowering depends on the electric field. Fig. 4.6 (c) shows the electric field at M/O interface under different light injection conditions when the M/O barrier height is 0.5 eV. There is only a small barrier lowering of about 0.020 eV at an electric field of 1×10^6 V/m and 0.064 eV at an electric field of 1×10^7 V/m as shown in Fig. 4.8. Thus, the corresponding value of ΔV_{low} is also small and then V_{OC}

shows a weak dependence on different electrodes. Although the barrier lowering is small, the trend is clear. The higher the metal work function is, the larger the electric field is at the cathode interface. Thus V_{OC} decreases slightly with the increase of the cathode work function (inset of Fig. 4.2).

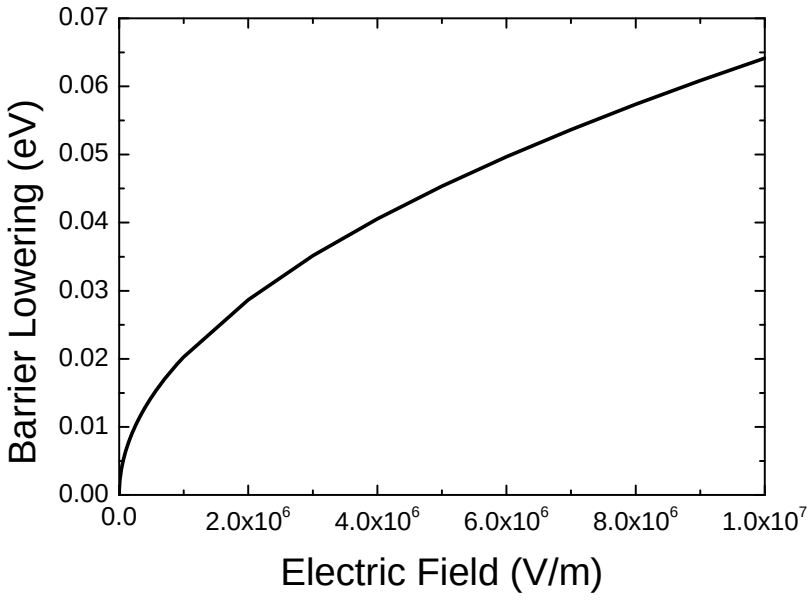

Fig. 4.8 Field dependent barrier lowering

Now, considering the light injection at D/A interface, electrode injection at M/O interface, and the distribution of DOS in organic materials, the expression for V_{OC} can be derived. If the bimolecular recombination dominates at the D/A interface,

$$qV_{\mathrm{OC}} = (HOMO_D - \Delta_{\mathrm{D}}) - (LUMO_A - \Delta_{\mathrm{A}}) - U_B - \frac{k_B T}{q} \ln \frac{\gamma k_X N_A N_D}{\alpha k_D} + \frac{k_B T}{q} \ln P_{in} - V_{Low} \qquad (4.17)$$

If the SRH recombination dominates at the D/A interface,

$$qV_{OC} = (HOMO_D - \Delta_D) - (LUMO_A - \Delta_A) - U_B - \frac{2k_BT}{q}\ln\frac{k_{SRH}(k_D + k_X)\sqrt{N_A N_D}}{2\alpha k_D} + \frac{2k_BT}{q}\ln P - V_{low} \quad (4.18)$$

where Δ accounts for the fact that the transport level in a Gaussian DOS locates below its center as shown in Fig. 4.1 (b), and its value is given by $\frac{5}{9}\frac{\sigma^2}{k_BT}$ with σ the broadening of DOS [4.23]. U_B is the polaron binding energy

$$U_B = \frac{q^2}{4\pi\varepsilon_0\varepsilon_r a} \quad (4.19)$$

here a is the initial separation distance of the electron-hole pair at the interface. V_{Low} accounts for the lowered voltage due to the barrier lowering. The rest accounts for the influence of light intensity.

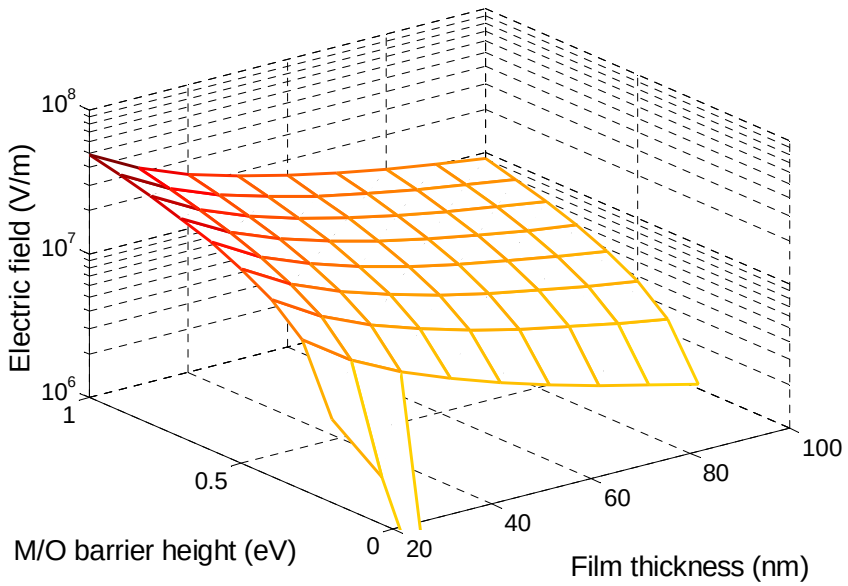

Fig. 4.9 Variation of electric field at the M/O interface with the M/O barrier and the film thickness under light saturation condition (semi-logarithm scale). Only the positive electric field is shown (positive direction point to the interface).

The value of V_{Low} depends on M/O interface conditions. For the case of the layered HJ PV cells, they have geometrically "flat" D/A and M/O interfaces, and the effective thickness from the D/A interface to the M/O interface is large (usually several tens nanometers). Thus the electric field at M/O interface is relatively small as shown in Fig. 4.9 and then V_{Low} is very low. Thus it shows that V_{OC} almost does not depend on the metal electrode work function, which is consistent with the reported study [4.26].

4.4.3 Bulk HJ PV Cells

Different from the layered HJ PV cells, a strong dependence of V_{OC} on the electrodes in bulk HJ PV cells was observed (Fig. 4.3). In theory, V_{OC} of bulk HJ PV cells should obey the same principle as that in layered HJ PV cells. Compared with layered HJ PV cells, the essential difference is the distinct device structure. In the bulk HJ PV cell, the D (polymer) and A (fullerene) materials are mixed together to form the interpenetrating network which makes the D and A domains very small. In addition to the "non-flat" D/A interface, the average distance from the D/A interface to the M/O interface (denoted as "effective thickness" in the following discussion) is significantly decreased compared with the layered HJ PV cell, which influences the electric field at M/O interface. The trend in Fig. 4.9 has shown that the electric field is expected to become very large when the M/O barrier is very high and the effective thickness is very small. Considering the extremely small effective thickness in bulk HJ PV cells, even the carrier tunneling effect may occur when there is a high M/O barrier. Then the number of injected carriers from the electrode becomes very large. This induces a large value of V_{Low}. The higher the barrier is, the larger the value of V_{Low} will be. Compared with the Ag and Mg electrodes, the barrier for the Au electrode is the highest and thus the V_{OC} is

expected to be the smallest, which explains the very large variation of V_{OC} with different metal electrodes.

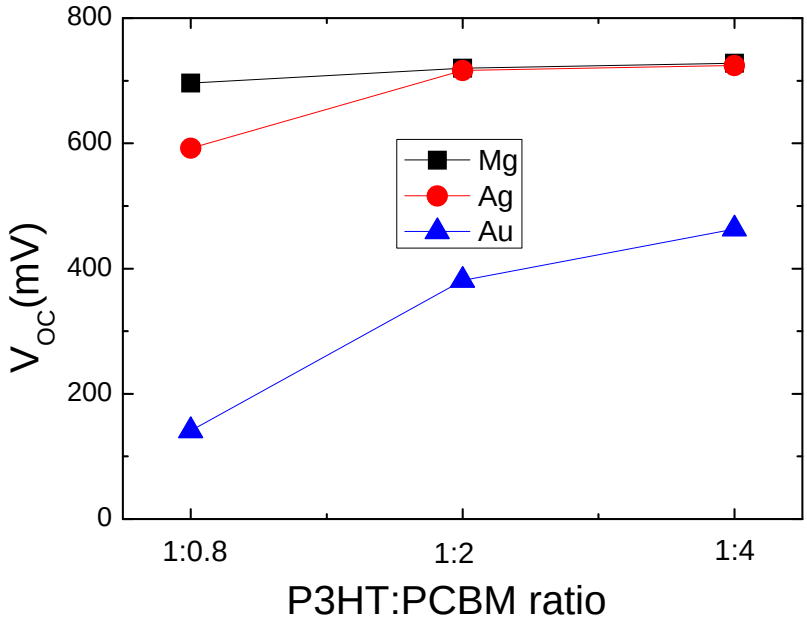

Fig. 4.10 Variation of V_{OC} with the different weight ratios of P3HT: PCBM (1:0.8, 1:2 and 1:4). All the devices have the same structure except the metal cathode. V_{OC} for Au device is obviously increased with a higher PCBM ratio, while V_{OC} for Mg electrode almost keeps constant.

If the above discussion is correct, V_{OC} of bulk HJ PV cells can be changed by modulating the effective thicknesses of phase D and phase A, which can be obtained by changing the D and A ratio in the blend layer. For high PCBM ratio, the PCBM domain is expected to be enlarged. This means that the effective thickness of phase A becomes large. For a high M/O barrier, the increased thickness of phase A decreases the electric field effectively. As a result, the value of V_{Low} becomes small and V_{OC} is expected to become large. However, for a low M/O barrier, the change of the electric field is

relatively small and then the increase of V_{OC} is expected to be small. Fig. 4.10 shows the variation of V_{OC} for the devices with different P3HT:PCBM ratios. As expected, for the Au electrode, V_{OC} is increased from 141 mV (P3HT:PCBM 1:0.8 weight ratio) to 381 mV (P3HT:PCBM 1:2 weight ratio) and further increased to 463 mV (P3HT:PCBM 1:4 weight ratio). For Ag electrode, V_{OC} is increased from 592 mV (P3HT:PCBM 1:0.8 weight ratio) to 716 mV and then almost kept as a constant. The variation of V_{OC} for Mg electrode is the smallest. These results are in accordance with the expectation and thus confirm the validity of the proposed explanation.

The assumption that V_{OC} of bulk HJ PV cells obeys the same principle as that of layered HJ PV cells can also be validated by the variation of V_{OC} in bulk HJ PV cells with the light intensity. According to equation (4.17) or (4.18), V_{OC} should have a linear relation with the logarithm of light intensity. As the prediction, V_{OC} indeed linearly depends on the logarithm of light intensity as shown in Fig. 4.11. The lines with the slop of around 60 mV/decade means that the bimolecular recombination dominates at the D/A interface, which is consistent with the previous study that the bimolecular recombination is the most important recombination mechanism in OSCs [4.10]. The similar results of V_{OC} on the light intensities reported by *Koster* et al. in OSCs based on MDMO-PPV:PCBM [4.32] confirm our observation. Then it can be concluded that V_{OC} of bulk HJ PV cells obeys the same mechanism as layered HJ PV cells and the different dependences of V_{OC} on the electrodes origin from their distinct structures.

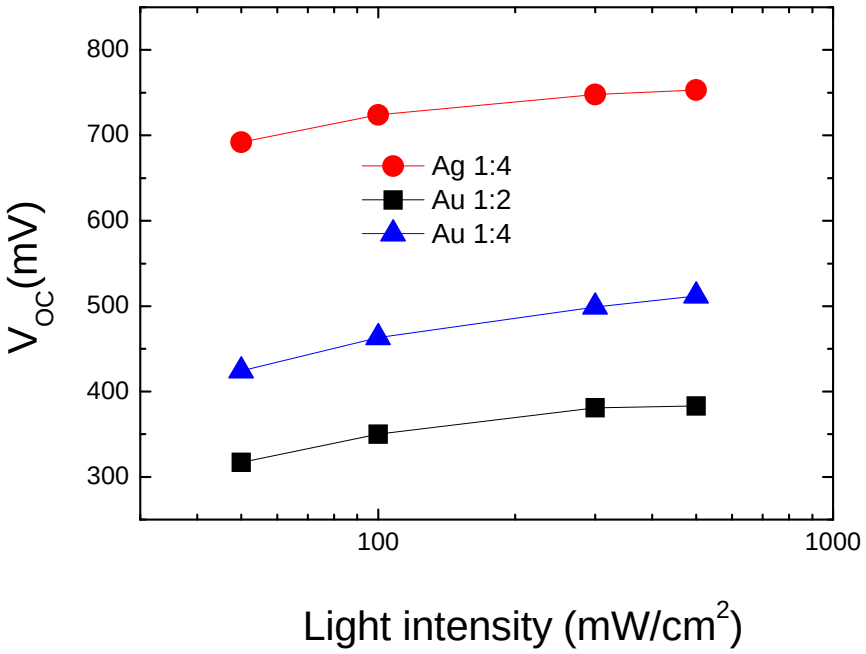

Fig. 4.11 Variation of V_{OC} with the light intensity for devices with different P3HT:PCBM weight ratios. The weight ratios are labeled in the graph after metal names. All the devices have the same structure except the metal cathode. The lines show the slopes around 60 mV/decade which means that the bimolecular recombination dominates at the D/A interface.

As discussed above, V_{OC} of bulk HJ PV cells strongly depends on the effective thickness of D and A domains, which is to say that their V_{OC} can be influenced by the morphology of the blend layer. After thermal annealing, the D and A domains increase due to the phase separation. Correspondingly, the D and A effective thicknesses are increased, which explains why V_{OC} is usually enhanced after the thermal annealing for bulk HJ PV cells [4.14, 4.20]. V_{OC} of bulk HJ PV cells also strongly depends on the electrodes. This gives us a way to increase V_{OC} of bulk HJ PV cells by using the interface

engineering. In fact, many works has been done to increase V_{OC} of bulk HJ PV cells by modifying the interface between the blend layer and the electrode [4.33-4.36]. However, because V_{OC} of layered HJ PV cells only slightly depends on the electrodes, there are few papers which focus on the interface engineering to increase V_{OC} of layered HJ PV cells.

4.5 Summary

In this chapter, we studied the origin of V_{OC} in layered and bulk HJ PV cells. It was found that V_{OC} of layered and bulk HJ PV cells show different dependences on the electrodes. When the electrodes are changed, V_{OC} of layered HJ PV cells almost keeps constant, while V_{OC} of bulk HJ PV cells shows an obvious variation. The experimental results and theoretical analysis showed that V_{OC} of the two types of PV cells follow the same mechanism and are mainly determined by the light injected carriers at the D/A interface and the electrodes. But their distinct structures lead to the different dependences of V_{OC} on the electrodes. The layered HJ PV cells have geometrically "flat" D/A and M/O interfaces which make the effective thickness from the D/A interface to the M/O interface is very large. The large effective thickness leads to a thick barrier and a low electric field at M/O interface. Thus the barrier lowering is low and the number of carriers injected from the metal electrode by thermionic emission is relatively small. Under this condition, the light injected carriers at D/A interface tend to "pin" the Fermi level of the electrodes. As a result, V_{OC} shows only a very weak dependence on the work function of the electrodes. On the other hand, the formation of the interpenetrating network in bulk HJ PV cells decreases D and A domain dimensions greatly which makes the effective thicknesses of D and A domains very small. When there is a very high potential barrier, the electric field is very high at M/O interface and even the carrier

tunneling effect may occur. Then a large number of carriers are injected from the metal electrode into the organic materials. Thus, the light injected carriers at D/A interface cannot "pin" the metal Fermi level any more. As a result, a strong dependence of V_{OC} on the metal electrodes for bulk HJ PV cells is observed. V_{OC} of layered HJ PV cells is difficult to be increased by the interface engineering. However, the interface engineering can help to increase V_{OC} of bulk HJ PV cells. This gives us a way to increase V_{OC} in bulk HJ PV cells.

References

[4.1] N. S. Sariciftci, L. Smilowitz, A. J. Heeger and F. Wudl, Science, 258, 1474 (1992).

[4.2] G. Yu, J. Gao, J. C. Hummelen, F. Wudl and A. J. Heeger, Science, 270, 1789 (1995).

[4.3] Z. Tan, C. Yang, E. Zhou, X. Wang and Y. Li, Appl. Phys. Lett., 91, 023509 (2007).

[4.4] M. Y. Chan, S. L. Lai, M. K. Fung, C. S. Lee and S. T. Lee, Appl. Phys. Lett., 90, 023504 (2007).

[4.5] W. J. Potscavage, J. S. Yoo and B. Kippelen, Appl. Phys. Lett., 93, 193308 (2008).

[4.6] J. Y. Kim, K. Lee, N. E. Coates, D. Moses, T. Q. Nguyen, M. Dante and A. J. Heeger, Science, 317, 222 (2007).

[4.7] C. F. Zhang, S. W. Tong, C. Y. Jiang, E. T. Kang, D. S. H. Chan and C. X. Zhu, Appl. Phys. Lett., 92, 083310 (2008).

[4.8] B. A. Gregg and M. C. Hanna, J. Appl. Phys., 93, 3605 (2003).

[4.9] J. A. Barker, C. M. Ramsdale and N. C. Greenham, Phys. Rev. B, 67, 075205 (2003).

[4.10] L. J. A. Koster, E. C. P. Smits, V. D. Mihailetchi and P. W. M. Blom, Phys. Rev. B, 72, 085205 (2005).

[4.11] C. Waldauf, M. C. Scharber, P. Schilinsky, J. A. Hauch and C. J. Brabec, J. Appl. Phys., 99, 104503 (2006).

[4.12] C. M. Martin, V. M. Burlakov, H. E. Assender and D. A. R. Barkhous, J. Appl. Phys., 102, 104506 (2007).

[4.13] B. P. Rand, D. P. Burk and S. R. Forrest, Phys. Rev. B, 75, 115327 (2007).

[4.14] C. F. Zhang, S. W. Tong, C. Y. Jiang, E. T. Kang, D. S. H. Chan and C. X. Zhu, Appl. Phys. Lett., 93, 043307 (2008).

[4.15] G. Dennler, H. J. Prall, R. Koeppe, M. Egginger, R. Autengruber, and N. S. Sariciftci, Appl. Phys. Lett., 89, 073502 (2006).

[4.16] X. Wang, E. Perzon, J. L. Delgado, P. Cruz, F. Zhang, F. Langa, M. Andersson and O. Inganäs, Appl. Phys. Lett., 85, 5081 (2004).

[4.17] L. A. A. Pettersson, L. S. Roman and O. Inganas, J. Appl. Phys., 86, 487 (1999).

[4.18] G. Li, V. Shrotriya, Y. Yao and Y. Yang, J. Appl. Phys., 98, 043704 (2005).

[4.19] A. J. Moule and K. Meerholz, Adv. Mater., 20, 240 (2008).

[4.20] Y. Kim S. A. Choulis, J. Nelson, D. C. Bradley, S. Cook and J. R. Durrant, Appl. Phys. Lett., 86, 063502 (2005).

[4.21] C. M. Ramsdale, J. A. Barker, A. C. Arias, J. D. MacKenzie, R. H. Friend and N. C. Greenham, J. Appl. Phys., 92, 4266 (2002).

[4.22] C. J. Brabec, A. Cravino, D. Meissner, N. S. Sariciftci, T. Fromherz, M. T. Rispens, L. Sanchez and J. C. Hummelen, Adv. Funct. Mater., 11, 374 (2001).

[4.23] V. D. Mihailetchi, P. W. M. Blom, J. C. Hummelen and M. T. Rispens, J. Appl. Phys., 94, 6849 (2003).

[4.24] M. C. Scharber, D. Wuhlbacher, M. Koppe, P. Denk, C. Waldauf, A. J. Heeger and C. J. Brabec, Adv. Mater. (Weinheim, Ger.), 18, 789 (2006).

[4.25] A. Cravino, Appl. Phys. Lett., 91, 243502 (2007).

[4.26] D. Cheyns, J. Poortmans, and P. Heremans, C. Deibel, S. Verlaak, B. P. Rand and J. Genoe, Phys. Rev. B, 77, 165332 (2008).

[4.27] T. Ishwara, D. D. C. Bradley, J. Nelson, P. Ravirajan, I. Vanseveren, T. Cleij, D. Vanderzande, L. Lutsen, S. Tierney, M. Heeney and I. McCulloch, Appl. Phys. Lett., 92, 053308 (2008).

[4.28] G. G. Malliaras, J. R. Salem, P. J. Brock and J. C. Scott, J. Appl. Phys., 84, 1583 (1998).

[4.29] V. D. Mihailetchi, L. J. A. Koster, J. C. Hummelen and P. W. M. Blom, Phys. Rev. Lett., 93, 216601 (2004).

[4.30] S. M. Sze, Physcis of Semiconductor Devices (Wiley, New York, 1981).

[4.31] V. D. Mihailetchi, H. X. Xie, B. de Boer, L. J. A. Koster and P. W. M. Blom, Adv. Funct. Mater., 16, 699 (2006).

[4.32] L. J. A. Koster, V. D. Mihailetchi, R. Ramaker and P. W. M. Blom, Appl. Phys. Lett., 86, 123509 (2005).

[4.33] C. J. Brabec, S. E. Shaheen and N. S. Saricifci, Appl. Phys. Lett., 80, 1288 (2002).

[4.34] E. Ahlswede, J. Hanisch and M. Powalla, Appl. Phys. Lett., 90, 163504 (2007).

[4.35] C. F. Zhang, S. W. Tong, C. Y. Jiang, E. T. Kang, D. S. H. Chan and C. X. Zhu, Appl. Phys. Lett., 94, 103305 (2009).

[4.36] F. Zhang, M. Ceder and O. Inganas, Adv. Mater., 19, 1835 (2007).

Chapter 5
Experimental studies to improve P3HT:PCBM Bulk HJ OSCs

In the previous two chapters, the most important parameters (J_{SC} and V_{OC}) in OSCs have been investigated theoretically. The factors affecting these parameters have been indicated. In this chapter, the experimental studies are carried out to increase J_{SC} and enhance V_{OC} based on the previous studies. The overall device performance is also optimized at the end of this chapter.

5.1 The effect of annealing sequence on J_{SC}

5.1.1 Introduction

Various experimental studies have been reported for the blended P3HT:PCBM bulk HJ solar cells [5.1-5.12]. Although PCBM can act as a good electron acceptor in this type of solar cells, the undesirable destruction of ordering in the P3HT chains takes place in the presence of PCBM [5.12-5.14]. Compared to the P3HT material alone, the optical absorption of the P3HT:PCBM system has a weaker absorption in red light region. For this type of solar cells, numerous reports have indicated that PCE increases with the crystallinity of P3HT [5.1-5.6]. Annealing [5.8-5.12, 5.15] has been widely applied to recover the P3HT crystallinity. In this section, it is pointed out that the post-annealing (anneal the device after the cathode deposition) can improve the performance of the solar cells more effectively than the pre-annealing (anneal the device before the cathode

deposition) because of the Al cathode confinement. This is supported by XPS study. It indicates that the stronger contact could be formed at the interface between the P3HT:PCBM blend and the Al cathode, due to the formation of Al-O-C bonding and the P3HT-Al complex for the post-annealed device. The Al cathode can effectively prevent the overgrowth of the PCBM molecules. UV-Vis absorption spectroscopy also shows the improved light absorption property in the post-annealed blend layer.

5.1.2 Experimental

All ITO substrates used were cleaned with detergent, deionized water, acetone and isopropanol for 15 mins, respectively. For the device fabrication, the PEDOT:PSS (Baytron P VP AI 4083) with a thickness of ~50 nm was firstly spin coated on the top of the ITO surface and dried at 110 °C in an oven. The P3HT:PCBM blend layer (1:0.8 weight ratio) was then spin coated from the dichlorobenzene solvent on the PEDOT:PSS layer. The Al metal (~100 nm) was then further thermally evaporated through a shadow mask giving an active device area of 0.2 cm^2. Different annealing conditions were used: (i) without annealing (pristine device); (ii) pre-annealing and (iii) post-annealing. All annealing processes were finished by using direct contact with a hot plate for about 10 min in the dry box. The solar cells were characterized by a Keithley 2400 source-measure unit in the dark and under Am 1.5 solar illumination at intensity of 100 mW/cm^2. Absorption spectra of organic films on glass substrates were measured by Shimadzu UV-3101 PC UV-VIS-NIR Spectrophotometer. The structural analysis of the samples was investigated by using a Shimadzu X-ray diffractometer with a copper x-ray beam (λ = 0.1542 nm).

The x-ray photoelectron spectroscopy (XPS) samples were consisted of identical sandwiched structure: ITO coated glass/P3HT:PCBM(100 nm)/Al(3 nm). The XPS spectra were measured by transferring the samples to the chamber of a Kratos AXIS HSi spectrometer at once. The operating pressure of the analysis chamber was maintained at 8 x 10^{-9} Torr. A 1486.71 eV monochromatic Al Kα x-ray gun source was used to achieve the Al 2p, O 1s, C 1s and S 2p spectra.

Tapping mode atomic force microscopy (AFM) measurements of three samples were taken with a Nanoscope III A (Digital Instruments) scanning probe microscope. The samples were prepared in the same sequence as the XPS samples. Two of the samples were arranged to undergo pre-annealing and post-annealing respectively, while one was used as the reference. The phase images and the line scanning profiles of the samples were then recorded under air operation.

5.1.3 Experimental Results and Discussion

To compare the impact of the annealing process on the performance of the PV device, three solar cells were fabricated based on P3HT:PCBM in an identical manner except for the annealing conditions. They are pristine solar cell, pre-annealed solar cell and post-annealed solar cell to represent the cells without annealing, with pre-annealing and with post-annealing, respectively. A plot of I-V curves for the devices is shown in Fig. 5.1.

The pre-annealed and the post-annealed devices exhibit an obvious increase in J_{SC} compared with the pristine device. PCE is also greatly improved correspondingly. The pristine device only shows PCE of 0.13%. However, after the annealing, PCE increases to 1.58 % for the pre-annealed device and near 3% for the post-annealed device. Obviously,

the post-annealed device shows the best performance. Compared with the pre-annealed device, FF of the post-annealed device increases from 0.43 to 0.61. The increases in J_{SC} and FF imply a significant reduction in the series resistance (R_s) of the solar cell (defined as the slope of the I-V curve at I=0 mA/cm^2). In fact, the value of R_s is reduced from 22.2 Ωcm^2 for pre-annealed device to 5.64 Ωcm^2 for post-annealed device.

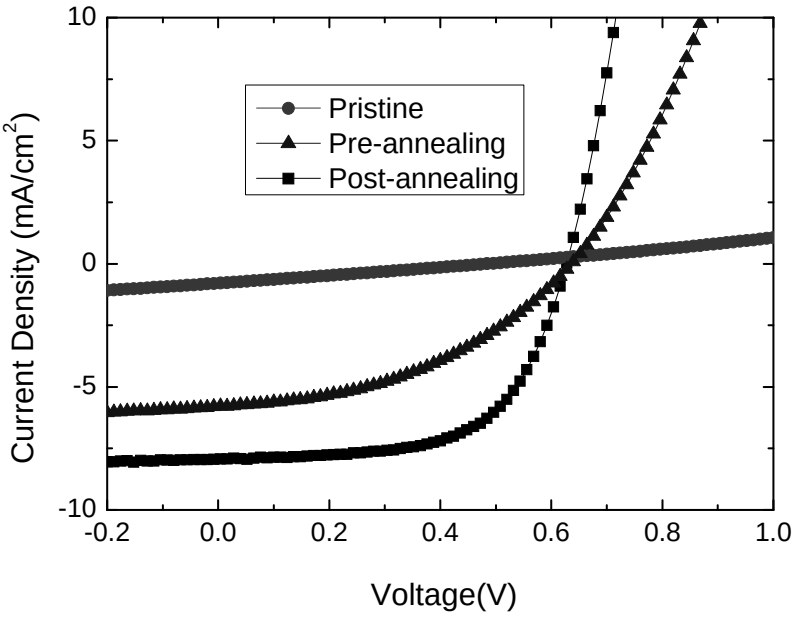

Fig. 5.1 I-V characteristics of the PV cells ITO/PEDOT:PSS/ P3HT:PCBM/Al under AM 1.5 illumination, with the P3HT:PCBM active layer thickness about 80 nm.

The post-annealed device shows the better performance than the pre-annealed device. It is inferred that different interfacial structures should be addressed from the two systems. To investigate the chemical structure at the interface of the polymer and Al

metal, the surface-sensitive XPS analysis is thus studied. Only a thin Al metal (3 nm) is deposited on the polymer blend in order to prevent weak XPS scanning signals from the polymer. Multiple peaks have been fitted in the XPS core level spectra by using Gaussian method. According to the published values of the binding energy (BE) as listed in Table 5.1, the bonding states are clearly marked on each XPS spectrum.

Table 5.1 Summary of the XPS binding energies of different bonding states.

Samples	Al 2p [eV]	C 1s [eV]	O 1s [eV]	S 2p [eV]
Al-O-C	74.6 [5.17]	286.2 [5.17]	531 [5.18]	
Al_2O_3	74.95 [5.16]		532.3 [5.24]	
Al-S	76 [5.19,5.22]			162.45 [5.19, 5.22,5.25]
COOH		289.5 [5.25]	532.3 [5.25]	
C-C		285.1 [5.19,5.22,5.25]		
C-S		285.7 [5.20,5.21]		164.1,165.3 [5.19-5.22]

The evolutions of the corresponding Al 2p, C 1s, O 1s and S 2p core level spectra are illustrated in Fig. 5.2. The bottom and the top curves in each graph are the spectra of the pre-annealed and the post-annealed samples, respectively. The position of the Al 2p main line is located at the BE of 74.95 eV, which is attributed to the Al oxide [5.16]. Both the two samples exhibit a peak at the BE of 74.6 eV, which is corresponded to the Al-O-C bonding [5.17]. The existence of the Al-O-C bonding has been confirmed by the

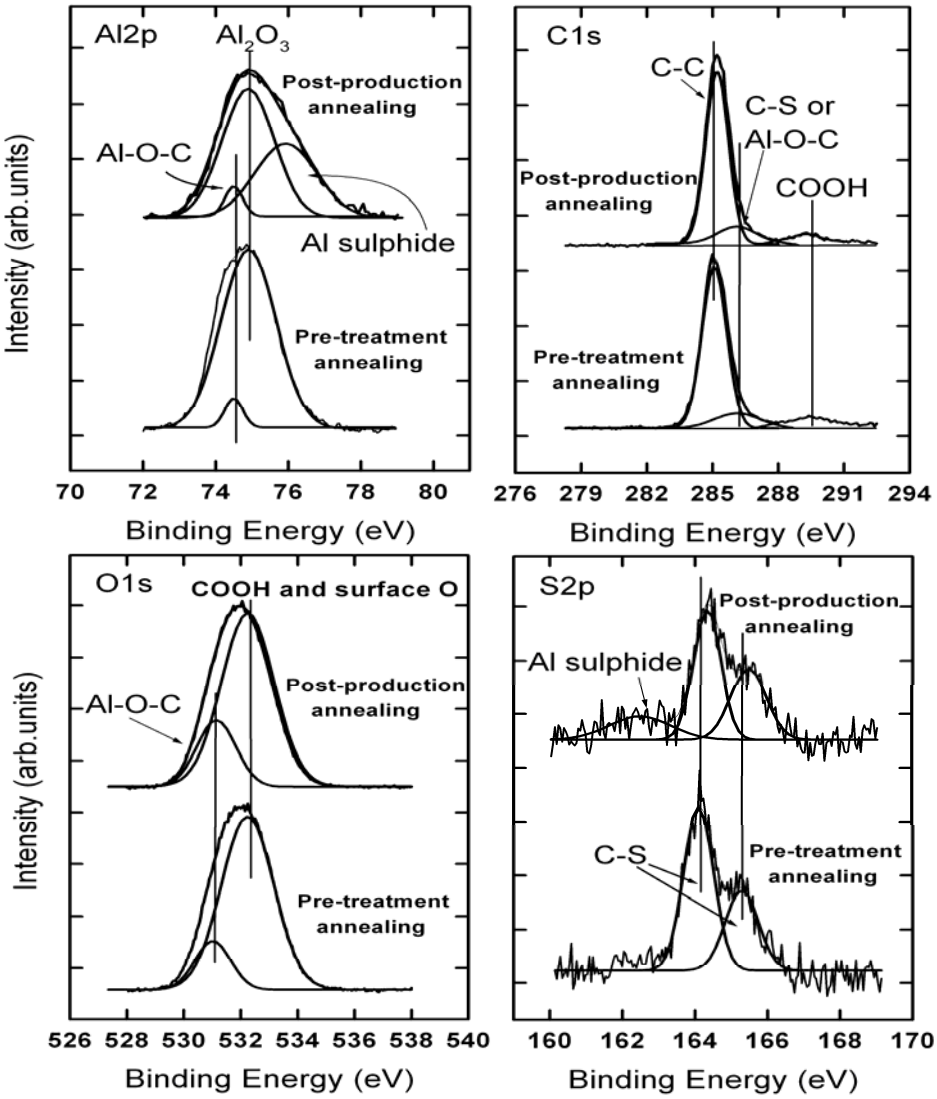

Fig. 5.2 High-resolution Al 2p, C 1s, O 1s and S 2p XPS spectra of the pre-annealed and the post-annealed samples. The configuration of the samples is ITO/P3HT:PCBM(100 nm)/Al(3 nm).

peaks located at the BE of 286.2 eV [5.17] in the C 1s spectrum and 531 eV [5.18] in the O 1s spectrum. It has been proposed that the Al-O-C bonding can improve the contact between the polymer and the metal [5.2]. Our results indicate that this favorable bonding exists in both the pre-annealed and the post-annealed samples. However, an additional

shoulder peak at the BE of 76 eV in the Al 2p spectrum is observed in the post-annealed sample. The evolution of this new chemical state suggests that there are structural differences between the samples that are annealed in different sequence. From the S 2p spectrum of the pre-annealed sample, the typical peaks of P3HT appeared at the BE of 164.1 eV ($2p_{3/2}$) and 165.3 eV ($2p_{1/2}$) due to the spin-orbit coupling are discovered [5.19-5.22]. We can also observe the emergence of an extra shoulder peak at the BE of 162.4 eV in the post-annealed sample. The donation of electron density from the Al metal to the thiophene ring of P3HT is suggested to be the reason of the formation of the peak at 162.4 eV [5.19, 5.22]. The interaction between P3HT and the Al metal is likely to occur under the post-annealing.

It has been reported that the Al atoms have a preference to react with the carbonyl groups than the thiophene ring of the polymer [5.22, 5.23]. Similarly, our results show that the Al metal preferentially reacts with the carbonyl oxygen in PCBM to form the Al-O-C bonding than the thiophene ring of P3HT. This can be understood by the fact that the electronegativity of the oxygen atoms is higher than the sulfur and carbon atoms [5.17].

Though the charge transfer between the Al metal and the thiophene ring of P3HT (including some conjugated carbon atoms) only occurs in the post-annealed system, the location of the C 1s main peak between two annealing conditions only has a slight energy difference (~0.1 eV shift in BE). This is because the C 1s peak is dominated by the aliphatic carbon atoms while the Al metal preferentially reacts with the carbon atoms in the conjugated system (thiophene ring of P3HT in this case) [5.21, 5.22, 5.24]. Thus the signal arose from the interaction between P3HT and the Al is too weak to be detected in the C 1s spectrum in the post-annealed sample.

Based on the above findings, we propose that there is a transition from P3HT to P3HT-Al complex upon the post-annealing as shown in Fig. 5.3. Since the direct reaction between the Al metal and the sulfur atoms is unlikely to occur because of the inherently high electron density on the sites, thus we believe that the Al metal forms bonds with the carbon atoms on the thiophene ring in the positions adjacent to the sulfur atom and affects the electron density of the sulfur atoms [5.20, 5.25]. In the P3HT-Al complex, the overall charge density of the sulfur atoms is smaller than that of the pristine P3HT. Thus the S 2p peaks located at the BE of 164.1 eV and 165.3 eV are shifted to the higher BE side at 164.3 eV and 165.5 eV after the post-annealing, respectively.

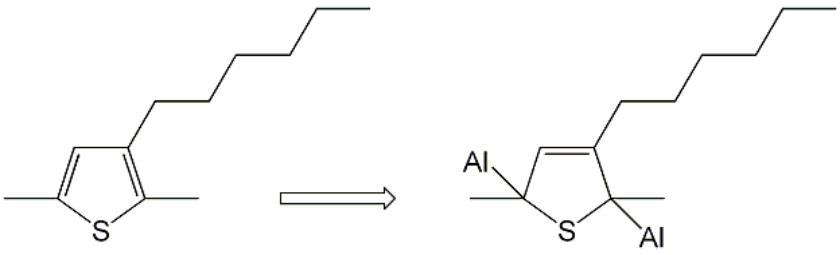

Fig. 5.3 The molecular structure transits from P3HT to P3HT-Al complex.

Different notions about the role of similar complex have been reported previously [5.17, 5.26]. *Ling* et al. proposed that the Al metal can effectively transfer the electron to the conjugated polymer with the sulfide species and this feature makes it as a potential cathode for polymeric electronics [5.17]. *Boman* et al. reported that the delocalization of the π–electron system is reduced due to the Al_2-thiophene complexes [5.26]. We believe that the latter effect does not play an important role in our solar cells because a good PV effect is achieved from the post-annealed device. From our point of view, the improved

PV effect in the post-annealed device is partly attributed to the stronger contacts at the polymer/metal interface with two interfacial bondings of Al-O-C and P3HT-Al complexes. Facilitated charge collection via the improved contact can result in the reduction of the series resistance in the post-production annealed solar cell.

The effect of the annealing sequence on the morphology is investigated by the AFM study. Figs. 5.4 a-f show the phase images and the cross-sectional profiles of the different samples. The sample structure is ITO/P3HT:PCBM/Al. The root mean square roughness of the pristine, the pre-annealed and the post-annealed samples are 5.5, 6.3 and 5.9 nm respectively. Both annealing sequences lead to the growth of the polymer domains and the increase of the surface roughness.

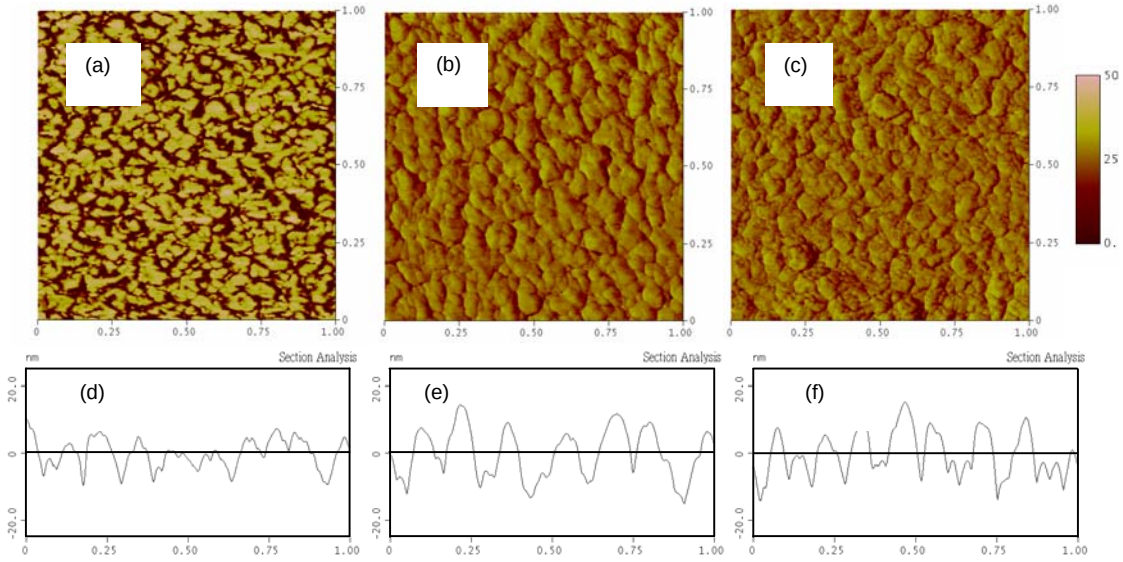

Fig. 5.4 Tapping-mode AFM phase images of Al covered P3HT:PCBM blend films: a) pristine, b) pre-annealed and c) post-annealed. Corresponding cross sectional profiles are shown in d) to f).

It has been shown that the main effect of the annealing is the redistribution of PCBM [5.3, 5.12, 5.13, 5.27, 5.32]. Diffused PCBM from the P3HT:PCBM system allows the transformation from P3HT aggregates to P3HT crystallites. The P3HT:PCBM blend with such conformation can improve the optical absorption property of P3HT and hence the PV effect. However, the rapid PCBM diffusion is also the main limiting parameter in the blend films [5.28, 5.29]. This induces the formation of the large PCBM aggregates in the P3HT:PCBM polymer blend and deteriorates the interpenetrating networks [5.28, 5.30]. Charge generation and interfacial contact between P3HT and PCBM will most likely be reduced due to the overgrowth of PCBM [5.12, 5.28]. Thus the appropriate annealing should be undergone to prevent the overgrowth of PCBM.

The appropriate annealing should be performed to prevent PCBM from overgrowing. In the pre-annealed devices, it is very easy for the PCBM domain to overgrow. Compared with the pre-annealing (Fig. 5.4e), the average peak-to-peak height and the width of the polymer domains can be reduced 20% and 33%, respectively by using the post-annealing (Fig. 5.4f). Smaller domain size implies that the overgrowing of PCBM can be effectively prevented by overlaying an Al cathode. A better nanoscale control of the morphology can be promoted by prohibiting a coarse phase segregation of PCBM molecules. Similar metal effect was also demonstrated on the organic surface by using silver caps [5.31]. More efficient charge separation in the increased interfacial areas between P3HT and PCBM is believed to be one of the reasons for the improvement of the post-annealed device. The XPS and AFM results show that the Al capping layer not only induces a stronger interfacial contact at the polymer/metal interface, but also reduces the

roughness of the Al covered polymer (prevents the overgrowth of PCBM) in the annealing process.

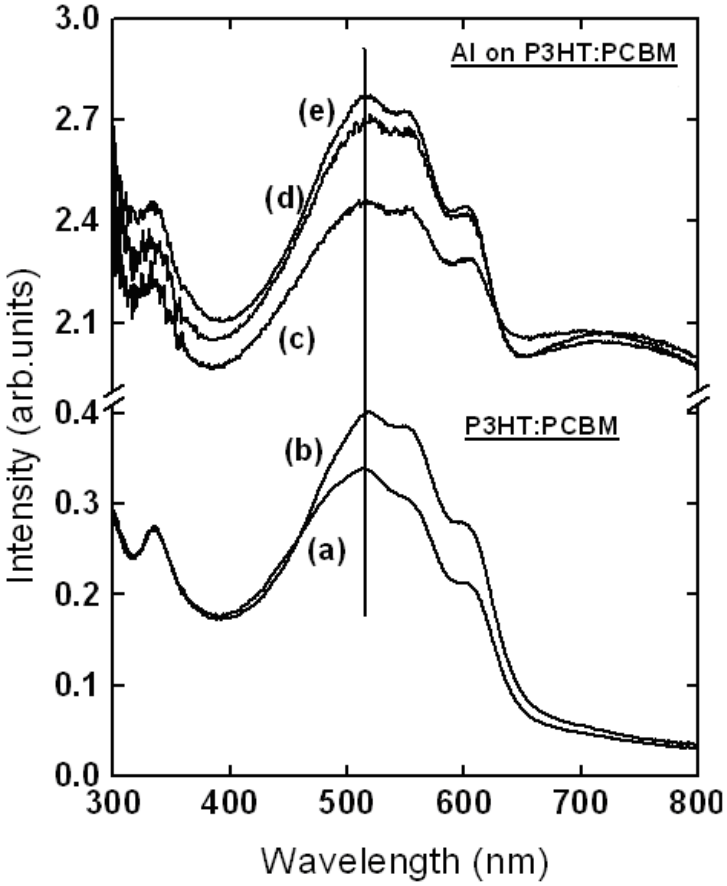

Fig. 5.5 The optical absorption spectra of the P3HT:PCBM blend films: a) pristine, b) annealed, c) pristine with Al, d) pre-annealed with Al and e) post-annealed with Al.

Fig. 5.5 shows the effect of the annealing on the UV-Vis absorption spectra for the P3HT:PCBM blend films. As indicated in spectra (a) and (b) in Fig. 5.5, an apparent increase in the optical absorption can be achieved after the thermal annealing of the polymer films. To understand the effects of the Al metal on the light harvesting property

of the polymer film during the annealing, the absorption spectra of the polymer capped with the Al metal are also measured. Similar spectral improvement is arisen upon annealing. Particularly, the most progressive increase in absorption is found in the post-annealed polymer film.

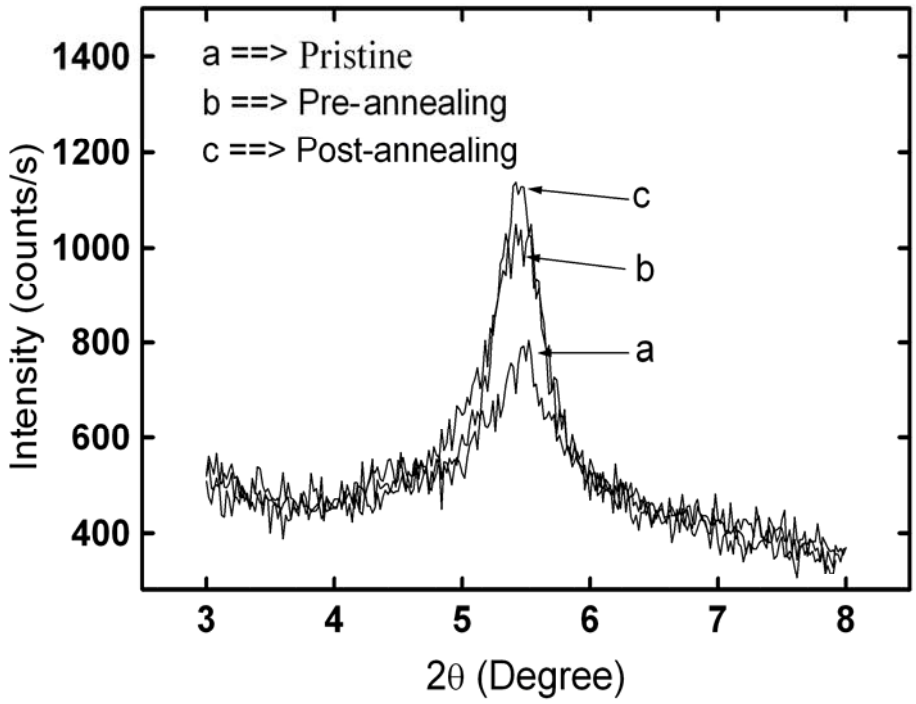

Fig. 5.6 The x-ray diffraction spectra of the Al covered P3HT: PCBM blend films: a) pristine, b) pre-annealed and e) post-annealed.

The enhancement in the light absorption can be explained by the XRD results. The XRD data are obtained from the samples made of polymer capped with the Al metal. The evolution of the XRD diffraction peak at $2\theta=5.4°$ is a well known signature for the P3HT crystallites [5.33] as shown in Fig. 5.6. The highest height (h) and the smallest full width at half maximum ($\Delta_{2\theta}$) of the peak reflect the largest P3HT crystallinity inside the post-

annealed polymer layer. Based on *Bragg's* law [5.34] and *Scherrer* relation [5.35], the corresponding lattice constant (*d*) and the size of the polymer crystallites (*L*) can be determined respectively.

$$n\lambda = 2d\sin\theta \tag{5.1}$$

$$L = \frac{0.9\lambda}{\Delta_{2\theta}\cos\theta} \tag{5.2}$$

where λ is the wavelength of the x-ray, and θ is the Bragg's angle.

Table 5.2 Summary about x-ray diffraction peaks of P3HT:PCBM under different annealing conditions (calculated from Fig. 5.6 and equations (5.1), (5.2)).

Annealing	2θ [°]	$\Delta_{2\theta}$ [°]	*h* [counts/s]	*L* [nm]	*d*
No	5.49	0.83	318	9.6	1.61
Pre-treatment	5.44	0.61	596	13	1.625
Post-production	5.44	0.45	617	17.7	1.625

As shown in Table 5.2, all polymer layers have the lattice constant of 1.62 ± 0.01 nm. The peak height, which is proportional to the number of the P3HT crystallites per unit volume [5.34], of the post-annealed sample is the highest. In contrast to the pristine P3HT:PCBM layer, the sizes of the P3HT crystallites can be dramatically increased by 35% and 84% (calculated by the the value of L in Table 5.2) after the pre- and the post-annealing, respectively. The most pronounced P3HT crystallinity leads to the improvement of the light harvesting property of the post-annealed films [5.1, 5.3]. From

the literature, strong diffusion of PCBM from the P3HT matrix reduces the P3HT crystallinity and optical absorption property [5.1, 5.36]. Therefore, it is expected that the efficient inhibition of the overgrowth of PCBM by the overlaying Al metal can facilitate the crystallization of the P3HT during the annealing. This conformation should also increase the inter-chain interaction among the P3HT chains, result in more delocalized conjugated π electrons, and increase the optical absorption. Thus the charge generation can be facilitated with the larger light harvesting property of the post-annealed films.

5.1.4 Conclusion

The sequence of the thermal annealing is critical for the performance of the P3HT:PCBM based solar cells. As shown by the XPS, AFM, UV-Vis and XRD studies, the post-annealing should be performed to enhance PCE of the devices. We attribute the increased PCE to three factors: (i) the improved contact at polymer/aluminum interface due to the formation of Al-O-C and P3HT-Al complex; (ii) the improved phase-structured morphology due to the prohibition of the overgrowth of PCBM and (iii) the enhanced P3HT crystallinity and thus a better light harvesting property of the polymer film. These advantageous factors can facilitate the charge collection, separation and generation in the post-annealed devices.

5.2 The effect of cathode deposition on V_{OC}

5.2.1 Introduction

To improve the device performance further, it is very clear that another very important approach of enhancing V_{OC} must be considered. As discussed in chapter 4, V_{OC}

is proportional to the offset energy between HOMO of D and LUMO of A [5.37, 5.38]. Then in order to enhance V_{OC}, we can increase the offset energy between HOMO of D and LUMO of A. However, this method usually decreases J_{SC}, because a high bandgap absorber is required which has a large mismatch with the solar spectrum. Therefore it is challenging to increase V_{OC} while maintaining or increasing J_{SC} at the same time. In addition, the best performance of the state-of-art devices is almost based on some special materials (such as P3HT, PCBM, CuPc anc C_{60}). Thus it is important to increase V_{OC} based on these given materials. Recently, enhancement of V_{OC} in the polymer solar cells has been achieved by using a very thin layer of LiF between the active layer and the cathode [5.39, 5.40]. LiF can increase V_{OC} by introducing dipoles at the cathode interface. However, the extra layer of LiF and its critical thickness control increase the complexity of the fabrication process.

In this section, we will demonstrate a simple method to achieve a very strong enhancement of V_{OC} while not affecting J_{SC} and *FF* by only using the e-beam deposited Al cathode in the polymer solar cells. The method of e-beam deposition, which is the industrial process of choice for many large area metallic coating, has rarely been applied to devices based on organic materials because of its possible damage to the organic layer due to the existence of the energetic particles. Here we show that e-beam deposited Al cathode can effectively increase V_{OC} and enhance the performance of OSCs. Compared with the device with the thermal evaporated Al cathode (V_{OC}=596mV), the increased V_{OC} (664 mV) makes the overall PCE improved greatly. Through the investigations of the electrical characteristics, it is found that the deep interface traps in polymer induced by the e-beam deposition play an important role for the enhancement of V_{OC}.

5.2.2 Experimental

The devices were fabricated on ITO-coated glass substrates. After routine solvent cleaning (treated sequentially with detergent, de-ionized water, acetone, and isopropanol in an ultrasonic bath for about 15 minutes), the dried ITO glass substrates were treated with oxygen plasma for about three mins. Then the filtered PEDOT:PSS suspension was spin coated on the top of the ITO surface under ambient condition and dried at 110 °C in an oven. The P3HT:PCBM solution dissolved in dichlorobenzene with a weight ratio of 1:0.8 was spin coated on the top of the PEDOT:PSS film in the glove box to form the active layer. Finally, Al cathode was deposited by e-beam evaporation or the thermal evaporation through a shadow mask. P3HT and PCBM single layer devices were also fabricated. Finally the complete devices were annealed in the nitrogen. The current-voltage (I-V) characteristics were measured using a Keithley 2400 parameter analyzer in the dark and under a simulated light intensity of 100 mW/cm^2 (AM 1.5G) calibrated by an optical power meter.

5.2.3 Experimental results and discussion

To compare the impact of the metal deposition methods on the performance of the PV devices, two types of solar cells were fabricated in an identical manner except for the cathode deposition methods. One used the thermal evaporated Al cathode, and the other used the e-beam deposited Al cathode. All these devices were measured after the post-annealing process.

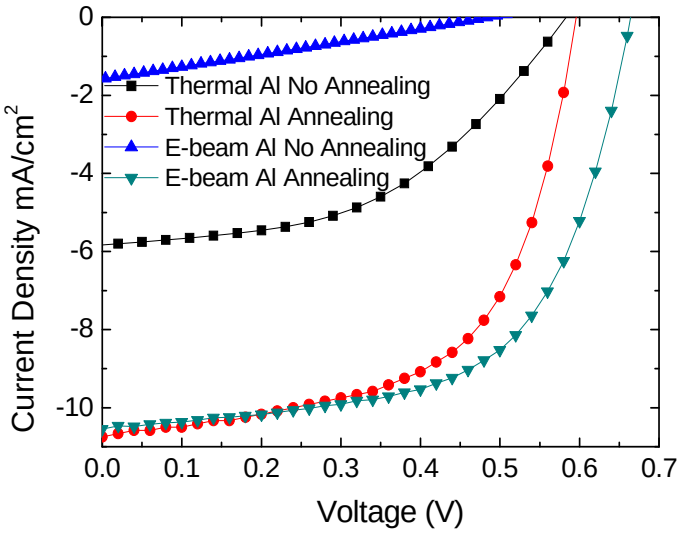

(a)

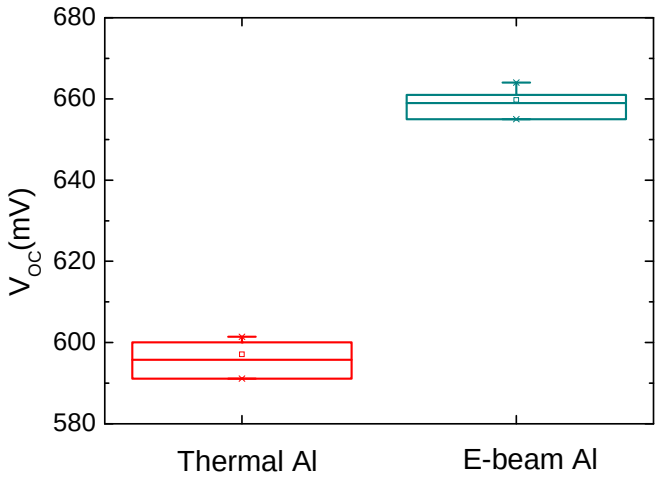

(b)

Fig. 5.7 (a) I-V characteristics of typical solar cells with e-beam deposited Al cathode and thermal evaporated Al cathode as fabricated and after annealing at 160°C for 10 minutes. And (b) Statistical results of V_{OC} for the both types of solar cells after annealing at 160°C for 10 minutes.

Fig. 5.7 (a) shows the I-V characteristics of the devices with the e-beam deposited Al cathode (e-beam Al device) and the thermal evaporated Al cathode (thermal Al device). After thermal annealing at 160^{o}C for 10 mins, both of the two types of devices show the comparable J_{SC} and *FF* (10.75 mA/cm^2, 60% for the thermal Al device and 10.55 mA/cm^2, 61% for the e-beam Al device). However, their V_{OC} shows different behaviors. As shown in Fig. 1 (a), the thermal annealing process only slightly increases V_{OC} from 583 mV to 595 mV for the thermal Al device. But an obviously higher V_{OC} of 664 mV is obtained for the e-beam Al device after the thermal annealing. The higher V_{OC} obtained by the e-beam Al device than the thermal Al device is more easily observed from the statistical results of V_{OC} as shown in Fig. 5.7 (b). As a result, compared with the thermal Al device (V_{OC}=595 mV), the increased V_{OC} (664 mV) by using the e-beam deposited Al cathode makes the overall PCE obviously increased by 12.4% (from 3.79% to 4.26%).

To well understand the influence of the e-beam deposited Al on the device performance, the I-V characteristics of the e-beam Al devices under different thermal annealing conditions are shown in Fig. 5.8 (a). Similar with the reported thermal Al devices and the results of the previous section, both J_{SC} and *FF* increase significantly after the thermal annealing. However, different from the thermal Al device where the increased value of V_{OC} is relatively small (form 580 mV to 600 mV), a very strong enhancement of V_{OC} is observed for the e-beam Al device. As shown in Fig. 5.8 (b), V_{OC} is increased steadily with the increase of the annealing temperature until it begins to saturate when the temperature is above 180^{o}C. The strong boost in V_{OC} makes the performance improve further. As shown in Fig. 5.8 (a), although J_{SC} and *FF* of the

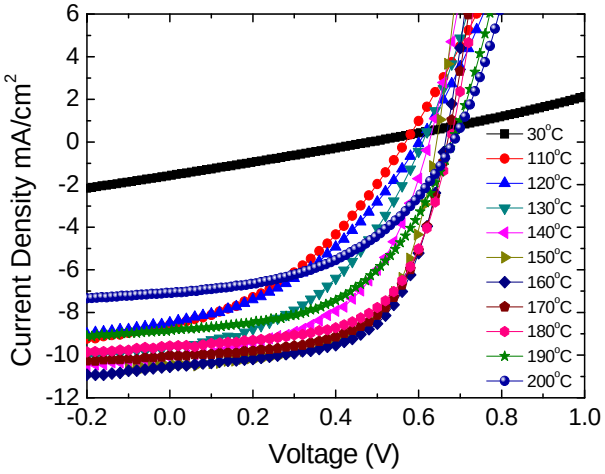

(a)

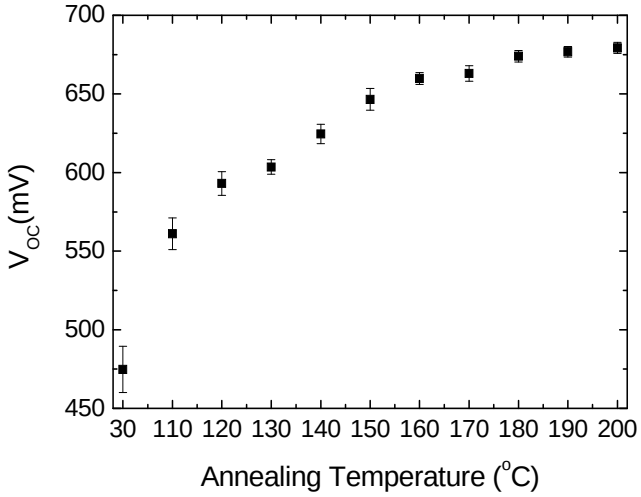

(b)

Fig. 5.8 (a) I-V characteristics of devices with the e-beam evaporated Al cathode that have undergone the thermal annealing from room temperature (30°C) to 200°C for 10 minutes. (b) Statistical results of V_{OC} under different annealing temperatures. V_{OC} is increased steadily with the increase of the annealing temperature until it begins to saturate when the temperature is above 180°C.

devices are almost the same for the annealing temperature of 150 °C (10.49 mA/cm^2, 61%) and 160 °C (10.55 mA/cm^2, 61%), the increased V_{OC} makes the ovrerall PCE further increase from 4.09% (150 °C) to 4.26% (160 °C).

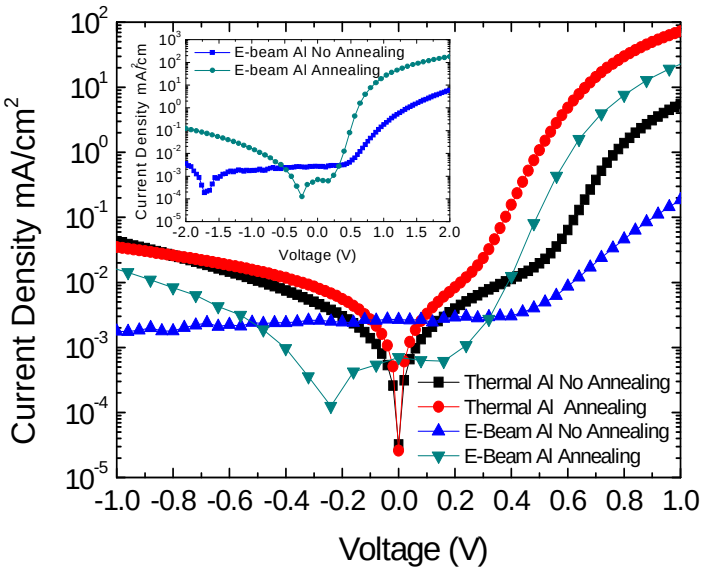

Fig. 5.9 Dark I-V characteristics of typical P3HT:PCBM solar cells with e-beam deposited Al cathode and thermal evaporated Al cathode as fabricated and after annealing at 160°C for 10 minutes.

In order to understand the origin of the enhancement of V_{OC}, the dark I-V curves for the e-beam Al device and the thermal Al device are investigated. As shown in Fig. 5.9, obvious differences are shown for the two types of devices. For the thermal Al device, the minimum current ("current zero") is observed when the voltage is zero. However, an obvious shift of current zero is observed for the e-beam Al device before and after the thermal annealing. This indicates that the deep traps are induced in the e-beam Al device [5.42]. It is noticed that the unique difference between the two types of devices is the cathode deposition method. Considering the existence of energetic particles of Al in the

e-beam deposition, these deep traps are believed to be induced by the damage of the blend layer in the cathode deposition process.

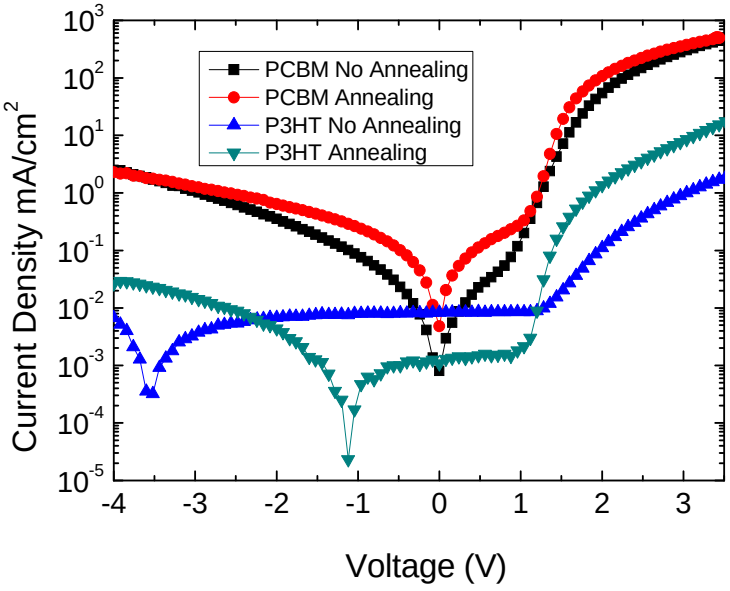

Fig. 5.10 Dark I-V characteristics of P3HT and PCBM single layer devices with e-beam deposited Al cathode as fabricated and after annealing at 160^{o}C for 10 minutes.

Since there are two different materials, P3HT and PCBM, in the solar cells, single layer of P3HT or PCBM has been used to fabricate devices with e-beam deposited Al cathode to find if the traps are located in P3HT or PCBM domains. Fig. 5.10 exhibits their dark I-V characteristics. No shift of current zero is observed for PCBM single layer device before and after the thermal annealing. This implies that PCBM is immune from the damage of the e-beam deposition. However, a very obvious shift of current zero is observed in the P3HT single layer device. This suggests that the energetic particles in the e-beam deposition damage and induce the deep interface traps in P3HT. The shift of

current zero is decreased after the thermal annealing. This trend is the same as in the P3HT:PCBM solar cell (inset in Fig. 5.10) and thus confirms that the deep traps in P3HT:PCBM solar cell is located in P3HT.

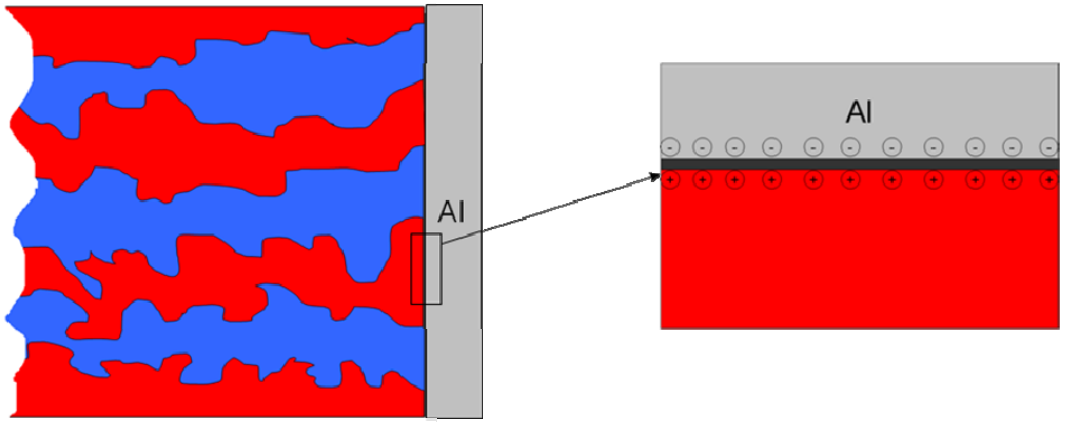

Fig. 5.11 Schematics illustrating the effects of deep interface hole traps on the polymer-fullerene solar cell. Red region means P3HT domain, and Blue region means PCBM domain. E-beam deposited Al cathode induces deep hole traps at P3HT/Al interface, and these positive trapped holes will induce the negative image charges in the cathode and thus forms the "dipoles".

The existence of the deep interface traps in P3HT can affect the device electrical characteristics and should be responsible to the strong enhancement of V_{OC}. However, the behind mechanism is still not well understood. Here a possible interpretation is proposed. Since P3HT is a p-type material, holes will be trapped in these deep traps. These positive trapped holes can induce the negative image charges in the cathode and thus form the "dipoles" as shown in Fig. 5.11. It is well known that even a monomolecular dipole layer can cause a significant vacuum level offset and lower the metal work function as has been shown for a very thin LiF layer [5.39, 5.40]. Similarly, here the interface "dipoles"

induced by the interface deep traps can also lower the Al effective work function and thus increase V_{OC}. Recently, *Ahlswede* et al. [5.43] reported that sputtered cathode can increase V_{OC}. We believe that it is also due to the deep interface hole traps induced by the sputter deposition.

As shown in Fig. 5.9 and Fig. 5.10, the shift of current zero changes with the annealing temperature. This implies that the annealing temperature can change the distribution of these deep traps, which explains why V_{OC} varies with the thermal annealing temperature (Fig. 5.8 (b)). When the temperature cannot change the trap distribution any more, V_{OC} should also keep constant. This is reflected by the gradual saturation of V_{OC} above 180^{o}C. Because these deep traps exist at the surface of P3HT (induced in the e-beam deposition), it should not influence the formation of the optimized morphology in the interior of the P3HT:PCBM layer. At the same time, PCBM is immune from the damage, thus the carrier extraction should not be affected because the electrons transport in PCBM and are collected by the cathode while holes transport in P3HT and are collected by the anode. As a result, the e-beam Al device obtains an increased V_{OC} and, at the same time, maintains the similar J_{SC} and *FF* as the thermal Al device.

5.2.4 Conclusion

In this section, the influence of metal deposition on V_{OC} was investigated. It was found that the energetic particles in the e-beam deposition can damage the surface of P3HT and induce deep hole traps at the surface while leave the fullerene unaffected. It was proposed that the deep trapped holes will induce the negative image charges in the cathode and form “dipoles”. These “dipoles” lower down the Al effective work function

and thus induce a very strong increase of V_{OC}. By using e-beam deposited Al cathode instead of the thermal evaporated Al cathode, V_{OC} was obviously increased from 596 mV to 664 mV while maintaining J_{SC} and *FF* almost unchanged, which made PCE improved by 12.4%.

5.3 Overall optimization of P3HT:PCBM OSCs

5.3.1 Introduction

The annealing process can efficiently improve the performance of P3HT:PCBM OSCs. As discussed above, the performance enhancement is related to the annealing sequence. Post-annealing is more favored by the devices. E-beam deposited Al cathode is also observed to efficiently increase V_{OC}. In this section, all the OSCs were made with the e-beam deposited Al cathode and post-annealed. These devices were used to optimize the overall solar cell performance.

Because the active layer is very thin in OSCs compared with the incident light wavelength, the optical interference effect influences the absorption and then J_{SC} as discussed in chapter 3. According to the simulated results based on the optical model, the thickness is optimized around the first and second optical interference peaks in this chapter.

5.3.2 Experimental

The fabrication process is the same as before. The devices were fabricated on the ITO-coated glass substrates. After routine solvent cleaning (treated sequentially with detergent, de-ionized water, acetone, and isopropanol in an ultrasonic bath for about 15 minutes), the dried ITO glass substrates were treated with oxygen plasma for about three

mins. Then the filtered PEDOT:PSS suspension was spin coated on the top of the ITO surface under ambient condition. The P3HT:PCBM solution dissolved in dichlorobenzene with a weight ratio of 1:0.8 was spin coated in the glove box. Finally, Al cathode was deposited by e-beam evaporation through a shadow mask. All the devices have same structure: ITO\PEDOT:PSS\P3HT:PCBM\Al, and only the thicknesses of the P3HT:PCBM active layers are different. The active layer thickness was controlled by changing the spin speed and solution concentration. Then different annealing temperatures are tested for the devices based on post-annealing to find the optimized conditions. The current-voltage (I-V) characteristics were measured using a Keithley 2400 parameter analyzer in the dark and under a simulated light intensity of 100 mW/cm^2 (AM 1.5G) calibrated by an optical power meter.

5.3.3 Experimental results and discussion

Optical interference effects and active layer thickness optimization

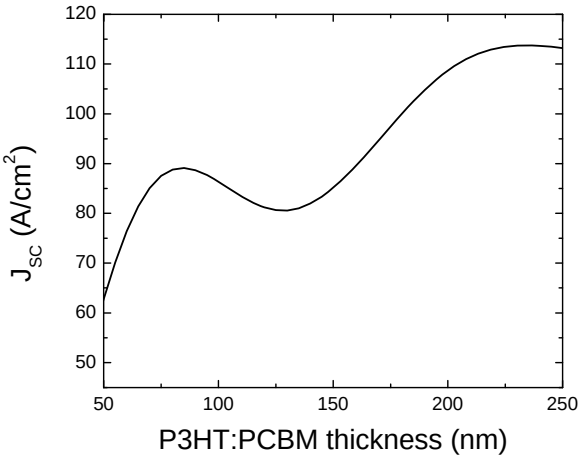

Fig. 5.12 J_{SC} versus P3HT:PCBM thickness, P3HT:PCBM with weight ratio of 1:0.8 and device structure of ITO/PEDOT:PSS/P3HT:PCBM/Al.

The TMF as discussed in chapter 3 is used to predict J_{SC} for the active layer thickness in a range from 50 nm to 250 nm for 1:0.8 P3HT:PCBM active layer. The optical constants (n, k) of the active layer were derived from the literature [5.44]. The results are plotted in Fig. 5.12. As predicted, obvious oscillatory behavior is observed because of the very thin active layer compared with the light wavelength. When the P3HT:PCBM ratio is 1:0.8, the first and second optical interference peaks are found at the P3HT:PCBM layer thicknesses of around 85 nm and 230 nm. Both the two optical interference peaks should be used to optimize the active layer thickness.

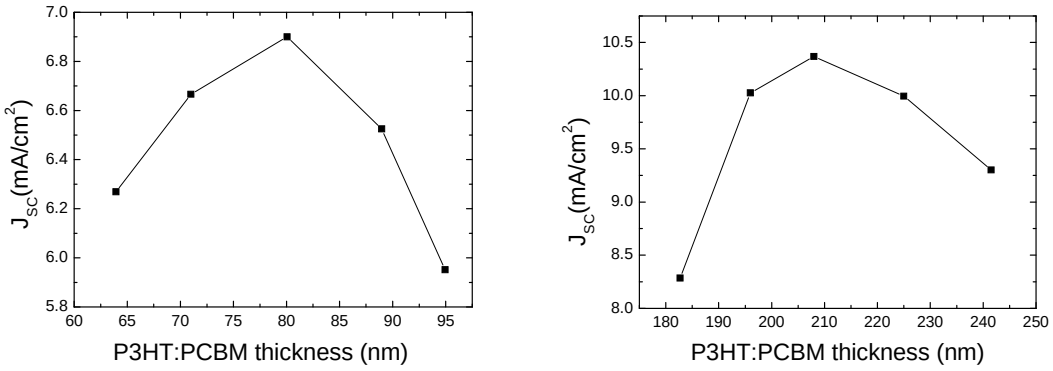

(a) (b)

Fig. 5.13 Optimization of active layer thickness. (a) around the first optical interference peak, and (b) around the second optical interference peak. All devices were post-annealed at 160^{o}C for 10 mins.

According to the simulated results, the devices were fabricated around the first and the second optical interference peaks. The experimental results for the different active layer thicknesses are shown Fig. 5.13. As predicted, J_{SC} shows a periodic behavior with the variation of the active layer thickness. The J_{SC} increases from as low as 6.25 mA/cm^2 (for the device with active layer thickness, t=64 nm) to as high as 6.93 mA/cm^2 (for t=80

nm), and then decreases around the first interference peak. The same trend is observed around the second optical interference peak at a thickness of 208 nm. J_{SC} reaches a value as high as 10.37 mA/cm^2 at the second optical interference peak. The higher J_{SC} comes from the better absorption ability. It is obviously shown that the second peak can absorb more light than the first peak as shown in Fig. 5.14. Thus the second optical interference peak is more preferred to achieve a higher PCE. Then around this peak, the annealing conditions are investigated.

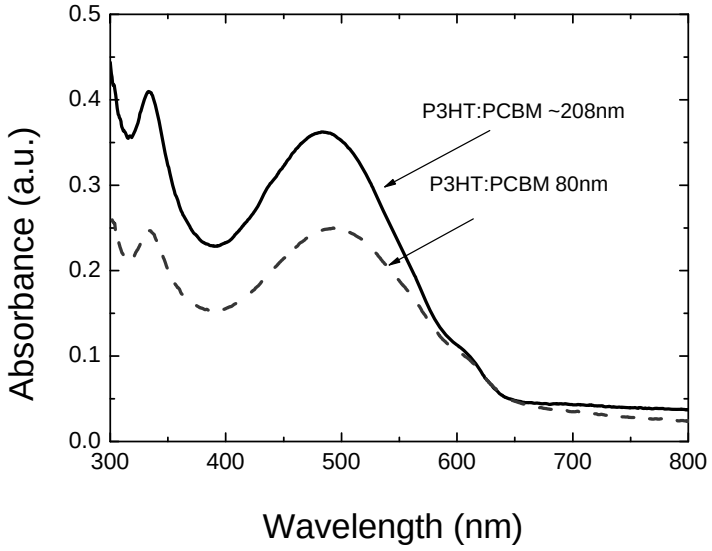

Fig. 5.14 UV-visible absorption spectra of P3HT:PCBM (about 80 nm thick) and P3HT:PCBM (about 208 nm thick).

Optimization of annealing conditions

The device performance depends greatly on annealing temperatures as clearly seen from Fig. 5.15. The reasons for the performance to be improved by the annealing process have been widely investigated. It is clear that for an efficient organic bulk HJ solar cell,

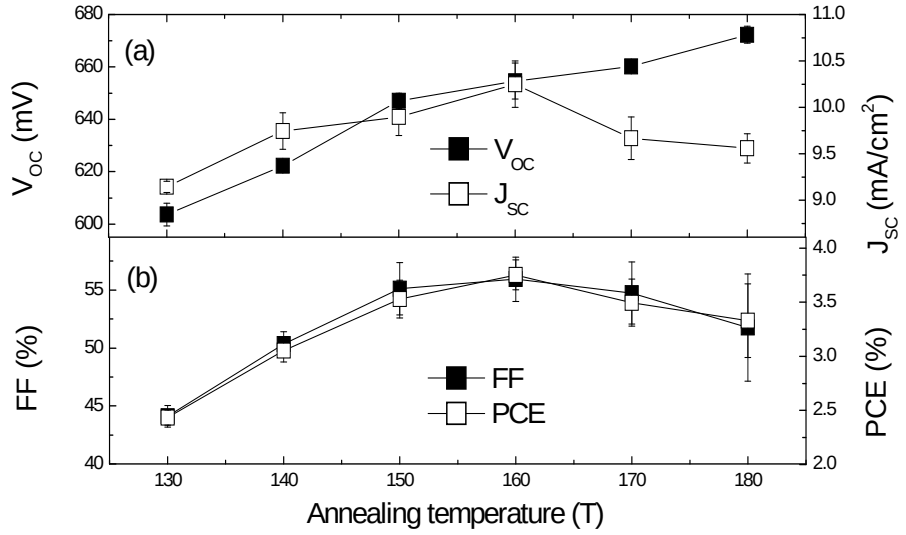

Fig. 5.15 Optimization of Glass/ITO/PEDOT:PSS/P3HT: PCBM/Al devices. (a) and (b): Relations of device performance and annealing conditions. The P3HT:PCBM layer thickness keeps constant of 208 nm.

D and A domains must be small enough so that most of the excitons can diffuse into the D/A interfaces before they decay. At the same time, the interpenetrating transport network must be formed for the efficient charge transport. Thus, the morphology optimization is of great important. By varying the annealing condition, the morphology can be well controlled. *Padinger et al* [5.9] reported that J_{SC} and FF were obviously enhanced by annealing the device with an applied voltage. A latter study by *Li* et al. [5.45] also reported that the device performance was improved by a slowing dry process.

These results were related to the better morphology as discussed in previous and also related to the increase of the charge carrier mobility. The same reason should also be responsible for our results. The highest PCE in our experiments is achieved when the annealing temperature is 160^{o}C which is very close to the annealing temperatures

reported by *Ma et al.* [5.2] and *Reyes et al* [5.5]. The analysis of changes in film morphology has shown that the changes in film crystallinity and aggregation within the film PCBM nanophase lead to the improved PV characteristics at this temperature [5.28]. When the annealing temperature is increased, a steady enhancement of V_{OC} is observed because the e-beam evaporated Al can induce dipoles at the interface between active layer and cathode as discussed above.

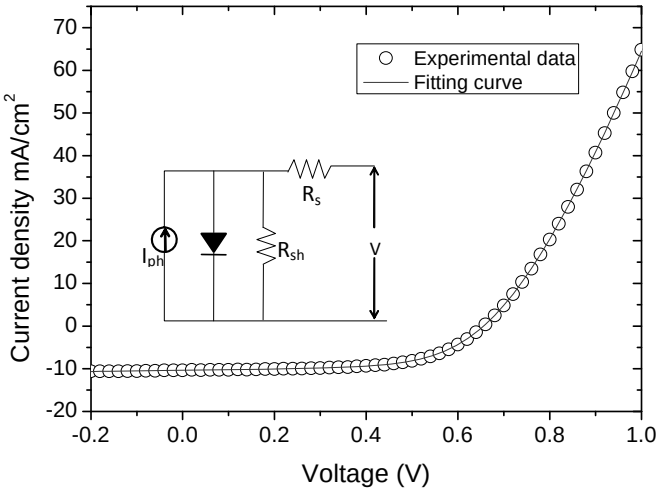

Fig. 5.16 Characteristics of the device around the second optical interference peak. Inset: the equivalent circuit of the solar cell is also shown.

Having been annealed at 160^{o}C for 10 min, the device shows the optimized performance. Use the macroscopic equation

$$I = I_S\left(e^{\frac{q(V+R_SI)}{nk_BT}} - 1\right) + \frac{V - R_SI}{R_{Sh}} - I_{ph} \tag{5.3}$$

The curve is fitted (Fig. 5.16) and the macroscopic parameters are extracted and listed in Table 5.3.

Table 5.3 Parameters extracted from the I-V curves (Fig. 5.16)

parameters	$I_{ph}(mA/cm^2)$	$I_S(mA/cm^2)$	$R_s(\Omega cm^2)$	$R_{sh}(\Omega cm^2)$	n
value	10.409	0.00094	3.1	679.7	2.75

5.3.4 Conclusion

The effects of the optical interference and the annealing on device performance were presented. Due to the optical interference effect, J_{SC} showed a periodic behaviour with the variation of thickness. With the help of the simulated results, the first two optical interference peaks were found to be corresponding to thicknesses of 80 nm and 208 nm. At the same time, the effect of annealing on the performance was also studied. Based on post-annealing, different annealing temperatures were tested. The optimized annealing condition was found to be 160^oC for 10 min in a nitrogen atmosphere.

5.4 Summary

The experimental studies were carried out to investigate P3HT:PCBM based HJ PV cells in this chapter. It was found that the strengthened contact due to the bonding reinforcements (Al-O-C bonds and P3HT-Al complex) at the blend/metal interface for post-annealed device improves the charge collection at the cathode side. Carrier separation can be facilitated via the improved nanoscaled morphology of the post-annealed polymer blend. The Al capping layer promotes efficient formation of the P3HT crystallites and thus enhances the light harvesting property of the polymer blend.

Evidence for the latter has been derived from the improved shape of the absorption spectrum. The results underline the importance of applying the most efficient annealing sequence in order to achieve the best PV device performance.

By using the e-beam deposited Al cathode, a significant increase of V_{OC} was obtained in the polymer-fullerene bulk HJ solar cell. Electrical characterizations suggested that the energetic particles in the e-beam deposition induce deep interface hole traps in the P3HT/Al interface while leaving the fullerene unaffected. The deep trapped holes near the P3HT/Al interface could induce the image negative charges in the cathode and thus form "dipoles". These "dipoles" lead to the lowering of the Al effective work function and cause the enhancement of V_{OC}.

Based on above findings, P3HT:PCBM bulk OSCs were optimized. As predicted by the TMF method, an obvious oscillatory behavior of J_{SC} was observed in the experiments. The devices were optimized around the first two optical interference peaks. It was found that the optimized thicknesses are 80 nm and 208 nm. Based on the post-annealing, different annealing temperatures have been tested. The optimized annealing condition was found to be 160^{o}C for 10 min in a nitrogen atmosphere.

References

[5.1] L. H. Nguyen, H. Hoppe, T. Erb, S. Günes, G. Gobsch and N. S. Sariciftci, Adv. Funct. Mater., 17, 1071 (2007).

[5.2] W. Ma, C. Yang, X. Gong, K. Lee and A. J. Heeger, Adv. Funct. Mater., 15, 1617 (2005).

[5.3] T. Erb, U. Zhokhavets, G. Gobsch, S. Raleva, B. Stühn, P. Schilinsky, C. Waldauf and C. J. Brabec, Adv. Funct. Mater., 15, 1193 (2005).

[5.4] X. Yang, J. Loos, S. C. Veenstra, W. J. H. Verhees, M. M. Wienk, J. M. Kroon, M. A. J. Michels and R. A. J. Janssen, Nano. Lett., 5, 579 (2005).

[5.5] M. R. Reyes, K. Kim, J. Dewald, R. L. Sandoval, A. Avadhanula, S. Curran and D. L. Carroll, Org. Lett., 7, 5749 (2005).

[5.6] K. Kim, J. Liu, M. A. G. Namboothiry and D. L. Carroll, Appl. Phys. Letts., 90, 163511 (2007).

[5.7] V. D. Mihailetchi, H. Xie, B. D. Boer, L. M. Popescu, J. C. Hummelen, P. W. M. Blom and L. J. A. Koster, Appl. Phys. Letts., 89, 012107 (2006).

[5.8] M. R. Reyes, K. Kim and D. L. Carroll, Appl. Phys. Letts., 87, 083506 (2005).

[5.9] F. Padinger, R. S. Rittberger and N. S. Sariciftci, Adv. Funct. Mater., 13, 85 (2003).

[5.10] Y. Zhao, Z. Xie, Y. Qu, Y. Geng and L. Wang, Appl. Phys. Letts., 90, 043504 (2007).

[5.11] Y. Kim, S. A. Choulis, J. Nelson, D. D. C. Bradley, S. Cook and J. R. Durrant, Appl. Phys. Lett., 86, 063502 (2005).

[5.12] D. Chirvase, J. Parisi, J. C. Hummelen and V. Dyakonov, Nanotechnology, 15, 1317 (2004).

[5.13] M. Drees, H. Hoppe, C. Winder, H. Neugebauer, N. S. Sariciftci, W. Schwinger, F. Schäffler, C. Topf, M. C. Scharber, Z. Zhu and R. Gaudiana, J. Mater. Chem., 15, 5158 (2005).

[5.14] Y. Kim, S. A. Choulis, J. Nelson, D. D. C. Bradley, S. Cook and J. R. Durrant, J. Mat. Sci., 40, 1371 (2005).

[5.15] N. Camaioni, G. Ridolfi, G. C. Miceli, G. Possamai and M. Maggini, Adv. Mater., 14, 1735 (2002).

[5.16] Y. Park, J. Lee, S. K. Lee and D. Y. Kim, Appl. Phys. Lett., 79, 105 (2001).

[5.17] Q. D. Ling, S. Li, E. T. Kang, K. G. Neoh, B. Liu and W. Huang, Appl. Surf. Sci., 199, 74 (2002).

[5.18] S. Kwon, S. C. Kim, Y. Kim, J.-G. Lee, S. Kim and K. Jeong, Appl. Phys. Lett., 79, 4595 (2001).

[5.19] R. Lazzaroni, J. L. Brédas, P. Dannetun, M. Lögdlund, K. Uvdal and W. R. Salaneck, Synth. Met., 41-43, 3323 (1991).

[5.20] A. Lachkar, A. Selmani, E. Sacher, M. Leclerc and R. Mokhliss, Synth. Met., 66, 209 (1994).

[5.21] A. Lachkar, A. Selmani and E. Sacher, Synth. Met., 72, 73 (1995).

[5.22] P. Dannetun, M. Boman, S. Stafström, W. R. Salaneck, R. Lazzaroni, C. Fredriksson, J. L. Brédas, R. Zamboni and C. Taliani, J. Chem. Phys., 99, 664 (1993).

[5.23] W. J. H. van Gennip, J. K. J. van Duren, P. C. Thüne, R. A. J. Janssen and J. W. Niemantsverdriet, J. Chem. Phys., 117, 5031 (2002).

[5.24] Q. J. Cai, Q. D. Ling, S. Li, F. R. Zhu, W. Huang, E. T. Kang and K. G. Neoh, Appl. Surf. Sci., 222, 399 (2004).

[5.25] H. Y. Seung and J. E. Whitten, Synth. Met., 114, 305 (2000).

[5.26] M. Boman, S. Stafström and J. L. Brédas, J. Chem. Phys., 97, 9144 (1992).

[5.27] X. Yang, A. Alexeev, M. A. J. Michels and J. Loos, Macromolecules, 38, 4289 (2005).

[5.28] M. T. Rispens, A. Meetsma, R. Rittberger, C. J. Brabec, N. S. Sariciftci and J. C. Hummelen, Chem. Commun., 2116 (2003).

[5.29] F. Zhang, K. G. Jespersen, C. Björström, M. Svensson, M. R. Andersson, V. Sundström, K. Magnusson, E. Moons, A. Yartsev and O. Inganäs, Adv. Funct. Mater., 16, 667 (2006).

[5.30] H. Hoppe, M. Niggemann, C. Winder, J. Kraut, R. Hiesgen, A. Hinsch, D. Meissner and N. S. Sariciftci, Adv. Funct. Mater., 14, 1005 (2004).

[5.31] P. Peumans, S. Uchida and S. R. Forrest, Nature, 425, 158 (2003).

[5.32] H. Kim, W. W. So and S. J. Moon, Sol. Energy Mater. Sol. Cells, 91, 581 (2007).

[5.33] W. Wang, H. Wu, C. Yang, C. Luo, Y. Zhang, J. Chen and Y. Cao, Appl. Phys. Lett., 90, 183512 (2007).

[5.34] B. D. Cullity, in Elements of X-Ray Diffraction, Addison-Wesley, Reading, MA, (1956).

[5.35] H. P. Klug and L. E., Alexander X-ray diffraction procedures for polycrystalline and amorphous materials, 2nd ed. New York: Wiley; (1974).

[5.36] A. Swinnen, I. Haeldermans, M. V. Ven, J. D. Haen, G. Vanhoyland, S. Aresu, M. D. Olieslaeger and J. Manca, , Adv. Funct. Mater., 16, 760 (2006).

[5.37] B.P. Rand, D.P. Burk and S.R. Forrest, Phys. Rev. B, 75, 115327 (2007).

[5.38] M. C. Scharber, D. Wuhlbacher, M. Koppe, P. Denk, C. Waldauf, A.J. Heeger, and C.J. Brabec, Adv. Mater. (Weinheim, Ger.), 18, 789 (2006).

[5.39] C. J. Brabec, S. E. Shaheen, C. Winder and N. S. Saricifci, Appl. Phys. Lett., 80, 1288 (2002).

[5.40] E. Ahlswede, J. Hanisch and M. Powalla, Appl. Phys. Lett., 90, 163504 (2007).

[5.41] L. H. Nguyen, H. Hoppe, T. Erb, S. Gunes, G. Gobsch and N. S. Sariciftci, Adv. Funct. Mater., 17, 1071 (2007).

[5.42] P. H. Nguyen, S. Scheinert, S. Berleb, W. Bruttin and G. Paasch, Organic Electronics, 2, 105 (2001).

[5.43] E. Ahlswede, J. Hanisch and M. Powalla, Appl. Phys. Lett., 90, 063513 (2007).

[5.44] G. Dennler, K. Forberich, M.C. Scharber, C. J. Brabec, I. Tomis, K. Hingerl and T. Fromberz, J. Appl. Phys., 102, 054516 (2007).

[5.45] G. Li, V. Shrotriya, J. Huang, Y. Yao, T. Moriarty, K. Emery and Y. Yang, Nature Materials, 4, 864 (2005).

Chapter 6
Tandem structure design for the performance enhancement of OSCs

In the previous chapters, great efforts have been devoted into the P3HT:PCBM bulk HJ OSCs both in the mechanism and experimental research. A clear picture of the device working mechanism has been built. By the experimental research, the performance of P3HT:PCBM based OSCs has been improved. However, compared to the inorganic counterparts, PCE of OSCs is still very low [6.1-6.4]. Several factors limit PCE of organic PV cells. One such important factor is the limited overlap between the organic absorber and the solar spectrum [6.5-6.8]. The widely used organic materials can only absorb a limited spectrum range. The P3HT:PCBM absorber system has its main absorption below 650nm. However, as we know, there is approximately more than 60% of the total solar energy at the wavelengths $\lambda > 600$nm [6.6]. Obviously, to enhance solar absorption ability of the organic PV cells is a very effective way to improve the device performance. Beyond modifying the properties of the materials to match the solar spectrum, other methods are also used to enhance spectral coverage [6.6-6.9]. Among them, the tandem structure is a very effective method to overcome this problem. As discussed in Chapter 2, the conventional tandem cells are stacked on the top of each other and connected in series or in parallel. By combining different organic materials with complementary absorption spectra in tandem cell [6.6-6.8], it can improve the spectral coverage and increase the photon harvesting. However, achieving an effective tandem cell still presents its own difficulties. Usually, between the front cell and the back cell,

there is a thermal evaporated metal layer as the intermediate layer. This layer can reflect light and decrease the transmitted light easily. Moreover, in a series tandem solar cell, J_{SC} generated by each subcell must be equal to prevent buildup of photogenerated charges which lead to a lower efficiency [6.2]. Thus it needs careful control of the respective layer thickness. In addition, for tandem polymer solar cells, spin coating multiple layers can result in significant damage to the bottom layer from the solvent used for spin coating of the subsequent layers [6.10]. In order to overcome these technology difficulties, in this chapter we demonstrate a new tandem structure to improve the spectral coverage. In this new tandem cell, no semitransparent intermediate layer is required in comparison with the conventional tandem solar cells. This decreases the complexity of device fabrication and reduces the light loss. The new tandem solar cell shows promising performance.

6.1 Structure design

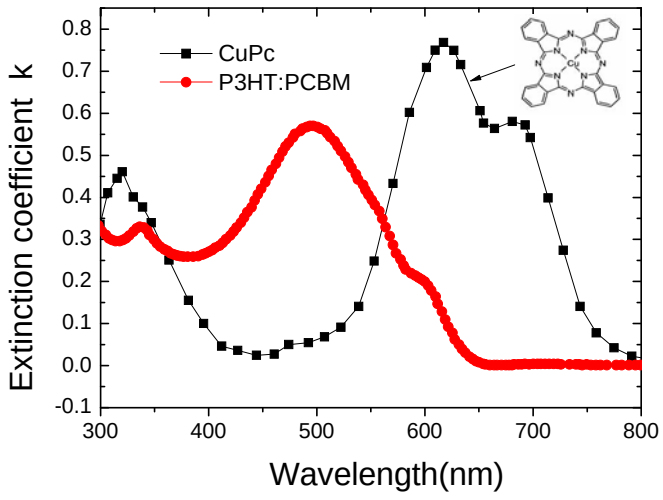

Fig. 6.1 Extinction coefficient of CuPc and P3HT:PCBM blend materials

CuPc and P3HT:PCBM materials can absorb complementary absorption spectra as shown in Fig. 6.1. By combining these materials together, it is expected to improve the light harvesting ability. Thus these two material systems are fit for the tandem structure. But because of the difficulties discussed above, to fabricate the tandem solar cell using the traditional structure is not easy. It is well known that CuPc and PCBM can be used for the bilayer structure. Based on this point, here we propose a simple tandem structure. In this structure, a CuPc layer is inserted between the P3HT:PCBM blend layer and the PEDOT:PSS layer. The proposed structure and the corresponding energy level diagram of the device are shown in Fig. 6.2.

The work principles of this structure can be well understood by comparing with the standalone solar cells. As shown in Fig. 6.3, in a standalone CuPc:PCBM bilayer solar cell, excitons can be easily dissociated at the interface of CuPc/PCBM and collected by the electrodes because of the energy offset between CuPc and PCBM (0.2 eV in LUMO offset and 1 eV in HOMO offset). The same thing also happens in the proposed structure. Thus, essentially CuPc and PCBM form a bilayer HJ PV subcell. In the same way, the blend P3HT and PCBM also form a bulk HJ PV subcell. In this subcell, excitons are dissociated throughout the interface of the blend layer. The free electrons pass the blend layer and are collected by the cathode as in the standalone solar cell. However, there is a small difference for the hole transport process compared with the standard standalone P3HT:PCBM bulk solar cell. As shown in Fig. 6.2 (a), the holes must pass through the extra CuPc layer. From the energy level diagram (Fig. 6.2 (a)), almost the same HOMO energies of CuPc and P3HT make it easy for the holes to pass through CuPc layer and collected by the anode.

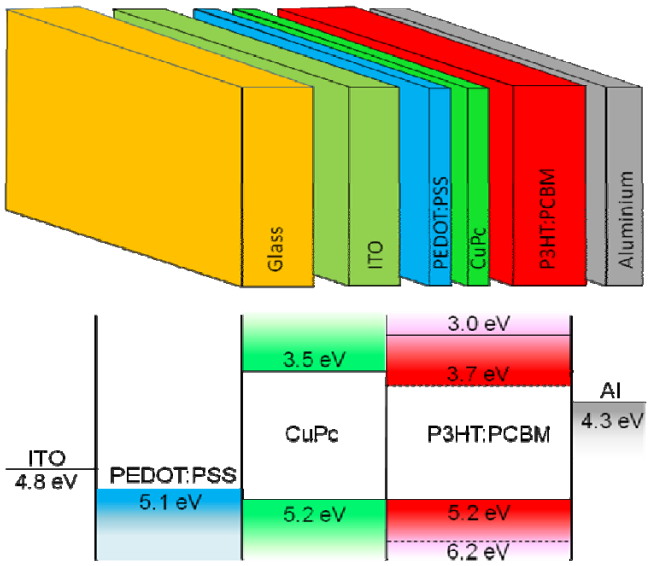

(a)

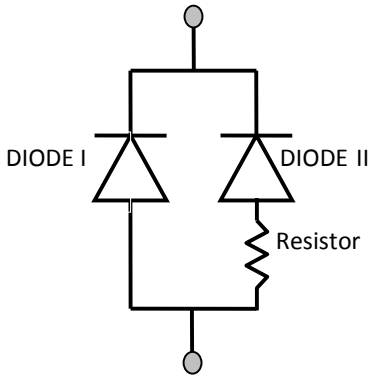

(b)

Fig. 6.2 Proposed tandem structure (a) layout structure and energy diagram of the proposed tandem PV cell. PCBM is simultaneously used to form CuPc/PCBM bilayer HJ subcell and P3HT:PCBM blend bulk HJ subcell; and (b) a simple equivalent circuit model of the PV cell. The extra resistor indicates the fact that holes generated in the blend layer have to pass the CuPc layer. All the material parameters are extracted from the literatures [5.11, 5.12].

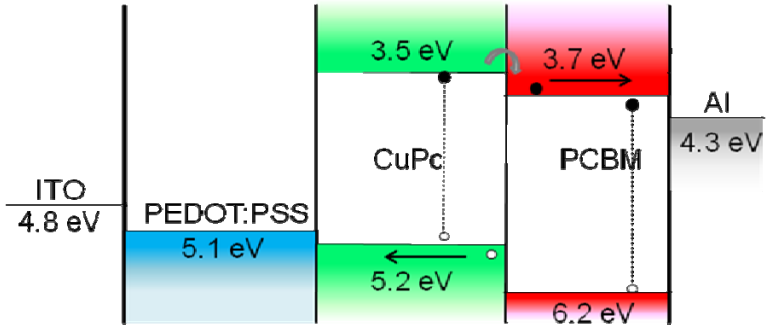

(a)

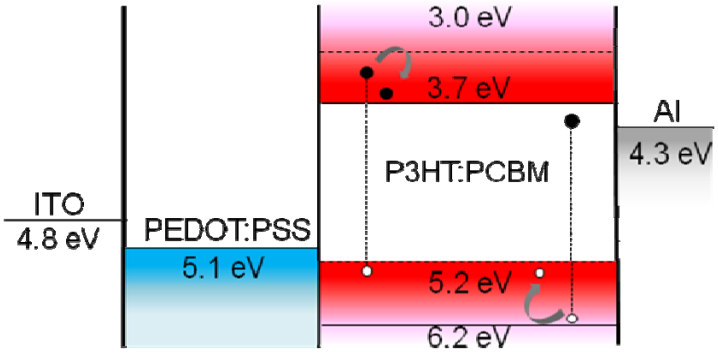

(b)

Fig. 6.3 (a) Energy diagram of standalone CuPc/PCBM bilayer HJ cell, and (b) Energy diagram of standalone P3HT:PCBM blend bulk HJ cell

As discussed above, PCBM is simultaneously used to form the bilayer HJ PV subcell (CuPc/PCBM) and the bulk HJ PV subcell (P3HT:PCBM). This structure can be regarded as a parallel connection of two individual subcells, as described in the simple circuit model of Fig. 6.2 (b). The extra resistor indicates the fact that holes generated in the blend layer have to pass the extra CuPc layer. This structure is different from the conventional tandem PV cells. In the latter, the design and control of the intercellular layer are of critical importance to ensure that the recombination is effective and sufficient

light can reach the back cell. For our proposed tandem structure, an intercellular connection layer is not required. Thus, photon loss due to reflection and absorption of the intercellular layer and the complexity of the devices are significantly reduced.

6.2 Device modeling

Theoretical analysis by optical modeling is a powerful way to understand and predict the performance of OSCs. In order to evaluate the validity of the structure, the optical aspects are investigated in this section. The extinction coefficients of CuPc and P3HT:PCBM have been shown in Fig. 6.1 and will be used in the TMF method [5.11, 5.12] as described in chapter 3.

Fig. 6.4 shows the calculated total excitons generated in the multilayers. Obvious oscillatory phenomenon of the exciton number in the active layer is observed with the thickness variation of the P3HT:PCBM layer and the CuPc layer. This is because of the intense optical interference effect induced by the very thin layer compared with the incident light, which has been discussed in chapter 3. Line I refers to the exciton number variation with the P3HT:PCBM layer thickness when there is no CuPc layer. Maxima are found at the P3HT:PCBM layer thickness of 85 and 230 nm. Line II and line III show the total exciton number variation with the CuPc layer while keeping the P3HT:PCBM layer thickness fixed at 85 and 230 nm, respectively. Obviously, with a thin CuPc layer underneath, the exciton number is increased effectively. The increased excitons can contribute to the photocurrent because of the easy exciton dissociation at the CuPc/PCBM interface. As shown in Fig. 6.4, the optical interference peaks are obviously

observed along Line II and III for this multilayer. These two regions are preferred for the proposed structure.

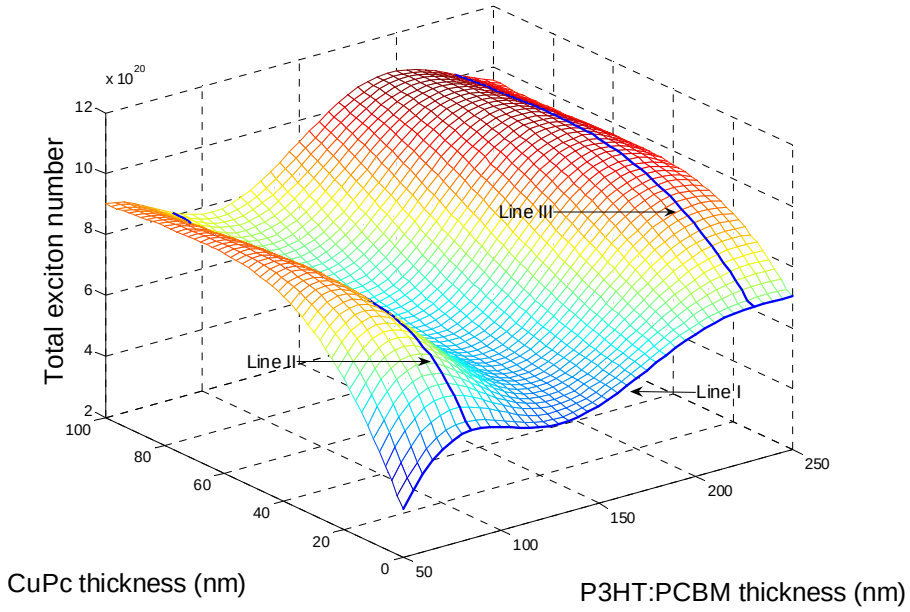

Fig. 6.4 Variation of total exciton number with the layer thickness in the proposed structure. Line I: the exciton number variation with the P3HT:PCBM layer thickness when there is no CuPc layer. Line II and III: the exciton number variation with the CuPc layer thickness when the P3HT:PCBM layer is kept at 85 nm and 230 nm, respectively.

6.3 Experimental

All the devices in this work were fabricated using ITO-coated glass substrates. After routine solvent cleaning (treated sequentially with detergent, de-ionized water, acetone, and isopropanol in an ultrasonic bath for about 15 minutes), the dried ITO glass substrates were treated with oxygen plasma for about three mins. Then the filtered PEDOT:PSS suspension (through 0.45 μm filter) was spin coated on the top of the ITO

surface to form a ~50 nm layer, under ambient conditions, before drying the substrates at 90^{o}C in an oven for more than 3 hours. And then the CuPc layer was deposited by thermal evaporation under a pressure of about 5.4x10^{-5} Pa. P3HT:PCBM was dissolved in dichlorobenzene at a weight ratio of 1:0.8 and stirred for more than 72 hours in the glove box before spin casting to form the blend layer. The blend layer thickness was controlled by changing the spin speed and solution concentration. Finally an Al electrode of about 100 nm in thickness was deposited by e-beam evaporation at a pressure of 2.4x10^{-4} Pa through a shadow mask. No buffer layer between the organic layer and cathode was used. For comparison, the standalone P3HT:PCBM blend and CuPc/PCBM bilayer OSCs were also fabricated. The current-voltage (I-V) characteristics were measured using a Keithley 2400 parameter analyzer under a simulated light intensity of 100 mW/cm^2 (AM 1.5G) calibrated by an optical power meter.

Absorption spectra of organic films on glass were measured using a Shimadzu UV-3101 PC UV-VIS-NIR spectrophotometer. AFM measurement was taken with a Nanoscope III A (Digital Instruments) scanning probe microscope.

6.4 Experimental results and discussion

The simulation has confirmed the validity of this proposed structure. Based on these results, the proposed solar cells (CuPc/P3HT:PCBM) as well as the standalone bilayer HJ (CuPc/PCBM) and bulk HJ (P3HT:PCBM) PV cells have been fabricated in the same batch. In the following sections, we will focus on the electrical characteristics of the devices.

6.4.1 First optical interference peak

The first optical interference peak was firstly used to fabricate the proposed tandem device as shown in Fig. 6.2. A CuPc layer was deposited before spin coating the P3HT:PCBM film. To evaluate the absorption ability of the multilayer, the absorption spectra were measured and shown in Fig. 6.5.

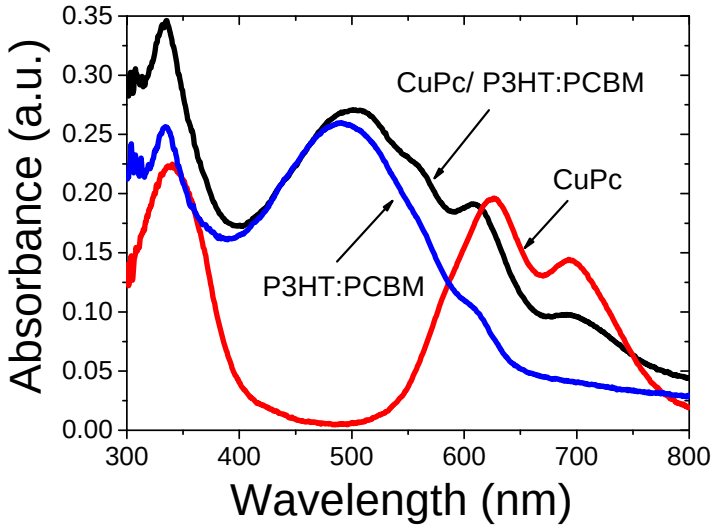

Fig. 6.5 UV-VIS absorption spectra of P3HT:PCBM (80 nm), CuPc (20 nm) and CuPc (8 nm)/P3HT:PCBM (80 nm). The absorption bands of P3HT:PCBM and CuPc complement each other, and by combining these materials in the new tandem solar cell, the absorption spectrum can be spread over almost the entire visible spectrum.

As shown in Fig. 6.5, the absorption spectra of P3HT:PCBM and CuPc complement each other, making them appropriate for the use in a single device to expend the absorption spectra. The absorption peak of the P3HT:PCBM film is located at 490 nm, and the absorption range extends from the ultraviolet (UV) up to approximately 650 nm.

The CuPc film absorbs weakly in the wavelength range of 400~550 nm. However, it has two strong absorption bands: one in the wavelength range between 550~800 nm and the other below 400 nm. Combining these materials, the absorption spectrum of the proposed tandem PV cell covers almost the entire visible spectrum. This enhanced absorption spectrum is expected to lead to a larger number of photogenerated excitons, and thus a larger photocurrent.

The optimum condition for our device configuration was firstly investigated. When the thickness of P3HT:PCBM is 80 nm, the standard cell (ITO/PEDOT:PSS/ P3HT:PCBM/Al) shows the optimum PV response with J_{SC}=6.87 mA/cm^2, V_{OC}=0.63 V, FF=58% and η=2.50% [Fig. 6.6 and Table 6.1]. This efficiency is comparable to those reported in the literature with the same device structure [5.13-5.16]. Keeping the optimized P3HT:PCBM thickness as 80 nm constant, Fig 6.7 shows the variation of J_{SC} with the CuPc layer thickness in the proposed tandem PV cell. Obviously, with a thin CuPc layer underneath, J_{SC} increases effectively. However, a thick CuPc layer degrades the device performance, because a thicker CuPc layer increases the series resistance and hinders carrier transport. Moreover, according to the working principles of bilayer PV cells, only the excitons in the CuPc layer that can diffuse to the interface can contribute to the photocurrent. Thus, for a thick CuPc layer, some excitons are lost. The photoactive region is about 8 nm from the D/A interface [5.17], beyond this region the excitons cannot contribute to the current. If the CuPc layer is too thick, it also reduces the number of photons reaching the P3HT:PCBM blend layer due to their overlap in absorption spectra, and thus the P3HT:PCBM subcell is degraded. Considering these effects, the predicted J_{SC} is shown in Fig. 6.8. The thickness of the optimized CuPc layer is about 8

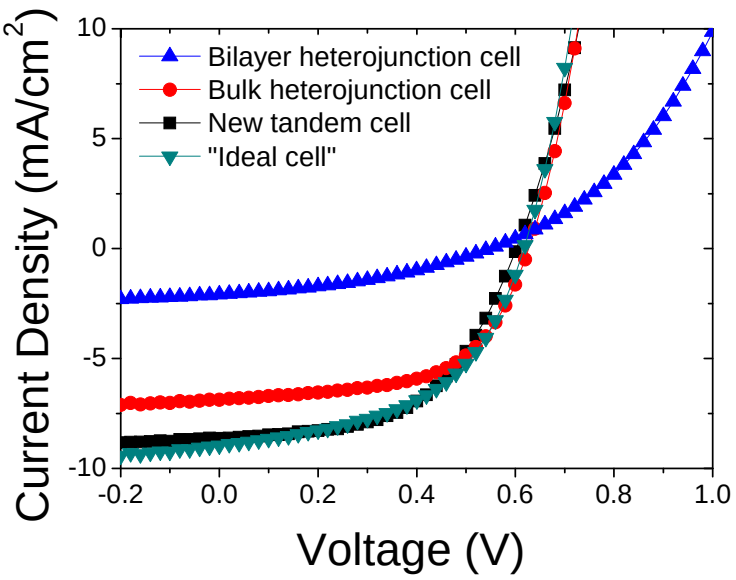

Fig. 6.6 I-V characteristics of three types of devices. Standalone bilayer HJ cell: ITO/PEDOT:PSS/CuPc/PCBM/Al; Standalone blend bulk HJ cell: ITO/PEDOT:PSS/P3HT:PCBM/Al; Proposed tandem PV cell: ITO/PEDOT:PSS/CuPc/P3HT:PCBM/Al; "Ideal cell": a theoretical cell with the sum of photocurrents of the standalone bilayer HJ cell and the blend bulk HJ cell. The illumination intensity is 100 mW/cm^2 (AM 1.5G).

Table 6.1 Electrical properties of standalone CuPc/PCBM and P3HT:PCBM PV cells, the proposed tandem PV cell, and the "ideal cell" (Fig. 6.6).

Cell type	Voc (V)	Jsc (mA/cm^2)	FF (%)	η (%)
Standalone bilayer HJ cell: ITO/PEDOT:PSS/CuPc/PCBM/Al	0.55	2.09	38	0.43
Standalone bulk HJ cell: ITO/PEDOT:PSS/P3HT:PCBM/Al	0.63	6.87	58	2.50
Proposed tandem PV cell: ITO/PEDOT:PSS/CuPc/P3HT:PCBM/Al	0.60	8.63	54	2.79
"Ideal parallel PV cell"	0.61	8.96	51	2.81

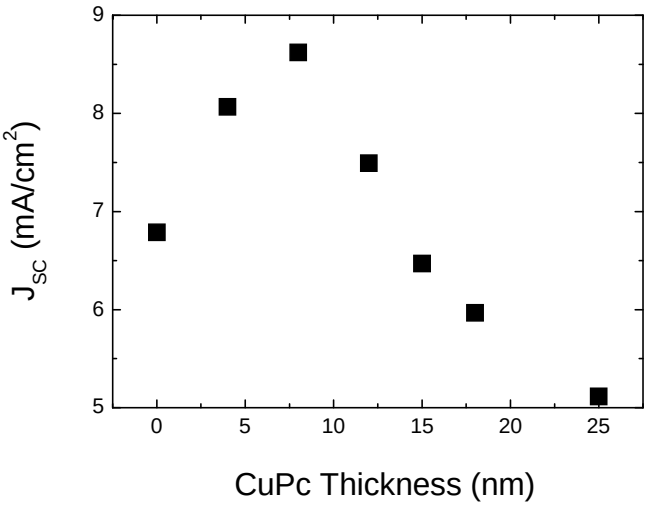

Fig. 6.7 Dependence of J_{SC} on the CuPc film thickness in the proposed tandem PV cell. The P3HT:PCBM layer is kept as constant of 80 nm. Device structure: ITO/PEDOT:PSS/CuPc/P3HT:PCBM/Al.

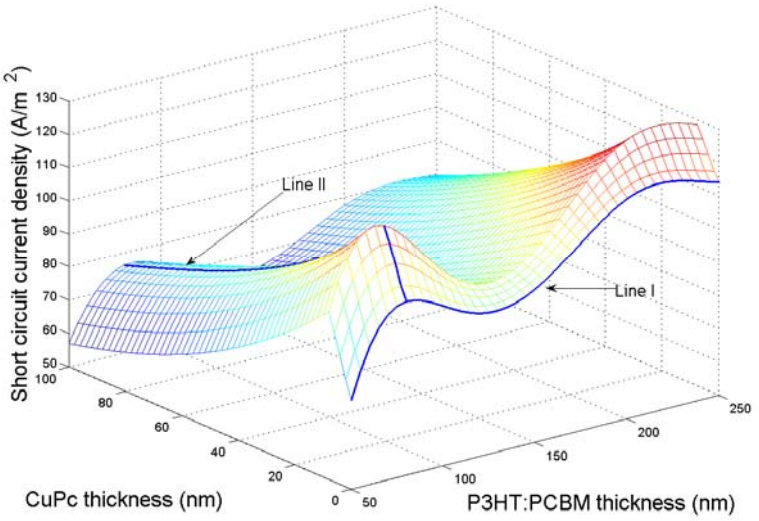

Fig. 6.8 The calculated J_{SC} with different layer thickness. Considering the photoactive region in CuPc is 8 nm. As can be seen from the graph, J_{SC} decreases when the CuPc layer is larger than 8 nm.

nm as shown in Fig. 6.7, which is just the photoactive region thickness. Using an 8 nm CuPc layer, the standalone CuPc/PCBM PV cell exhibits a PV response with J_{SC}=2.09 mA/cm^2, V_{OC}=0.55 V, FF=38% and η=0.43% [Fig. 6.6 and Table 6.1].

For the optimized layer thicknesses (CuPc～8nm and P3HT:PCBM～80nm), the tandem solar cell exhibits typical performance of J_{SC}=8.63 mA/cm^2, V_{OC}=0.60 V, FF=54% and η_e=2.79%, as shown in Fig. 6.6 and Table 6.1. To confirm the parallel connection of the subcells in the tandem cell, we simply add the photocurrents of the two standalone bilayer and bulk HJ cells together and denote it as an "ideal cell", whose I-V curve is also shown in Fig. 6.6. From the summarized electrical properties in Table 6.1, it is found that J_{SC} (8.63 mA/cm^2) and PCE (2.79%) of the fabricated tandem cell are just slightly lower than J_{SC} (8.96 mA/cm^2) and PCE (2.81%) of the "ideal cell". Thus, the PV performance is in accordance with that expected from the parallel connection in the proposed tandem cell and Kirchhoff's law. The slightly reduced J_{SC} and PCE can probably be attributed to overlap in absorption spectra between the CuPc layer and P3HT:PCBM layer. The statistical results of J_{SC} and PCE for the optimized tandem cell, as well as for the standalone cells, are shown in Fig. 6.9. Although the performance of the devices varies due to sample non-uniformity, it can be clearly seen that the proposed tandem cells have the respective J_{SC} and PCE values close to the sum of the standalone bulk and bilayer HJ cells.

Till now, the proposed tandem cell has been demonstrated around the first optical interference peak. The performance of the proposed tandem cell is equivalent to the combined performances of the two standalone single cells. Next we will show the devices around the second optical interference peak.

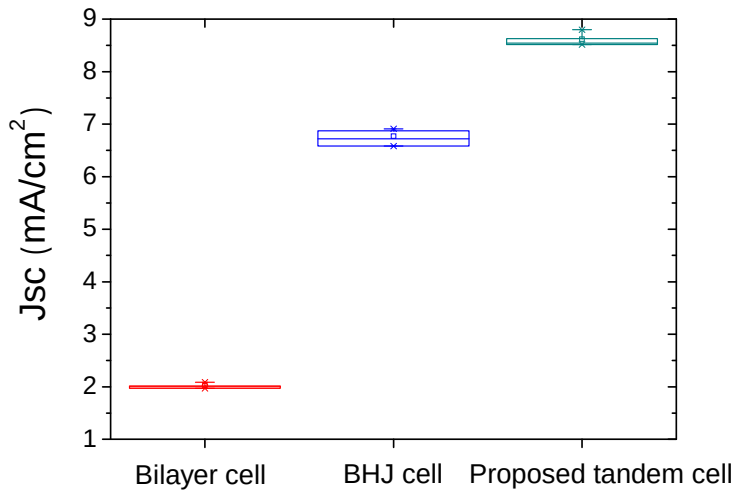

(a)

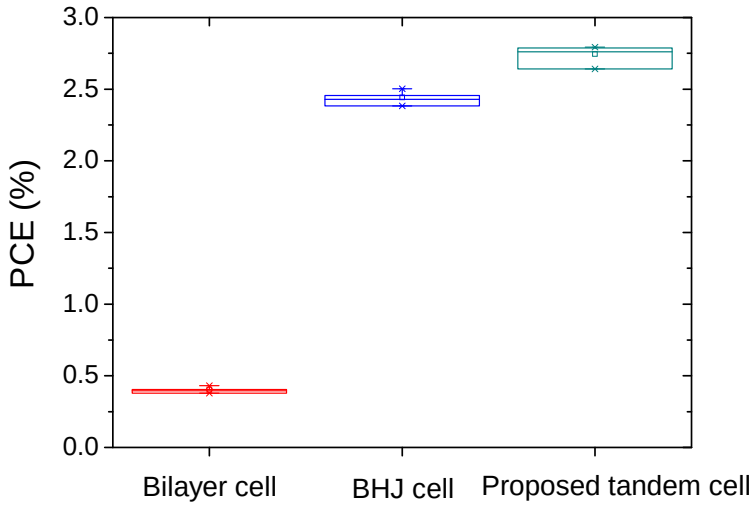

(b)

Fig. 6.9 Statistical properties of J_{SC} (a) and PCE (b). Bilayer cell: standalone CuPc/PCBM bilyar HJ PV cell; Bulk HJ cell: standalone P3HT:PCBM bulk HJ PV cell; Proposed tandem cell: CuPc/P3HT:PCBM PV tandem cell.

6.4.2 Second optical interference peak

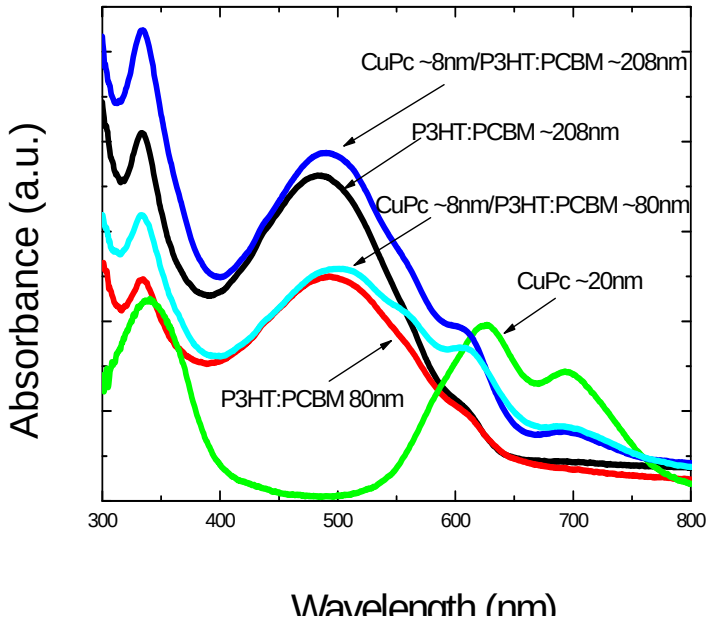

Fig. 6.10 UV-visible absorption spectra of P3HT:PCBM (~80 nm), P3HT:PCBM (~208 nm), CuPc (~20 nm), CuPc (~8 nm)/P3HT:PCBM (~80 nm) and CuPc (~8 nm)/P3HT:PCBM (~208 nm) structures. The absorption bands of P3HT:PCBM and CuPc complement each other, and by combining these materials in the proposed tandem PV cell, the absorption spectrum covers almost the entire visible range.

We have initially (chapter 5) optimized the standalone P3HT:PCBM OSCs (ITO/PEDOT:PSS/ P3HT:PCBM/Al) around the second optical interference peak. And the optimized P3HT:PCBM layer thickness is ~208 nm. Around this thickness, the film shows better absorption ability compared to the ~80 nm film (Fig. 6.10), which should increase J_{SC}.

A thin CuPc layer is then inserted between the PEDOT:PSS and blend layer, and its influence is studied by keeping the P3HT:PCBM blend layer of 208 nm thick and varying

the CuPc thickness (~4, ~8, and ~12 nm). From the absorption spectra shown in Fig. 6.10, the absorption spectrum of the multilayer structure extends covering almost the entire visible spectrum. Furthermore, the structure with CuPc(~8 nm)/P3HT:PCBM(~208 nm) absorbs more light in comparison with that with CuPc(~8 nm)/P3HT:PCBM(~80 nm) around the first optical interference peak. The inset of Fig. 6.11 shows that J_{SC} increases at the initial stage and then decreases with the CuPc thickness. The device shows a maximum J_{SC} of 12.54 mA/cm^2 when CuPc is of ~ 8 nm thick. This is inconsistent with the simulation result of the continuously increased total exciton number with CuPC thickness (Fig. 6.4). As around the first optical interference peak, this discrepancy results from the short exciton diffusion length of CuPc (Fig. 6.8).

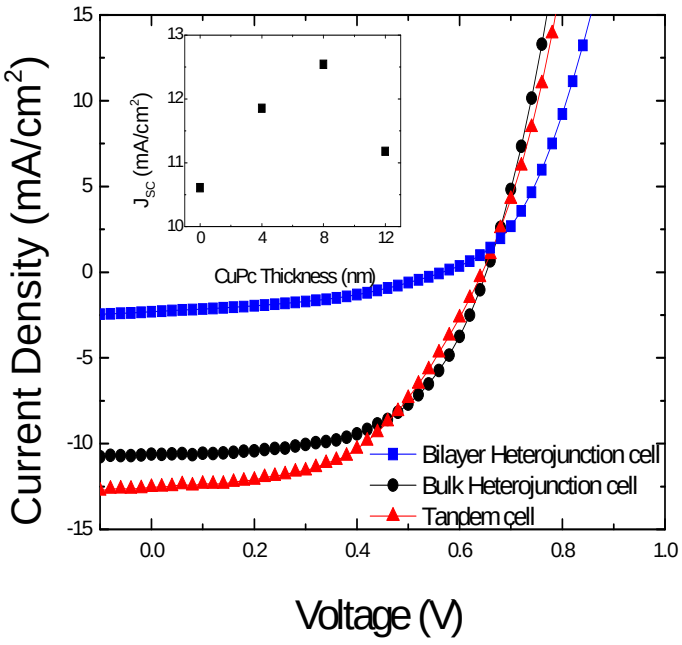

Fig. 6.11 I-V characteristics of three types of devices. Standalone bilayer HJ cell: ITO/PEDOT:PSS/CuPc/PCBM/Al; Standalone blend bulk HJ cell: ITO/PEDOT:PSS /P3HT:PCBM/Al; Tandem PV cell: ITO/PEDOT:PSS/CuPc/P3HT:PCBM/Al. Inset: dependence of J_{SC} on the CuPc film thickness in the proposed tandem PV cell. The P3HT:PCBM layer is kept constant at ~208 nm.

Fig. 6.11 shows the I-V characteristics of the optimized devices. The standalone P3HT:PCBM solar cell exhibits PCE of 3.95% with J_{SC}=10.61 mA/cm^2, V_{OC}=0.65 V, FF=57.1% and the standalone CuPc/PCBM solar cell exhibits PCE of 0.54% with J_{SC}=2.30 mA/cm^2, V_{OC}=0.58 V, FF=41.1%. For the optimized tandem solar cell, PCE of 4.13% with J_{SC}=12.54 mA/cm^2, V_{OC}=0.64 V, FF=51.1% is measured. The enhanced J_{SC}=12.54 mA/cm^2 of the tandem structure is nearly the sum of those of the standalone cells of CuPc/PCBM (J_{SC}=2.31 mA/cm^2) and P3HT:PCBM (J_{SC}=10.61 mA/cm^2), which confirms the parallel connection of the subcells in the tandem cell. Despite the enhanced J_{SC}, the series resistance (Rs), estimated to be about ~15.64 Ω cm^2 in the tandem cell, is larger than that of the standalone P3HT:PCBM solar cell (~10.94 Ω cm^2). Meanwhile, FF of the tandem solar cell also decreases to 51.1% from 57.1% of the standalone P3HT:PCBM solar cell. Both the changes of series resistance and FF imply that the additional interfaces (P3HT:PCBM/CuPc and CuPc/PEDOT:PSS) and CuPc in the tandem solar cell influence the charge transport and make the overall PCE only increased from 3.95% to 4.13%. It is expected that a further study of carrier transport in this structure can continuously improve the device performance.

6.5 Methods to further improve the proposed devices

Although the absorption spectra of CuPc and P3HT:PCBM can complement each other, the overall absorption spectra are only extended to 800 nm. Much light with the wavelength larger than 800 nm is missed. There is still an overlap between the absorption spectra of CuPc and P3HT:PCBM. All these factors limit the increase of PCE. Then the materials with better light harvesting ability and complemented absorption spectra are needed.

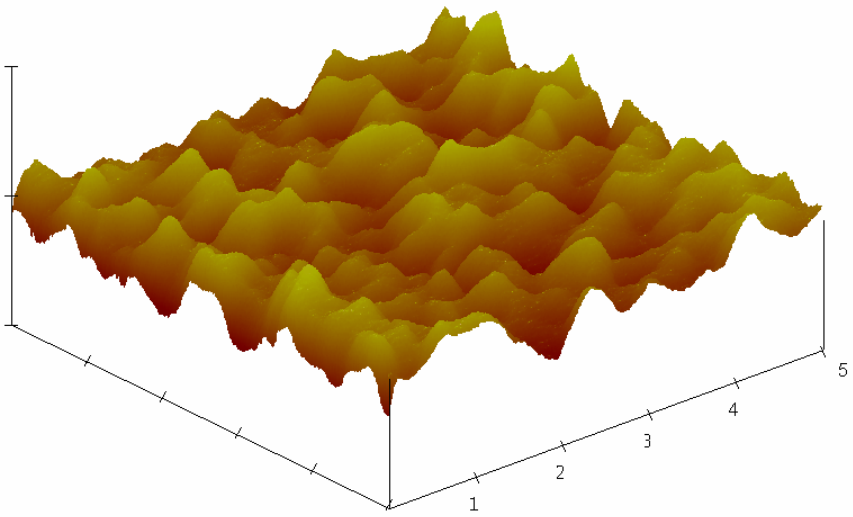

Fig. 6.12 AFM image of CuPc film grown on ITO/glass. The thickness of CuPc layer is 15 nm. Data scale is 10 nm. The root-mean-square roughness (σ_{rms}) of CuPc surface was measured to be only 1.26 nm.

Another way to improve the performance of the proposed tandem cell is to increase the CuPc and P3HT:PCBM interface areas. As discussed above, the thickness of the CuPc layer is limited by the photoactive region. As a result, only 8 nm CuPc layer is used. AFM shows that the root-mean-square roughness (σ_{rms}) of CuPc surface is low and only 1.26 nm. If σ_{rms} can be made large, the CuPc and P3HT:PCBM interface area will be greatly increased. This will greatly decrease the needed exciton diffusion length and then increase the CuPc photoactive region. If σ_{rms} is enhanced further, CuPc and PCBM may form another bulk HJ subcell as the P3HT:PCBM subcell. This will efficiently increase the exciton dissociation probability [5.17, 5.18]. It has been reported that the growth of CuPc layer can be controlled to form the needle-like crystals [5.18]. This growth method can help to increase the total CuPc and P3HT:PCBM interface areas. Thus it gives a great potential to improve the proposed tandem cell further.

6.6 Summary

PCE of OSCs is still low compared to their inorganic counterparts. One important limiting factor is the limited overlap of the absorption spectra of organic materials with the solar spectrum. Tandem structure is an effective approach to overcome this problem. In this chapter, we proposed and demonstrated a simple tandem structure of organic PV cell for efficient light harvesting. In this device structure, PCBM is employed simultaneously to form a bilayer HJ PV subcell with the underlying CuPc and a bulk HJ PV subcell with blended P3HT. In comparison with the conventional tandem structure, the omission of the semi-transparent intercellular connection layer reduces the complexity of the device and the light loss. This structure effectively improved J_{SC} and PCE. By using this structure, around the first optical interference peak, the optimized device showed J_{SC} of 8.63 mA/cm^2 and PCE of 2.79%. Around the second optical interference peak, the optimized solar cell showed J_{SC} of 12.54 mA/cm^2 and PCE of 4.13%.

References

[6.1] C.J. Brabec, N.S.Sariciftci, and J.C.Hummemen, Plastic Solar Cells, Adv. Funct. Mater. **11**, 15 (2001).

[6.2] P. Peumans, A. Yakimov, and S.R. Forrest, J. Appl. Phys., **93**, 3693 (2003).

[6.3] K. Kim, J. liu, M.A.G. Namboothiry, and D.L. Carroll, Appl. Phys. Lett. **90**, 163511 (2007).

[6.4] J. Y. Kim, K. Lee, N. E. Coates, D. Moses, T.Q. Nguyen, M. Dante, and A.J. Heeger, *Science,* **317**, 222 (2007).

[6.5] B. P. Rand, J.G. Xue, F. Yang, and S.R. Forrest, Appl. Phys. Lett. **87**, 233508 (2005).

[6.6] A. G. F. Janssen, T. Riedl, S. Hamwi, H.-H. Johannes, and W. Kowalsky, Appl. Phys. Lett. **91**, 073519 (2007).

[6.7] G. Dennler, H.J. Prall, R. Koeppe, M. Egginger, R. Autengruber, and N.S. Sariciftci, Appl. Phys. Lett. **89**, 073502 (2006).

[6.8] A. Hadipour, B. Boer,and P.W.M. Blom, J. Appl. Phys. **102**, 074506 (2007).

[6.9] M.Y. Chan, S.L. Lai, M.K. Fung, C.S. Lee, and S.T. Lee, Appl. Phys. Lett. **90**, 023504 (2007).

[6.10] V. Shrotriya, E.H. Wu, G. Li, Y. Yao, and Y. Yang, Appl. Phys. Lett. **88**, 064104 (2006).

[6.11] O. S. Heavens, Optical Properties of Thin solid Films (Dover, New York, 1965).

[6.12] L. A. A. Pettersson, L.S. Roman, and O. Inganas, J. Appl. Phys. **86**, 487 (1999).

[6.13] J. Y. Kim, S.H. Kim, H. Lee, K. Lee, W. Ma, X. Gong, and A. J. Heeger, Adv. Mater. **18**, 572 (2006).

[6.14] H.J. Kim, W.W. So, and S.J. Moon, Solar Energy Materials & Solar Cells, **91**, 581 (2007).

[6.15] A. Hayakawa, O. Yoshikawa, T. Fujieda, K. Uehara, and S. Yoshikawa, Appl. Phys. Lett. **90**, 163517 (2007).

[5.16] E. Ahlswede, J. Hanisch, and M. Powalla, Appl. Phys. Lett. **90**, 163504(2007).

[6.17] Peumans P, Yakimov A, Forrest SR. *J. Appl. Phys.,* **93,** 3693 (2003).

[6.18] P. Schilinsky, C. Waldauf, and C.J. Brabec, *Appl. Phys. Lett.* **81,** 3885 (2002).

[6.19] F. Yang, M. Shtein and S. R. Forrest, Natural Materials, **4**, 37(2005).

Chapter 7
Conclusion and outlook

7.1 Conclusions

The purpose of this work is to study the device mechanisms and design the novel structure of OSCs to improve the power conversion efficiency. Through this work, a clear theoretical picture of J_{SC} and V_{OC} was built, and the limited factors for them were also indicated. Experimental studies improved the P3HT:PCBM device performance. Specially, based on these understandings, a simple tandem structure was proposed, which efficiently improved the overall device performance. Generally, the main results and conclusions of this work are summarized as below.

The microscopic mechanism of J_{SC} in Bulk HJ solar cells was investigated. It was found that the optical interference effect becomes very important in OSCs. This is due to the very high absorption coefficients of organic materials compared to the inorganic materials which make the active layer very thin. Because excitons rather than free carriers are generated in organic materials, the exciton dissociation probability should be considered when predicting J_{SC}. Neglecting this factor, J_{SC} will be overestimated. At the same time, the influence of the carrier lifetime on J_{SC} also cannot be neglected. When the carrier lifetime is relatively short, J_{SC} only increases at the initial stage and then decreases rapidly with the increase of the active layer thickness. However, for a relatively long carrier lifetime, J_{SC} behaves wave-like with the increase of the active layer thickness. The validity of this model is confirmed by the experimental results.

Another important parameter, V_{OC}, was also investigated. Layered and bulk HJ PV cells showed different dependences on the electrodes. By the analysis, it was found that although V_{OC} of the two types of PV cells follows the same mechanism and is mainly determined by the light injected carriers at the electrodes and the D/A interface, their distinct structures lead to the different dependences of V_{OC} on the electrodes. The layered HJ OSCs have geometrically "flat" D/A and M/O interfaces, which make the effective thickness from the D/A interface to the M/O interface is very large. The large effective thickness leads to a thick barrier and a low electric field at M/O interface. Thus the barrier lowering is low and the number of carriers injected from the metal electrode by thermionic emission is relatively small. Under this condition, the light injected carriers at D/A interface tend to "pin" the Fermi level of the electrodes. As a result, V_{OC} shows only a very weak dependence on the work function of the electrodes. On the other hand, the formation of the interpenetrating network in bulk HJ OSCs decreases D and A domain dimensions greatly, which makes the effective thickness of D and A domains very small. When there is a high potential barrier at M/O interface, the electric field will be very high at M/O interface and even the carrier tunneling may occur. Then a large number of carriers will be injected from the metal electrodes into the organic materials. Thus, the light injected carriers at D/A interface cannot "pin" the metal Fermi level any more. A strong dependence of V_{OC} on the metal electrodes for bulk HJ PV cells is observed. This indicates that V_{OC} of bulk HJ OSCs can be increased by the interface engineering and guides us to increase V_{OC} of bulk HJ OSCs.

Based on the above understandings, the experimental studies were carried out to increase J_{SC} and enhance V_{OC} of the P3HT:PCBM solar cells. Experimentally, two main results were achieved:

(a) The post-annealing is preferred by the P3HT:PCBM bulk HJ OSCs. This is because of the improved contact at polymer/aluminum interface due to the formation of Al-O-C and P3HT-Al complex, the improved phase-structured morphology due to the prohibition of the overgrowth of PCBM and the enhanced P3HT crystallinity and thus a better light harvesting property of the polymer film.

(b) The e-beam deposited cathode should be used in the fabrication of P3HT:PCBM bulk HJ solar cells because it can efficiently improve V_{OC}. Electrical studies suggested that the energetic particles of Al could damage the P3HT/Al surface and induce deep hole traps while leaving fullerene unaffected. The trapped holes induce the image negative charges in the cathode and thus form "dipoles". These "dipoles" lower down the Al work function and should be responsible for the enhancement of V_{OC}.

Based on above findings, P3HT:PCBM bulk HJ OSCs with the e-beam evaporated Al cathode were post-annealed and used for the device optimization. The optimized thicknesses of the first two optical interference peaks were found to be 80 nm and 208 nm, respectively. Through the optimization, the device showed PCE around 4% at the second optical interference peak.

Although PCE is improved, the value is still low compared to inorganic counterparters. To increase the performance further, a simple tandem solar cell was proposed. In this device structure, PCBM is employed simultaneously to form a bilayer HJ PV subcell with the underlying CuPc and a bulk HJ PV subcell with blended P3HT. In

comparison with the conventional tandem structure, the omission of the semitransparent intercellular connection layer reduces the complexity of the device and the light loss. In the experiment, this structure effectively improved J_{SC} and PCE. Around the second optical interference peak, the optimized solar cell exhibited J_{SC} of 12.54 mA/cm^2 and PCE of 4.13%, which showed the potential of the proposed structure.

7.2 Recommendations for future work

The present study can help to improve the performance of OSCs. However, some issues should be further investigated.

For the standard P3HT:PCBM bulk HJ OSCs, the morphology needs to be further optimized. In this type of solar cells, P3HT and PCBM are blended randomly in the solution. The P3HT and PCBM domains and the interpenetrating network are formed by the self-phase separation. Usually, the "dead zones" (Chapter 2) are inevitable. Although thermal annealing process can improve the morphology and charge transport greatly, there is still a distance from the ideal morphology. The dynamics of the phase separation should be further investigated. This can help to better control the morphology. Other methods, such as electrical field, magnetic field and microwave separately or combining with the thermal annealing, may help further improve the morphology and should be investigated. The ordered structures, which can help form the ideal interpenetrating network, should be also studied and used in OSCs.

For the proposed tandem cell, the series resistance is increased and FF is decreased compared to the standard P3HT:PCBM OSCs. This is because that the additional interfaces (P3HT:PCBM/CuPc and CuPc/PEDOT:PSS) and CuPc itself in the tandem solar cell affect the charge transport. Then a further study of carrier transport is needed to

improve the device performance. Another way to improve the performance of the proposed tandem cell is to increase the CuPc and P3HT:PCBM interface area. Compared to the P3HT:PCBM bulk HJ subcell, the CuPc/PCBM bilayer subcell is less efficient. The very short exciton diffusion length in CuPc and the absorption spectra overlap between CuPc and P3HT:PCBM limit the thickness of CuPc of only 8 nm. By increasing CuPc and P3HT:PCBM interface area and at last forming the CuPc:PCBM bulk HJ subcell can efficiently increase the CuPc thickness and thus improve the performance of the proposed tandem solar cell.

List of Publications

Journal Articles:

1. **Chunfu Zhang**, S. W. Tong, Changyun Jiang, E. T. Kang, and D. S. H. Chan, Chunxiang Zhu, "Origin of different dependences of open circuit voltage on the electrodes in layered and bulk heterojunction organic photovoltaic cells", IEEE Transaction on Electron Device, 57, 397 (2010).
2. **Chunfu Zhang**, S. W. Tong, Chunxiang Zhu, Changyun Jiang, E. T. Kang, and D. S. H. Chan, "Enhancement of open circuit voltage induced by deep interface hole traps in polymer-fullerene bulk heterojunction solar cells", Applied Physics Letters, 94, 103305 (2009).
3. **Chunfu Zhang**, S. W. Tong, Changyun Jiang, E. T. Kang, D. S. H. Chan, and Chunxiang Zhu, "Efficient multilayer organic solar cells using the optical interference peak", Applied Physics Letters, 93, 043307 (2008).
4. **Chunfu Zhang**, S. W. Tong, Changyun Jiang, E. T. Kang, D. S. H. Chan, and Chunxiang Zhu, "Simple tandem organic photovoltaic cells for improved energy conversion efficiency", Applied Physics Letters, 92, 083310 (2008).
5. S. W. Tong, **Chunfu Zhang,** Changyun Jiang, E. T. Kang, D. S. H. Chan, and Chunxiang Zhu, "The use of thermal initiator to make organic bulk heterojunction solar cells with a good percolation path", Applied Physics Letters, 93, 043304 (2008).
6. S. W. Tong, **Chunfu Zhang,** Changyun Jiang, E. T. Kang, D. S. H. Chan, and Chunxiang Zhu, "Improvement in the hole collection of polymer solar cells by utilizing gold nanoparticle buffer layer", Chemical Physics Letters, 453, 73 (2008).
7. Hailong You, and **Chunfu Zhang**, "Effect of optical interference and annealing on the performance of solar cells based on Poly(3-hexythiophene):Fullerene", Chinese Physics B, 18, 2096 (2009).
8. Hailong You, and **Chunfu Zhang**, " Influence of optical interference and carrier lifetime on the short circuit current density of organic bulk heterojunction solar cells", Chinese Physics B, 18, 349 (2009).

Conference papers:

1. **Chunfu Zhang**, S. W. Tong, Chunxiang Zhu, Changyun Jiang, E. T. Kang, and D. S. H. Chan, "Influence of optical interference and carrier lifetime on the short circuit current density of organic bulk heterojunction solar cells", International Conference on Organic Electronics (ICOE), Eindhoven, The Netherlands, June 2007.
2. **Chunfu Zhang**, S. W. Tong, Chunxiang Zhu, Changyun Jiang, E. T. Kang, and D. S. H. Chan, "Performance enhancement of poly(N-vinylcarbazole) with covalently bonded C_{60} for photovoltaic application**"**, International Conference on Organic Electronics (ICOE), Eindhoven, The Netherlands, June 2007.
3. S. W. Tong, **Chunfu Zhang,** Changyun Jiang, E. T. Kang, D. S. H. Chan, and Chunxiang Zhu, "Application of gold nanoparticle buffer layer in organic solar cells", 4th International Meeting on Molecular Electronics (ElecMol08), Grenoble, France, 169 December 2008.